國立臺灣大學理學院物理學研究所

博士論文

Department of Physics

College of Science

National Taiwan University

Doctoral Dissertation

激發-探測光譜顯微術
應用於半導體奈米結構及生物樣本

Pump-probe Spectro-microscopy: From Semiconductor Nanostructures to Biological Samples

黃冠傑

Guan-Jie Huang

指導教授: 朱士維 博士
楊尚達 博士

Advisor: Shi-Wei Chu, Ph.D.
Shang-Da Yang, Ph.D.

中華民國 111 年 12 月

December, 2022

doi:10.6342/NTU202300045

國立臺灣大學博士學位論文

口試委員會審定書

激發-探測光譜顯微術
應用於半導體奈米結構及生物樣本

Pump-probe Spectro-microscopy: From Semiconductor Nanostructures to Biological Samples

本論文係黃冠傑君（F06222014）在國立臺灣大學物理學系、所完成之博士學位論文，於民國 111 年 12 月 19 日承下列考試委員審查通過及口試及格，特此證明

口試委員：朱士維

（指導教授）

謝宇龍　　林宏宗

詹明哲　　楊尚達

Chau-Kong YONG　　李子日

致謝

感謝一路走來，遇見過的所有人。

首先要先感謝我的指導老師朱士維教授，五年來的諄諄教誨，不論是研究上相關的專業知識以及生人經驗分享，都讓我受益匪淺。老師在教導上特別著重於口頭表達能力，能否有邏輯且言簡意賅得表達想法，是我們實驗室一重大的課題。此外，老師也十分注重團隊合作，研究若是單槍匹馬。很容易一股腦兒得就鑽進了死胡同裡了，透過合作可以有不同的看法，問題也更能解決。很感謝老師培養的這些能力，使我在博班路上在跟其他實驗室合作時，能更快融入團體，達成跨領域的合作。再來，我要感謝合作實驗室的老師們，陳學禮教授與萬德輝教授，在碩班時提供許多研究上的建議及方向。中研院的林宮玄博士，在您的實驗室學到許多光學系統架設的能力，帶領我進到了超快領域。清大的楊尚達教授，在您的實驗室架設了整套拉曼系統，也完成一直以來生醫影像的目標。朱麗安教授，感謝每次與您的討論，獨到的見解免去我在研究路上走了許多冤枉路。也十分感謝江安世教授，提供了我在腦科中心實驗的環境，老師的專業團隊製備了各種複雜生物樣品。也要感謝楊超強教授、詹明哲教授、謝佳龍博士，擔任我的口試委員，對於我的博士研究給予肯定及提供指教與建議。

doi:10.6342/NTU202300045

除了老師們，也要感謝實驗室的學長姐們，厚獻、懿修、伯超，帶領我進入奈米粒子的非線性光學領域，教導我基本的對光以及光譜量測。國仁、涵源、裕峰、黃喬，謝謝你們營造實驗室很好的討論氛圍，光學系統的問題找你們討論都可以收斂出明確的方向，問題都能迎刃而解。還有一起奮鬥同儕們，首先是進入實驗室第一個認識的邦漢，謝謝常常當我的垃圾桶，傾聽研究路上的種種抱怨。宇軒，謝謝你精美的光學系統筆記受益良多，光學問題找你討論準沒錯。俊誼、鴻羽、建昇、伯元，謝謝你們常常陪我聊天打屁，一起玩電動、打球等。最後我想感謝我的家人，謝謝你們在我求學階段一路上的支持，使我能無後顧之憂，也感謝一直努力的自己。

doi:10.6342/NTU202300045

中文摘要

激發-探測光譜顯微術結合了遠場光學顯微鏡的成像模式和超快光譜的時間分辨特性，已成爲研究電子和振動動力學的有力技術，在材料科學和生醫影像的應用中日益廣泛。這促使發展激發-探測技術以解析相應的時域及光譜特性。目前激發-探測中的時間分辨特性，主要用以研究載子動力學特性，對超快非線性在時域中的行爲研究較少。至於激發-探測技術中來探究振動特性，由於電子躍遷效率低，其靈敏度往往不足。

本研究在激發-探測光譜學的範疇下，主要拓展兩個研究方向，即探究半導體奈米結構中的超快載子動力學，以探討瞬態非線性行爲，並透過電子預共振效應發展高靈敏度之觀測方法，用以觀測生醫樣品內的振動特性。

本研究的第一部分，利用共軛焦顯微鏡搭配激發-探測的時間分辨特性，對矽奈米結構中的超快載子動力學進行檢測，並揭示了一種基於俄歇機制的瞬態非線性行爲。以往的研究主要集中在多光子吸收、四波混頻等瞬時非線性行爲，即在脈衝持續時間內發生的事件。此研究則展示了瞬態非線性具有非常規的特性，即在非激發-探測光之時間零點，仍具有非線性行為，呈現了各種非線性行爲之間的

doi:10.6342/NTU202300045

時間演化，包括次線性、全飽和、超線性響應。論文的第一部分主要對基於非線性載子動力學引起的瞬態非線性進行了檢測和應用。

在第二部分，我們著重於發展先進的超連續光源來獲取分子的振動信息，此信息提供了化學鍵的成像對比。激發-探測光譜顯微術能夠在不對樣品進行螢光標定的情況下，仍可對化學和生物樣品進行振動特性定位。然而，儘管激發-探測技術具有化學分辨性，目前的靈敏度仍然遠遠落後於螢光技術，源自於雷射的激發能量遠小於激發態與基態的能階差，不能有效地促進振動能階之間的電子躍遷。而發展激發-探測光譜顯微術中的先進光源，有助於優化電子預共振效應，即透過控制激發光之能量接近至樣本之激發能階來增強振動信號。

在本論文所述的研究中，我們開發之激發-探測光譜顯微術用以檢測半導體奈米結構的時域特性以及解析生醫樣品的光譜特性。藉由非線性載子複合過程引起的瞬態非線性之研究，為操縱非線性行爲增加了新的自由度，即藉由時域進行調變。另一方面，對電子預共振效應的研究爲高靈敏度振動譜測量和生醫成像提供了新的思路。

關鍵字：激發-探測光譜顯微術、矽奈米粒子、超快載子動力學、俄歇複合、瞬態非線性、多重薄片超寬頻譜、同調拉曼散射、電子預共振效應

doi:10.6342/NTU202300045

Abstract

Pump-probe spectro-microscopy combining the imaging modality of far-field optical microscopy with the time-resolved property of ultrafast spectroscopy has become a valuable technique for studying electronic and vibrational dynamics toward the growing applications in material science and biomedical imaging. The development of pump-probe techniques to resolve temporal or spectral features is highly desirable. However, current time-resolved spectroscopy mainly focuses on carrier dynamics, and few reports address the ultrafast nonlinear optical behaviors in the temporal domain. As for vibrational properties in pump-probe techniques, they usually suffer from insufficient sensitivity due to low-efficiency electronic transition.

In this study, under the scope of pump-probe spectroscopy, two major aspects are expanded, which are (A) characterizing the ultrafast carrier dynamics in semiconductors nanostructures to explore transient nonlinear behaviors and (B) investigating the vibrational properties of biomedical samples with highly sensitive detection through electronic pre-resonance effects.

doi:10.6342/NTU202300045

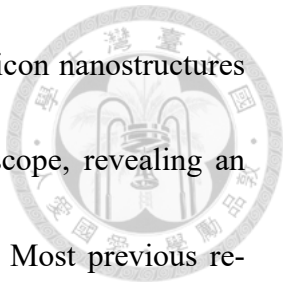

In the first part of the research, ultrafast carrier dynamics of silicon nanostructures are characterized based on a confocal time-resolved spectro-microscope, revealing an unusual transient nonlinear behavior based on Auger mechanisms. Most previous reports mainly focus on instantaneous nonlinear behaviors such as multi-photon absorption and four-wave mixing; that is, the nonlinearities occur within pulses duration. Here, we demonstrate transient nonlinearity featuring an unconventional off-time-zero property and presenting temporal evolution among various nonlinear behaviors, including sub-linear, full-saturation, and super-linear responses. The first part is devoted to the characterization and application of transient nonlinearity based on nonlinear carrier dynamics.

In the second part, we focus on the development of an advanced supercontinuum light source to acquire the vibrational information of molecules, offering the contrast on chemical bonds. Pump-probe spectro-microscopy is capable to perform vibrational mapping of chemicals and biological samples without fluorescence labeling. However, despite the chemical specificity, the sensitivity is still far behind those in fluorescence techniques. This is attributed to the far-off resonance of the laser excitation, not efficiently promoting electronic transition among vibration levels. The development of the advanced light source in pump-probe spectro-microscopy is crucial in optimizing the electronic pre-resonance effects, where vibrational signals are significantly enhanced via tuning laser excitation close to the excited energy levels.

doi:10.6342/NTU202300045

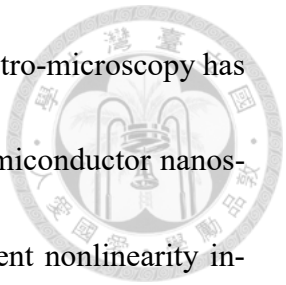

In the research described herein, our developed pump-probe spectro-microscopy has been utilized to characterize the temporal and spectral features in semiconductor nanostructures and biomedical samples, respectively. The study of transient nonlinearity induced by the nonlinear recombination process adds new degrees of freedom in temporally manipulating nonlinear behaviors. On the other hand, the research on electronic pre-resonance effects sheds light on high-sensitive vibrational spectroscopic measurement and biomedical imaging.

Keywords: pump-probe spectro-microscopy, silicon nanostructures, ultrafast carrier dynamics, Auger recombination, transient nonlinearity, multiple-plate continuum, coherent Raman scattering, electronic pre-resonance

doi:10.6342/NTU202300045

Contents

doi:10.6342/NTU202300045

doi:10.6342/NTU202300045

doi:10.6342/NTU202300045

doi:10.6342/NTU202300045

List of Figures

doi:10.6342/NTU202300045

doi:10.6342/NTU202300045

List of Tables

doi:10.6342/NTU202300045

Chapter 1

Introduction

As a pioneer of femtochemistry, Ahmed Hassan Zewail received the Nobel Prize in Chemistry in 1999 for the study of chemical reactions across femtoseconds based on ultrafast pump-probe techniques [1–3]. Pump-probe spectro-microscopy has become an attractive tool for investigating the electronic and vibrational properties of materials [4–10]. Leveraging various nonlinear processes and the unique time-resolved property, pump-probe techniques provide spatial-temporal dynamics characterization, and chemical specificity by probing electronic and vibrational levels of molecules toward the study of material science and biological fields [11–13]. This chapter offers an introduction and motivation for this dissertation. In Sec. 1.1, the general concept and instrumentation strategy of pump-probe spectro-microscopy are introduced. Sec. 1.2 and Sec. 1.3 specialize in the application of pump-probe spectro-microscopy within semiconductors nanostructures and biological samples, respectively. Sec. 1.4 gives an overview of the dissertation.

doi:10.6342/NTU202300045

1.1 Pump-probe Spectro-microscopy

Modern optical nonlinear microscopy accompanied by molecular spectroscopy has been employed to explore the physics of advanced material and reveal unconventional phenomena, facilitating the comprehension of spatial-temporal dynamics as well as molecular structure and function in material science and biological fields [4, 9]. Conceptually, various nonlinear mechanisms such as multiphoton excited fluorescence and high harmonic generation are able to provide distinct contrast in optical spectro-microscopy [14]. As the underlying mechanism and imaging modality vary, different light-matter interactions are taken as the contrast, featuring different physical and chemical properties. For example, second harmonic generation stems from second-order nonlinearity, which is sensitive to materials that present a non-centrosymmetric property [15]. Furthermore, a third-order nonlinearity, coherent Raman scattering effects deduce the vibrational information if the beating frequency of pump and probe pulses matches the vibrational levels.

Among these nonlinear processes, fluorescence and photoluminescence are known as the most prominent contrast in current nonlinear spectro-microscopy, which is popular in biomedical studies [16–18] and advanced semiconductor materials [19, 20] due to its high sensitivity up to a single-molecule level and background-free detection. Despite its success, fluorescence encounter some limitations: (1) Fluorescent molecules have a finite lifetime since a long-time illumination leads to the photo-chemical alteration of the molecules, resulting in loss of fluorescence, i.e., photobleaching. (2) Through non-radiative energy

doi:10.6342/NTU202300045

transfer, fluorescent molecules would form oxygen radicals, which is fatal to bio-samples, i.e., phototoxicity. (3) Most molecular species are intrinsically non-fluorescent and there may be no suitable fluorescent markers for the target species. Therefore, optical spectro-microscopy based on non-fluorescence contrast with high sensitivity is highly desirable in biomedical and materials science.

Unlike fluorescence as an incoherent process, the advent of coherent nonlinear molecular spectroscopy helps to overcome these limitations, where coherent nonlinear processes do not involve non-radiative relaxation pathways, and thus electrons are not allowed to relax via intersystem crossing, i.e. no photobleaching and phototoxicity. Moreover, the coherent nonlinear optical process can provide intrinsic contrast for spectro-microscopic measurements. Usually, those processes are classified into two distinct groups [4, 5, 9]:

1. Parametric generation spectroscopy, in which materials act as a frequency mixer, allowing energy exchange between the incident and resulting light fields. In such a way, materials return to the ground state after the parametric process. This group includes second harmonic generation (SHG), third harmonic generation (THG), and coherent anti-Stokes Raman scattering (CARS).

2. Pump-probe spectroscopy, in which materials exchange energy with incident light fields, resulting in the quantum state of material changed after nonlinear interaction. This group covers stimulated Raman scattering (SRS), excited-state absorption (ESA), stimulated emission (SE), and ground-state depletion (GSD).

doi:10.6342/NTU202300045

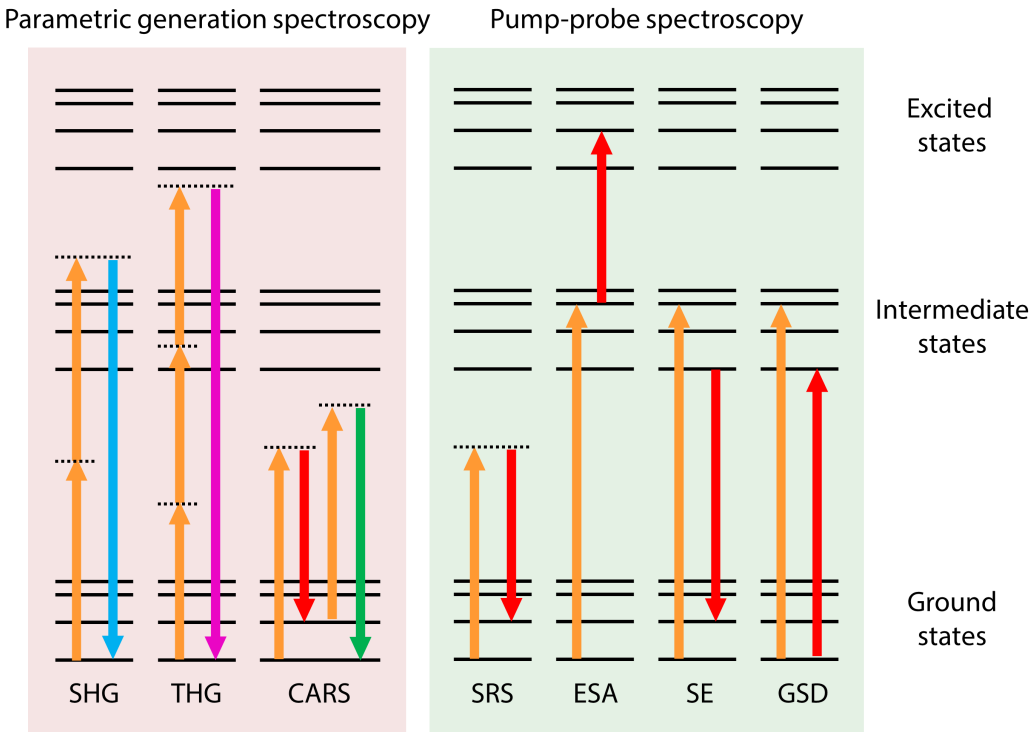

Figure 1.1: Coherent nonlinear mechanisms. SHG: second harmonic generation; THG: third harmonic generation; CARS: coherent anti-Stokes Raman scattering; SRS: stimulated Raman scattering; ESA: excited-state absorption; SE: stimulated emission; GSD: ground-state depletion. Black dashed lines indicate intermediate virtual states.

Figure 1.1 illustrates the energy level diagram for coherent nonlinear mechanisms. On the left side of the dashed line, each parametric process generates a new frequency, which is spectrally separated from the incident radiation using optical filters and detected with a photomultiplier. Except for the CARS process, the remaining parametric processes only involve virtual intermediate states, resulting in the lack of molecular specificity. On the contrary, the pump-probe process carries specific spectroscopic signatures by probing the electronic resonance energy levels and vibrational levels of molecules, thus facilitating the characterization of excited-states dynamics and chemical analysis. Since pump-probe processes do not generate the new frequency, it requires more sophisticated measurement techniques, that is, a modulation transfer scheme.

doi:10.6342/NTU202300045

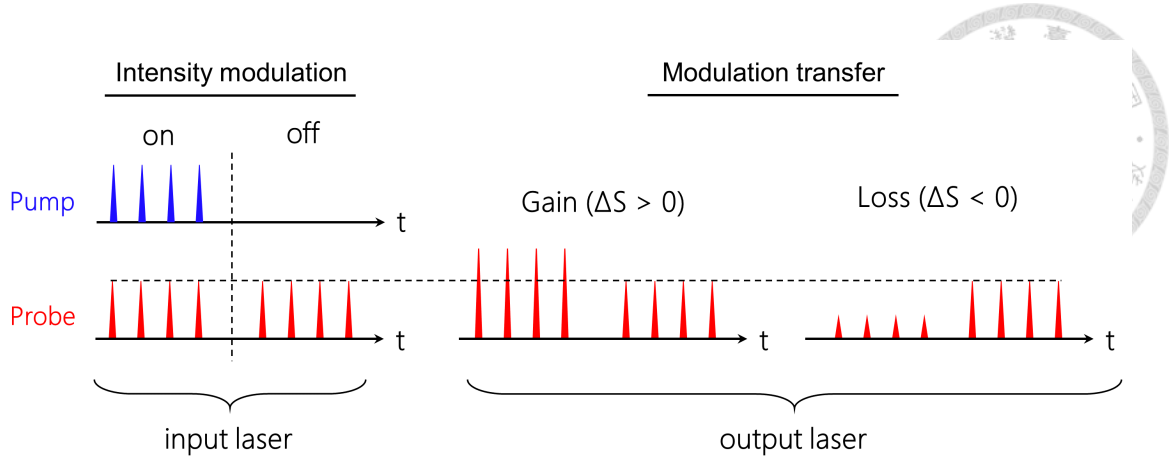

Figure 1.2: Schematic of modulation transfer scheme.

1.1.1 Modulation Transfer Scheme

Figure 1.2 depicts a typical modulation transfer scheme. The incident pump pulse train is imposed by an intensity modulation with a chopper, an electro-optic modulator (EOM), or an acousto-optic modulator (AOM). As the pump-probe nonlinear process requires participation with both pump and probe pulses, the nonlinear signals of interest would carry the modulation profiles in the probe pulse train. The pump transfers its modulation to the probe through transient gain/loss processes, whose signals are then detected by a photodetector and demodulated by a lock-in amplifier.

Since multiple photons participate, the occurrence of different nonlinear effects in the pump-probe process is related to various adjustable parameters, such as excitation wavelengths combination of pump and probe pulses, and the time delay between two pulses. This leads to another unique time-resolved property in the pump-probe techniques, which enables the characterization of vibration motion in the femtochemistry field [1] and ultrafast carrier dynamics in semiconductors [7, 21–26].

doi:10.6342/NTU202300045

1.1.2 Time-resolved Property

Time-resolved property in pump-probe techniques manifests in a way of the time delay between pump and probe pulses. The pump pulse is responsible for the photoexcitation and the probe pulse is accountable for the detection. By tuning the time delay, one can sketch the signal variation as a function of delayed time, where the evolution of pump-probe signals unravels the ultrafast dynamics in the materials. The delayed line is usually controlled by the motorized translation stage with high precision to achieve a femtosecond-scale resolution in each move step. We note that the temporal resolution is defined as the cross-correlation between pump and probe pulses and is usually comparable to the pulse duration themselves [27].

In brief, pump-probe spectro-microscopy combining the coherent nonlinear process as contrast with the unique time-resolved property has facilitated the study of the electronic and vibrational properties of samples in the fields of material science and biology. In the following section, we would specialize the introduction of pump-probe spectro-microscopy in semiconductors nanostructures and biological samples.

doi:10.6342/NTU202300045

1.2 Pump-probe Spectro-microscopy in Semiconductors Nanostructures

The study of ultrafast dynamics in semiconductors has gained lots of attention due to the interest in the direct application of semiconductor devices, which require fast response and high-speed information processing. For semiconductor devices, e.g. transistors, the processing speed is highly related to the structure dimensions. As the length goes down to a few nanometers, the electron transit time can be as short as a femtosecond to a picosecond. This brings out the motivation to characterize the ultrafast dynamics of semiconductors. For example, the carrier transit time of a 125-nm silicon nanodisk has been reported to be 65 fs [25]. Therefore, a fundamental understanding of non-equilibrium carrier dynamics in semiconductors would facilitate the development of high-speed semiconductor devices. Over the past few decades, thanks to pump-probe techniques, ultrafast dynamics covers photoexcited carrier density, and the subsequent carrier recombination process has been well-studied on femtosecond to subpicosecond time scales [11, 28–32].

With the development of nanotechnology, excited-state dynamics of semiconductor nanostructures have recently attracted significant attention due to the ability to modify material features by controlling their dimensionality, morphology, defects, and interface properties, thereby manipulating ultrafast behaviors [7, 22–26]. Moreover, high optical index semiconductor nanostructures, e.g., silicon and germanium with strong field confinement, exhibit more complex optical behaviors, which present electric and magnetic

doi:10.6342/NTU202300045

Mie resonances that can significantly enhance both linear and nonlinear light-matter interactions [33, 34]. Inspired by the time-resolved property in pump-probe techniques and Mie resonance-induced multipole electromagnetic responses in semiconductor nanostructures, we propose and demonstrate the concept of transient nonlinearity based on nonlinear carrier dynamics [35]. For a more detailed theoretical background and experimental demonstration, see chapter 2 and 3, respectively.

1.3 Pump-probe Spectro-microscopy in Biological Samples

The other aspect of pump-probe techniques would focus on the contrast based on the various nonlinear mechanisms, generating coherent nonlinear optical signals. These signals carry specific spectroscopic features via interrogating electronic energy levels or probing the vibrational states of the molecules [9]. Among these nonlinear mechanisms, coherent Raman scattering holds a unique position in that it provides the chemical specificity to probe intrinsic molecular vibrations without exogenous labeling [8, 9, 36]. Typically, vibrational modes have energies in the range of $1-4000\ \mathrm{cm}^{-1}$ that corresponds to the wavelength in the mid-infrared domain ($2.5-10000\ \mu\mathrm{m}$). By switching from mid-infrared to visible excitation, the overwhelming absorption from water molecules is suppressed, making this technique particularly useful for biomedical applications [10, 37–41]. Moreover, benefiting its overall quadratic and cubic dependence on the excitation intensities, a nonlinear CRS process naturally possesses the capability of optical sectioning, allowing

doi:10.6342/NTU202300045

three-dimensional volume imaging. However, despite its prominent chemical specificity, the CRS spectro-microscopy remains a secondary candidate in biomedical applications because of its relatively low sensitivity compared with fluorescence. To further boost the Raman sensitivity, electronic pre-resonance (EPR) is a promising solution to overcome the bottleneck [42–45]. By addressing the pump wavelength close to the absorption peak of the sample, the Raman cross-section could be significantly enhanced [46, 47]. Inspired by the CRS contrast in pump-probe technique and EPR effects to enhance the sensitivity towards biomedical applications, we propose the advanced laser system: double-pass multiple-plate continuum with enough excitation strength to offer sufficient responses and flexible wavelength tuning ability to support desired Raman mode interrogation and EPR detection [48]. For a more detailed theoretical background and experimental demonstration, see chapter 4 and 5, respectively.

1.4 Structure of dissertation

This work aims to apply the pump-probe techniques to both ultrafast carrier dynamics and biomedical imaging. In this dissertation, leveraging the time-resolved property of pump-probe techniques, ultrafast carrier dynamics of silicon nanostructures are investigated and a novel concept of transient nonlinearity generation is presented. In addition, by adjusting the excitation wavelength of pump and probe pulses with ultra-broadband supercontinuum, vibrational information of pure chemicals or biological samples can be probed, allowing coherent Raman scattering bio-imaging without exogenous chemical la-

doi:10.6342/NTU202300045

beling. This dissertation would cover two original publications [35, 48] in chapter 2-5. In these chapters, the background knowledge and relevant theory are given before presenting experimental results. A summary of this dissertation and future outlook are discussed at the end.

Chapter 2 provides the physical principles of ultrafast dynamics in a semiconductor nanostructure as well as the basic Mie scattering theorem. We link the carrier dynamics to the Mie scattering via the key parameter, the refractive index that carrier dynamics induce the refractive index variation, further resulting in the Mie spectrum shift, which alters the optical properties of semiconductors.

Chapter 3 introduces the concept of transient nonlinearity generation, where the underlying mechanism is fluence-dependent carrier lifetime. This effect is exemplified via nonlinear Auger recombination. Auger-induced transient nonlinearity is then applied to the point-spread-function engineer, demonstrating the sub-diffraction imaging.

Chapter 4 provides the physical principles of the Raman effect. By adopting a classical forced damped oscillator model, the theory of spontaneous Raman scattering and coherent Raman scattering is introduced. The electronic pre-resonance (EPR) theorem is also described. This effect is achieved by bringing the excitation wavelength close to the absorption peak of the sample, leading to the enhancement of the Raman cross-section.

Chapter 5 contains the results of coherent Raman spectro-microscopy driven by a double-pass multiple-plate continuum. This ultra-broadband supercontinuum not only provides pump and Stokes beams but also supports dual-wavelength tunability. That is,

doi:10.6342/NTU202300045

two beams can be adjusted independently, facilitating spectroscopic measurement and EPR detection. Its intense octave-spanning spectrum also allows for conducting imaging in biological samples.

Chapter 6 summarizes the entire work. Potential improvement of the system and the future outlook are discussed.

doi:10.6342/NTU202300045

Chapter 2

Ultrafast Carrier Dynamics in Semiconductors Nanostructures

In this chapter, the physics of ultrafast carrier dynamics of semiconductors and Mie theory related to nanostructures scattering are introduced, starting from the photoexcitation and the subsequent carrier recombination process to the Mie spectrum shift resulting in transient signals variation. The key physical parameter: the refractive index helps to link these two mechanisms.

2.1 Introduction

The requirement of fast response and high-speed information processing microelectronics devices has driven the study of ultrafast carrier dynamics in semiconductors, including carrier–carrier scattering, carrier-phonon scattering, and recombination process (Figure 2.1). Typically, these fundamental dynamics occur ranging from femtosecond to

doi:10.6342/NTU202300045

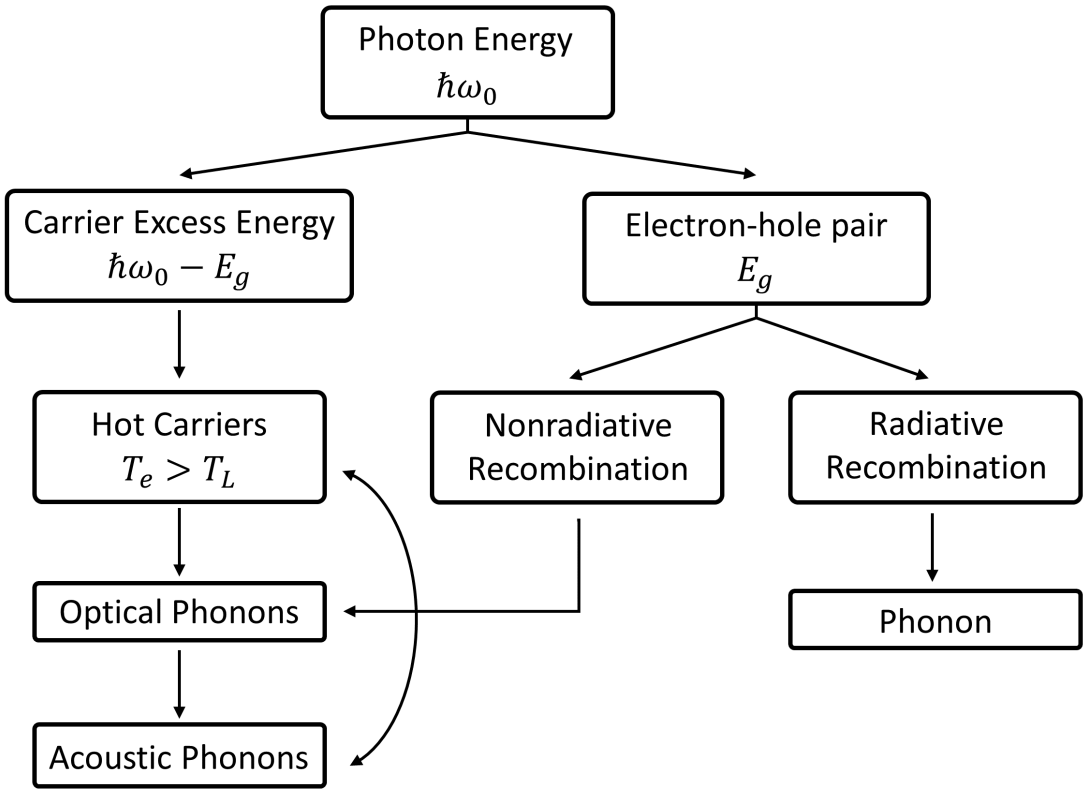

Figure 2.1: Illustration of the flow of the energy in a photoexcited semiconductor.

nanosecond time scale [11, 49]. To resolve the temporal dynamics, the most adopted technique is pump-probe, where the semiconductors are first excited by pump beams, undergoing several states of relaxation before back to the thermodynamic equilibrium. Based on scanning the time delay between pump and probe pulses, ultrafast carrier dynamics are then characterized. In the following sections, we review the primary mechanism of ultrafast carrier dynamics, and specifically, we focus on the case of highly-dense carrier densities ($N > 10^{19}$ cm^{-3}) [50, 51]. In addition, we introduce the concept of pump-probe techniques.

doi:10.6342/NTU202300045

2.2 Photoexcited Carriers Generation and Carrier Thermalization

The ultrashort pulses with photon energy $\hbar\omega_0$ higher than the silicon band gap energy E_g are absorbed either via linear and two-photon interband absorption or free-carrier absorption. Initially, few free-carrier densities are present in the system, and thus the former process dominates, leading to the generation of electron-hole pairs with the kinetic energy $\hbar\omega_0 - E_g$. The photoexcited carrier density can be calculated from [31]

$$N_0 = (1-R_n)F_{eff}(\frac{\alpha}{E_{ph}} + \frac{\beta(1-R_n)F_{eff}}{2E_{ph}\tau_{\text{FWHM}}}) \approx (1-R_n)F_{eff}\frac{\alpha}{E_{ph}} \tag{2.1}$$

where $R_n = 0.328$ is the normal incidence reflectivity of silicon, τ_{FWHM} is the full width at half maximum (FWHM) of the pulse width, F_{eff} represents the incident laser fluence, α is the linear absorption coefficient [52], and $\beta = 6.8$ cm/GW is the two-photon absorption parameter. In the comparison of the linear and two-photon absorption processes, linear absorption dominates to generate the carrier density. Therefore, the portion of two-photon absorption is negligible. In addition, in the case of nanostructures, the value of α has an order of magnitude larger than the bulk silicon, estimated to be $\alpha_{nano} \sim 10^4$ cm^{-1}.

Subsequently, the electrons and holes thermalize with other carriers for the transition from a non-thermal regime to a hot-carrier regime [49]. Note that in the non-thermal regime, the distribution function of carriers is not able to be characterized by a temperature. Within $\sim 10^{-13}$ s, electron-electron and hole-hole collisions bring the electrons

doi:10.6342/NTU202300045

and hole into thermalized Fermi–Dirac distributions with the characterized temperature T_e and T_h, respectively. Then, within $\sim 10^{-12}$ s, electron-hole scattering thermalize two separated carriers system into a common carrier temperature $T_e = T_h$. In the process of carrier thermalization, the carrier energy does not transfer to the lattice, so typically carrier temperature is initially higher than the lattice temperature T. At the end of the hot-carrier regime, the carriers relax via optical phonon emission, and the optical phonons decay by the emission of acoustics phonons, bringing phonons into equilibrium with the lattice [53]. But still, in comparison to thermodynamic equilibrium, there are extra electrons and holes present in the conduction and valence bands. The excess electron-hole pairs then recombine in either radiative or non-radiative ways (Figure 2.1). In brief, as time evolves, the carrier energy attempt to transfer the kinetic energy to the lattice through various scattering and recombination mechanisms.

2.3 Carriers Recombination Process

After the carrier thermalization, both electrons and holes share the common carrier temperature. To characterize the relationship between these two levels, we have to consider the recombination process, further relaxing the energy and reducing the carrier densities. The recombination process is classified into radiative and non-radiative ways. The time scale for radiative recombination in direct band gap semiconductors is hundreds of picoseconds to nanoseconds, while in indirect band gap semiconductors it is microseconds to milliseconds. On the other hand, the non-radiative recombination occurs on the

doi:10.6342/NTU202300045

time scale of tens to hundreds of picoseconds in indirect band gap semiconductors [22]. Consider our observation time scale and the measured samples (silicon). Here, we only consider non-radiative recombination.

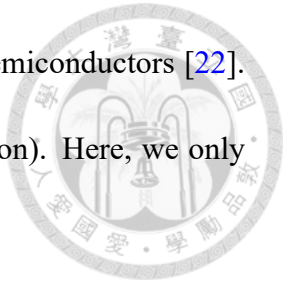

In general, the spatiotemporal evolution of carrier density N is governed by two processes: diffusion and recombination, written by

$$\frac{dN(z,t)}{dt} = D\frac{\partial^2 N(z,t)}{\partial z^2} - \frac{N(z,t)}{\tau_{\text{eff}}} \tag{2.2}$$

where D is the diffusion coefficient and τ_{eff} is the effective lifetime of various recombination processes. In the case of nanostructures, spatial confinement suppresses the carrier diffusion process [54]. The first term in Eq. 2.2 is ignored and the recombination processes are described by the polynomial function of carrier density N, written by

$$\frac{dN(z,t)}{dt} = -\frac{N(z,t)}{\tau_{\text{eff}}} = -AN - BN^2 - CN^3 \tag{2.3}$$

where the first term is the Shockley-Read-Hall (SRH) term, the second term is the bimolecular recombination with radiation emission, and the third term represents Auger recombination [55–57]. SRH is typically the dominant recombination process in indirect band gap semiconductors like silicon. As the carriers recombine, the energy is released via phonon emission. The bimolecular recombination occurs in direct band gap semiconductors, and the band-to-band recombination is accompanied by photon emission [58]. For high carrier density ($N > 10^{19}$ cm^{-3}), the Auger process becomes the dominant recombination process [50]. This process involves the transfer of recombination energy from an

doi:10.6342/NTU202300045

electron-hole pair to a third carrier, which is excited to a higher energy state. Equation 2.3 also highlights that in low carrier density, carriers primarily recombine in the SRH channel and typically τ_{eff} stays constant, while in high carrier density, τ_{eff} is carrier-density dependent, reducing with increasing carrier density.

In our work, we manipulate in the condition of high carrier density of silicon sample ($N \approx 10^{20} - 10^{21}$ cm^{-3}) [35]. Therefore, Auger recombination is the dominant process. Eq. 2.3 is then recast as

$$\frac{dN}{dt} = -CN^3 \tag{2.4}$$

with an analytic solution [59]

$$N(t) = \frac{N_0}{\sqrt{1 + 2CN_0^2 t}} \tag{2.5}$$

where N_0 is the carrier density that is photoexcited by the optical pulses at time zero and C represents the Auger coefficient. Moreover, we introduce the Auger lifetime, defined by

$$\tau_{\text{Auger}} = -N \left(\frac{dN}{dt} \right)^{-1} \Bigg|_{t=0} = \frac{1}{CN_0^2} \tag{2.6}$$

However, as the carrier density is high enough ($N_0 \sim 10^{21}$ cm^{-3}), screen effects of Coulomb interaction need to take into consideration, and the rate equation in Eq. 2.4 has to be modified as [50, 60]

$$\left(\frac{\partial N}{\partial t} \right)_{\text{Auger}} = -\frac{CN^3}{\left(1 + (\lambda/k_g)^2\right)^2} \tag{2.7}$$

doi:10.6342/NTU202300045

where λ is the screening wave vector and k_g is the wave vector corresponding to the recombination transition (energy band gap). Similarly, following the Eq. 2.6, the modified Auger lifetime is derived as

$$\tau_{\text{Auger}} = -N \left(\frac{\partial N}{\partial t} \right)^{-1}_{\text{Auger}} \Bigg|_{t=0} = \frac{1}{C N_0^2} \left(\frac{\lambda^4}{k_g^4} + 2 \frac{\lambda^2}{k_g^2} + 1 \right) \tag{2.8}$$

The high carrier temperature leads to nondegeneracy so that $\lambda^2 \sim N_0$. Without loss of generality, we assume that carrier density N_0 is linearly proportional to the excitation fluence F. Equation 2.8 can thus be rewritten as

$$\tau_{\text{Auger}} \sim \frac{1}{C' F^2} \left(\frac{F^2}{k_g^4} + 2 \frac{F}{k_g^2} + 1 \right) = a + \frac{b}{F} + \frac{c}{F^2} \tag{2.9}$$

Note that as increasing the fluence, the Auger lifetime decreases asymptotically to a constant "a", which refers to saturation lifetime. Overall speaking, understanding the carrier dynamics and the carrier density evolution function helps to interpret the behaviors of transient signals in pump-probe spectroscopy. In the following section, we link the carrier dynamics to transient signals, where the key physical parameter is the refractive index.

2.4 Carrier Dynamics Induced Refractive Index Variation

The photo-induced refractive index change Δn is usually described with two physical parameters: carrier density N and lattice temperature T, corresponding to the effects of

doi:10.6342/NTU202300045

carrier evolution and lattice heating [29, 30]. The refractive index change is given as

$$\Delta n = \Delta n_N + \Delta n_{\Delta T} \tag{2.10}$$

According to the classical Drude model, carrier densities inducing refractive index change can be written as [30]

$$\Delta n_N = -\frac{Ne^2}{2n_0 m^*_{eh} \epsilon_0 \omega^2} \leq 0 \tag{2.11}$$

where e is the electron charge, n_0 is the refractive index without perturbation, m^*_{eh} is the reduced mass of electrons and holes, ϵ_0 is the vacuum dielectric constant, and ω is the angular frequency of optical fields. Equation 2.11 highlights that carriers provide a negative contribution to the refractive index. On the contrary, lattice temperature provides the variation of refractive index in a positive manner, given as

$$\Delta n_{\Delta T} = \left(\frac{\partial n}{\partial T}\right) \Delta T \geq 0 \tag{2.12}$$

Lattice heating stems from two sources: direct heating and Auger heating. Direct heating stems from the emission of optical phonons by photoexcited carriers, which are allowed to relax toward the band edge on the time scale of a few picoseconds. On the other hand, Auger heating results from Auger recombination, which leads to reheating the electronic systems. In principle, it slows down the carrier relaxation process, remaining hundreds of picoseconds [61]. For the high carrier density $N > 10^{20}$ cm^{-3}, band-filling effects reduce the portion of the direct heating process to less than 15 % of the incident photon energy, and thus Auger heating dominates the lattice heating process [29, 62]. So far, refractive index

doi:10.6342/NTU202300045

variation induced by carrier density N and lattice temperature rise ΔT is discussed. The change in the refractive index will affect the spectrum profile of nanostructures according to the Mie theory, further leading to the deviation of transient signals.

2.5 Refractive Index Variation Induced Mie Spectrum Shift

In this section, we briefly introduce the Mie theory to interpret the relationship between the change of refractive index and the Mie spectrum shift. Mie theory is used to describe the scattering of the light fields by a spherical particle with a different refraction index from the surrounding [63]. Compared with the well-known Rayleigh scattering, Mie theory deals with the case that the wavelength of light fields is comparable to the size of the scattering particles. Here, rather than deriving the theory from the basic Maxwell's equation, we highlight some crucial formulas to interpret the fundamental concept. To begin with, consider a spherical particle with radius a (labeled 1) isolated in the host medium (labeled 2) as shown in Fig. 2.2. The incident optical field is assumed to be a plane wave with wavelength λ_2, angular frequency ω, propagation direction $\mathbf{u}$, and polarization $\mathbf{e}$. The electromagnetic field is thus given by

$$\begin{aligned} \mathbf{E}_{\text{inc}}(\mathbf{r},t) &= E_0 \exp[i(k_2\mathbf{u}\cdot\mathbf{r}-\omega t)]\mathbf{e} \\ \mathbf{H}_{\text{inc}}(\mathbf{r},t) &= \frac{k_2}{\mu_2\omega}[\mathbf{u}\times\mathbf{E}_{\text{inc}}(\mathbf{r},t)] \end{aligned} \tag{2.13}$$

where E_0 is the amplitude of $\mathbf{E}_{\text{inc}}(\mathbf{r},t)$, μ_2 is the magnetic permeability, and k_2 is the wavenumber of the host medium. The analytic form of the scattered electric field $\mathbf{E}_{\text{sca}}(\mathbf{r})$

doi:10.6342/NTU202300045

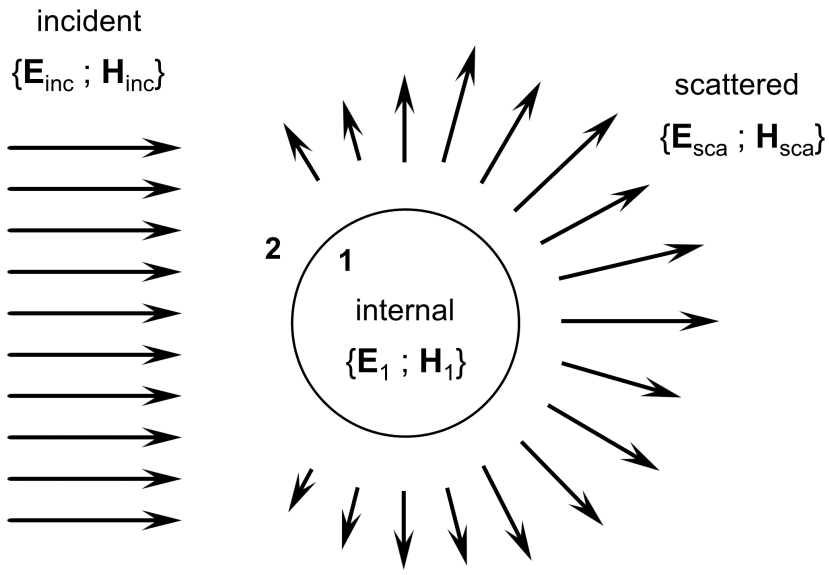

Figure 2.2: Incident light fields scattered by a spherical particle. $\{\mathbf{E}_{\text{inc}}; \mathbf{H}_{\text{inc}}\}$ and $\{\mathbf{E}_{\text{sca}}; \mathbf{H}_{\text{sca}}\}$ refer to incident and scattered electromagnetic fields in the host medium. $\{\mathbf{E}_1; \mathbf{H}_1\}$ is the internal fields of the sphere particle.

can be further derived under the continuity condition at the interface and far-field approximation, written as [63, 64]

$$\begin{aligned}
\mathbf{E}_{\text{sca}}(r,\theta,\phi) &= \sum_{n=1}^{\infty} E_n \left[ia_n \mathbf{N}_{e1n}^{h2}(r,\theta,\phi) - b_n \mathbf{M}_{o1n}^{h2}(r,\theta,\phi)\right] \\
\mathbf{H}_{\text{sca}}(r,\theta,\phi) &= \frac{k_2}{i\omega\mu_2} \sum_{n=1}^{\infty} E_n \left[ia_n \mathbf{M}_{e1n}^{h2}(r,\theta,\phi) - b_n \mathbf{N}_{o1n}^{h2}(r,\theta,\phi)\right]
\end{aligned} \tag{2.14}$$

The notation in Eq. 2.14 is explained below:

- The coefficients E_n are related to the amplitude of electromagnetic fields, which are

$$E_n = i^n E_0 \frac{2n+1}{n(n+1)} \tag{2.15}$$

- Two sequences a_n and b_n are known as Mie sequences, weighting the contribution of electromagnetic normal modes, expressed by

doi:10.6342/NTU202300045

$$a_n = \frac{m\psi_n(mx)\psi_n'(x) - \psi_n(x)\psi_n'(mx)}{m\psi_n(mx)\xi_n'(x) - \xi_n(x)\psi_n'(mx)}$$
$$b_n = \frac{\psi_n(mx)\psi_n'(x) - m\psi_n(x)\psi_n'(mx)}{\psi_n(mx)\xi_n'(x) - m\xi_n(x)\psi_n'(mx)} \tag{2.16}$$

where $\psi_n(\rho)$ and $\xi_n(\rho)$ are the Ricatti-Bessel functions.[1] The quantity x is defined by $x = k_2 a$, the product of the wavenumber and the radius of the particle. It is dimensionless and referred to as a size parameter. The quantity m is also dimensionless, describing the contrast of the complex optical index[2] between the spherical particle and the host medium, defined by $m = m_1/m_2$. Equation 2.16 highlights that Mie coefficients a_n and b_n are determined by two dimensionless parameters: size parameter x and optical index contrast m, providing the viewpoint that Mie scattering profiles are size- and refractive index dependent.

- The functions $\mathbf{M}^{h2}_{e1n}(r,\theta,\phi)$, $\mathbf{M}^{h2}_{o1n}(r,\theta,\phi)$, $\mathbf{N}^{h2}_{e1n}(r,\theta,\phi)$, and $\mathbf{N}^{h2}_{o1n}(r,\theta,\phi)$ are vector spherical harmonics, whose analytic expression is provided in Ref. [64]. These functions are also known as the electromagnetic normal modes of the spherical particle [65]. For a_n series, they are related to electric multipoles. On the other hand, the b_n series describe magnetic multipoles.

Moreover, the scattering cross-section can be derived as

$$C_{sca} = \frac{2\pi}{k_2^2}\sum_{n=1}^{\infty}(2n+1)(|a_n|^2 + |b_n|^2) \tag{2.17}$$

[1] The Ricatti-Bessel functions are defined by $\psi_n(\rho) = \rho j_n(\rho)$ and $\xi_n(\rho) = \rho h_n(\rho)$, where $j_n(\rho)$ and $h_n(\rho)$ is the spherical Bessel and Hankel functions.

[2] The complex optical index is expressed by $m = n + i\chi$, where n is the refractive index and χ is the extinction index.

doi:10.6342/NTU202300045

We can also derive the scattering cross-section of the first four multipoles, which are

$$
\begin{aligned}
C_{sca}^{\mathrm{ED}} &= \frac{6\pi}{k_2^2}|a_1|^2 \\
C_{sca}^{\mathrm{MD}} &= \frac{6\pi}{k_2^2}|b_1|^2 \\
C_{sca}^{\mathrm{EQ}} &= \frac{10\pi}{k_2^2}|a_2|^2 \\
C_{sca}^{\mathrm{MQ}} &= \frac{10\pi}{k_2^2}|a_2|^2
\end{aligned}
\tag{2.18}
$$

where ED, MD, EQ, and MQ represent the electric dipole, magnetic dipole, electric quadrupole, and magnetic quadrupole, respectively. Figure 2.3a provides an example of the multipole decomposition of scattering cross-section. We simulate a nanosphere with a diameter of 150 nm and refractive index $n_1 = 4$ embedded with the host medium with refractive index $n_2 = 1$ and Eq. 2.18 helps to calculate the contribution from each mode. Figure 2.3b and 2.3c show that the scattering cross-section varies under the different diameters of a nanosphere and refractive index. As the refractive index or diameter increases, the peaks of scattering spectra exhibit a redshift.

So far, we introduce the fundamental concept of Mie theory that two key parameters: size parameter x and optical index contrast m determine the Mie coefficients and Mie spectrum profile. We note that the analytical solution of Mie theory is only valid in the case of a nanosphere. Thus, numerical methods must have to be introduced to deal with non-spherical structures. The main idea highlighted in this section is that the variation of refractive index leads to the Mie spectrum shift as shown in Fig. 2.3c. The variation of the refractive index may be affected by carrier density and lattice temperature, resulting

doi:10.6342/NTU202300045

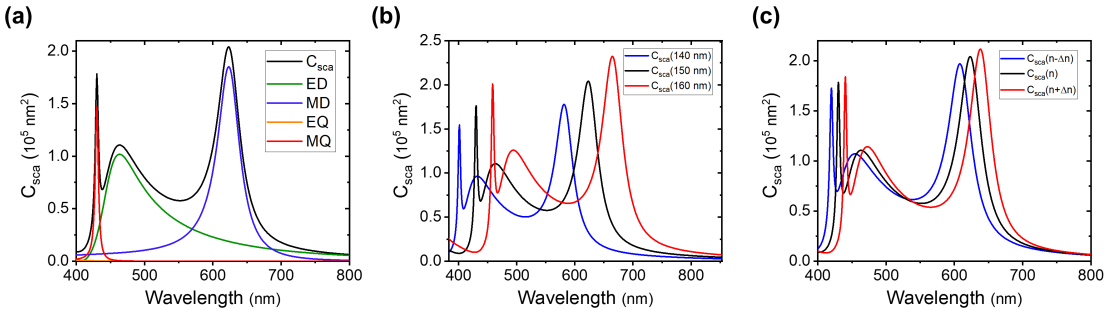

Figure 2.3: The simulation of Mie scattering cross-section. (a) Multipole decomposition of scattering cross-section by nanosphere with diameter 150 nm and refractive index 4. The solid lines correspond to electric dipole (ED), magnetic dipole (MD), electric quadrupole (EQ), magnetic quadrupole (MQ), and total scattering cross-section. (b) Scattering cross-section by nanosphere with various diameters: 140, 150, and 160 nm with the fixed refractive index 4. (c) Scattering cross-section by nanosphere with various refractive index: 3.9, 4.0, and 4.1 with the fixed diameter 150 nm. All scattering spectra are calculated by a Python package: *PyMieScatt*.

in the change of transient signals in pump-probe spectroscopy. By probing the evolution of transient signals in pump-probe spectroscopy, we can then speculate on the underlying carrier dynamics.

doi:10.6342/NTU202300045

Chapter 3

Transient Nonlinearities in Silicon Nanostructures

In this chapter, the concept of transient nonlinearity is first introduced. Auger-induced transient nonlinearity in silicon nanostructures is exemplified to prove the concept, whose nonlinear behavior is characterized by intensity-scan and pump-probe techniques to acquire spatiotemporal information. The temporal evolution of Auger-induced transient nonlinearity and its related application are demonstrated and discussed.

3.1 Introduction

Thanks to its natural abundance on earth and mature fabrication engineering, silicon (Si) has long been a preferred material in the microelectronics industries. This prominent position leads to great success in applications such as diodes, detectors, and transistors in electronic fields. However, the optical properties of Si are relatively poor due to its

doi:10.6342/NTU202300045

indirect bandgap nature and weak nonlinear light-matter interactions, which restrict efficient light emission. Recent developments of Si nanostructures are starting to change the picture owing to the high refractive index of Si ($n \sim 4$) and nanoscale light confinement [33, 66, 67]. The strong spatial confinement and field localization helps to enhance the intrinsically weak optical nonlinearity, facilitating various nonlinear effects such as multiphoton absorption [25, 68], harmonic generation [69], and photothermal effects [70, 71], leading to the emerging fields, nonlinear Si nanophotonics [33, 72] with applications such as all-optical signal processing, super-resolution imaging, and wavelength conversion.

Traditionally, the characterization of optical nonlinearity is based on intensity-scan techniques, e.g. z-scan [73, 74]. A single laser beam is first tightly focused in the z-axis to provide z-dependent intensity illumination. Then, the sample moves along the propagation direction (z-axis) and z-dependent transmittance or divergence in the far field is measured. When there is z-dependent divergence/transmittance, the real/imaginary nonlinear susceptibility of the sample is expected to be observed and can be quantitatively deduced (Figure 3.1a). However, the z-scan method is suitable for the thin sample. If the sample is not uniformly distributed in the transverse direction, like an array of nanoparticles, the resulting nonlinear contribution is an ensemble contribution. To address this issue, our group recently announces another intensity-scan method called the x-scan method, which is specifically designed for analyzing isolated nanoparticles [70, 75], based on the lateral laser scanning in both the x and y axis to acquire the emission pattern of nanostructures. If there is no nonlinear response, the resulting image is simply the linear convolution of the nanostructures and laser point spread function (PSF), where its profile is often a Gaussian

doi:10.6342/NTU202300045

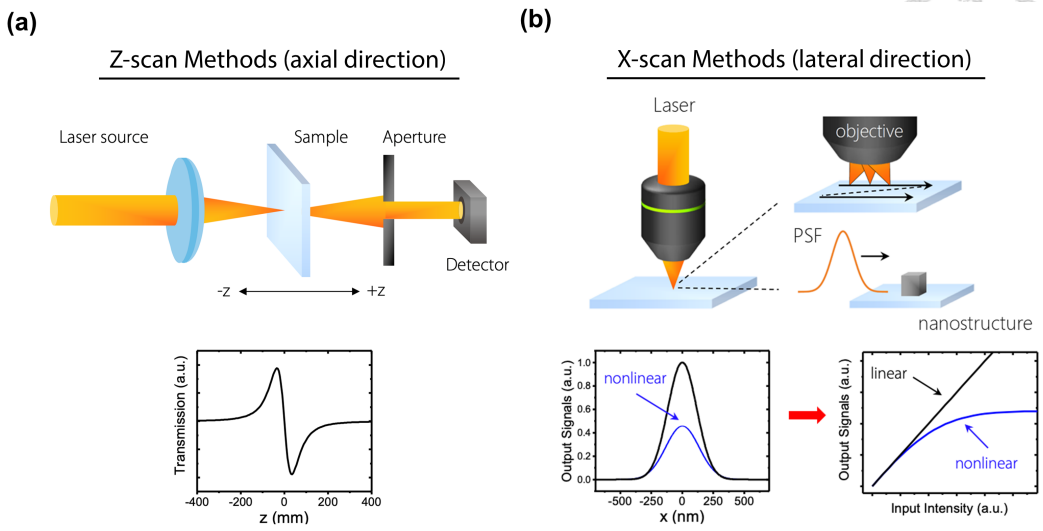

Figure 3.1: Schematic of intensity-scan methods. (a) z-scan methods. (b) x-scan method. PSF: point spread function.

function (Figure 3.1b). On the contrary, if the nanostructure presents nonlinear behavior, the emission image will differ from its original Gaussian profile, and this deformation is exactly related to the nonlinear index [76, 77]. Nevertheless, intensity-scan methods limit the nonlinearity characterization in the spatial domain and they are not capable of exploring the transient nature.

To resolve the temporal responses, especially in the ultrafast domain, the most commonly adopted method is pump-probe techniques, probing the dynamics by scanning the time delay between two pulses [23, 78]. In most cases, linear transient responses are characterized by the pump-probe scheme, including stimulated emission [79], excited-state absorption [80], and ground-state depletion [81]. In addition, the study of nonlinear transient effects has been reported based on the mechanism such as absorption saturation [82], four-wave mixing [83], and multiphoton absorption [84]. Typically, most transient signals are instantaneous, occurring within the pulse duration, and have a solitary nonlinear power dependency (square, cubic, etc.).

doi:10.6342/NTU202300045

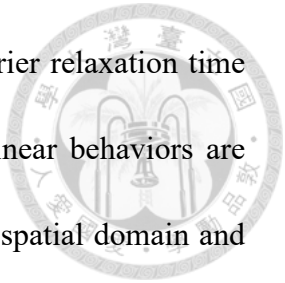

Here, we present a new concept based on fluent-dependent carrier relaxation time to generate transient nonlinearity in Si nanostructures, whose nonlinear behaviors are characterized by the combination of intensity x-scan methods in the spatial domain and pump-probe techniques in the temporal domain. It is well-known that carrier relaxation depends on the recombination processes via, for example, Shockley-Read-Hall (SRH) effects and Auger recombination (AR) [57, 85]. If the carrier relaxation time exhibits fluence-dependent property, we speculate that transient nonlinearities with either sub-linear or super-linear properties would emerge at a certain time delay t_D. Note that previous research mainly focuses on the study of the characteristic relaxation time as a function of fluence and few studies report the nonlinear behaviors at different temporal intervals.

In this chapter, a general concept of the transient nonlinearity generation based on fluence-dependent lifetime is introduced. As a proof-of-concept experiment, transient nonlinearity in Si nanostructures is exemplified through the nonlinear Auger process. Moreover, Auger-induced transient nonlinearity is further applied to microscopic imaging, resulting in the broadening and shrinking of single-particle images. All of the contents in this chapter have been published in *Advanced Optical Materials*, 10(5):2101711, (2022).

3.2 Concept of Transient Nonlinearity Generation

In a pump-probe experiment, transient nonlinear behaviors are characterized by the transient signals as a function of pump fluence. Consider the general case of the transient nonlinearity induced by the fluence-dependent carrier recombination lifetime. According

doi:10.6342/NTU202300045

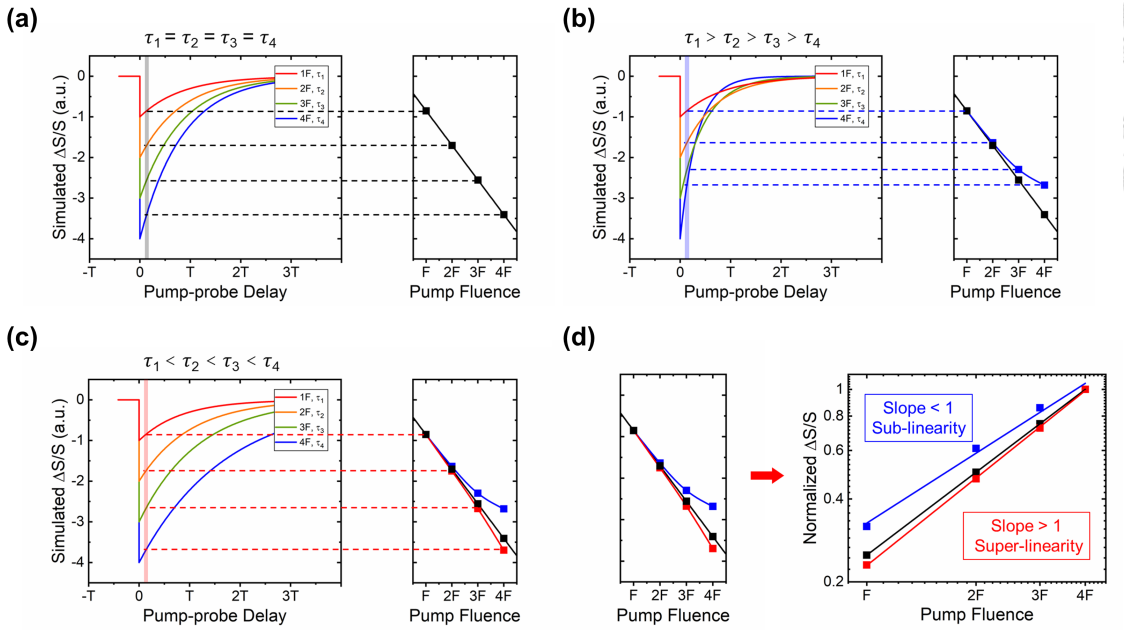

Figure 3.2: Concept of fluence-dependent carrier lifetime inducing transient nonlinear behaviors. (a)-(c) Simulated pump-probe traces with constant (a), decreasing (b), and increasing (c) carrier lifetimes at various pump fluences (F, $2F$, $3F$, $4F$). (Right) Transient signals as a function of fluences at a specific time delay to show linear (a), sub-linear (b), and super-linear (c) fluence dependencies. (d) Pump fluence dependence of normalized transient signals in a logarithmic scale, corresponding to (a)-(c).

to Eq. 2.3, the effective carrier recombination time τ_{eff} is given as

$$\frac{1}{\tau_{\text{eff}}} = AN + BN^2 + CN^3 \tag{3.1}$$

where N is the carrier density. A, B, and C refer to SRH, bimolecular recombination, and Auger effects, respectively. It is obvious that for low carrier density, i.e., low pump fluence, τ_{eff} is constant, leading to the exponential decay of carrier densities over time. While for high carrier density, τ_{eff} is carrier-density/fluence dependent, reducing with increasing pump fluence.

To present the general scenario of how non-constant τ_{eff} generates transient nonlinearity, we start by simulating the pump-probe traces with four carrier lifetimes ($\tau_1, \tau_2, \tau_3, \tau_4$)

doi:10.6342/NTU202300045

under four different pump fluences ($F - 4F$) with three conditions. Figure 3.2a shows the case of constant τ_{eff} over various pump fluences, leading to a linear pump fluence dependency. In Fig. 3.2b, carrier lifetime τ_{eff} decreases with the increasing pump fluences ($\tau_1 > \tau_2 > \tau_3 > \tau_4$) that transient signals $|\Delta S/S|$ reduce as increasing pump fluences, leading to the sub-linear behaviors. On the other hand, in Fig. 3.2c, carrier lifetime τ_{eff} increases with the increasing pump fluences ($\tau_1 < \tau_2 < \tau_3 < \tau_4$) and the transient signals exhibit a super-linear fluence dependency. Figure 3.2d depicts the fluence dependency of normalized transient signals, where nonlinear behaviors are quantified through the slope of pump-fluence dependence in a logarithmic scale: linearity (slope = 1), sub-linearity (slope < 1), and super-linearity (slope > 1), manifesting that transient nonlinearity is a universal incident under the condition of fluence-dependent carrier lifetimes τ_{eff}.

As mentioned in Sec. 2.3 and Eq. 3.1, usually the carrier lifetime is not constant at high-fluence excitation and transient nonlinearity is expected. In the following section, Auger-based nonlinear carrier dynamics in Si nanoblocks (SiNBs) are taken as a proof-of-concept experiment to verify our idea.

3.3 Experimental Methods and System Performance

3.3.1 Experimental Setup

Figure 3.3 shows a schematic of the home-built pump-probe confocal microscope. The front-end laser was a Ti:Sapphire oscillator (Tsunami 3960C-15HP, Spectra-Physics),

doi:10.6342/NTU202300045

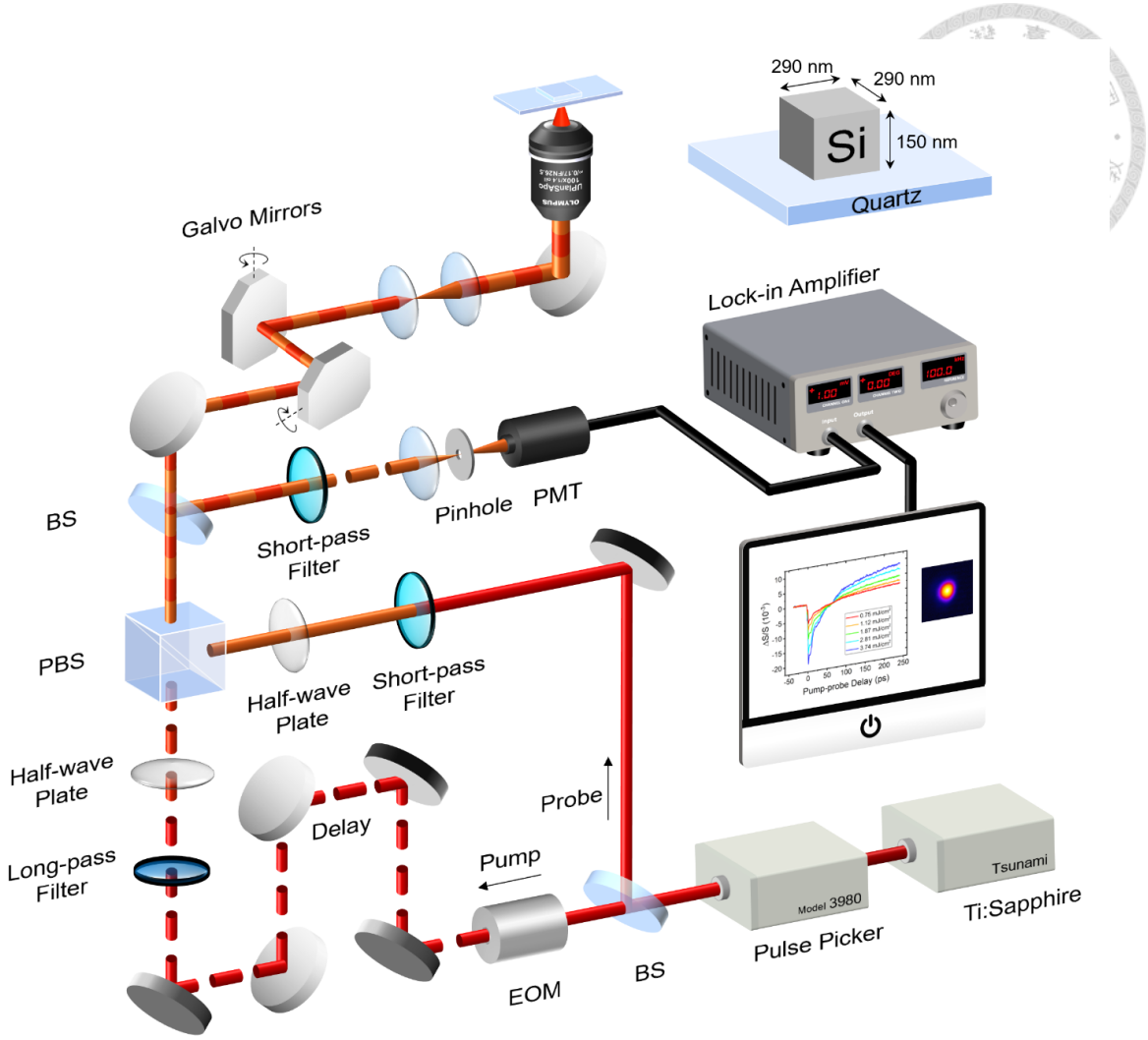

Figure 3.3: Schematic of the confocal pump-probe microscope. BS: beam splitter, PBS: polarized beam splitter, EOM: electro-optic modulator, PMT: photomultiplier tube.

providing a pulse train at 785 nm with an 80-MHz repetition rate. To avoid heat accumulation in the damage to the Si sample, the repetition rate was reduced to 8 MHz with a pulse picker (Model 3980, Spectra-Physics). Pulses were divided into pump and probe beam paths using a 50/50 beamsplitter. The intensity of the pump was modulated by an electro-optical modulator (Model 25D, Conoptics) at a frequency of 100 kHz. A linear motor stage (M-ILS150PP, Newport) served as an optical delay line that offers a time delay between pump and probe pulses. A long-pass filter (LP02-785RE-25, Semrock) and a short-pass filter (SP01-785RU-25, Semrock) were used to select the excitation spectra of the pump

doi:10.6342/NTU202300045

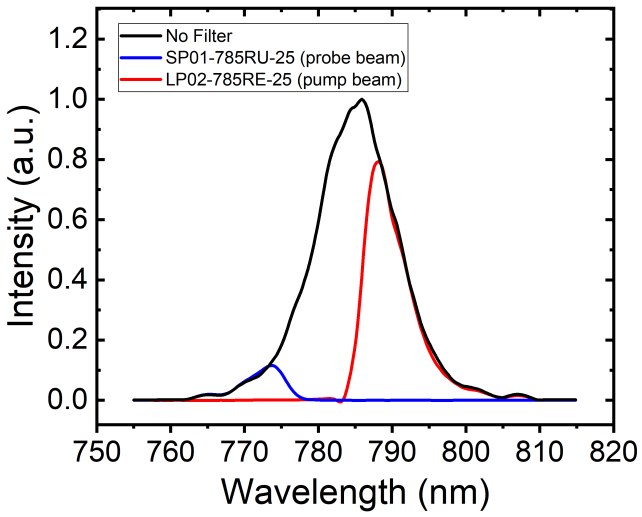

Figure 3.4: Spectra of pump and probe pulses.

and probe pulses and avoid spectral overlap (Figure 3.4). Pump and probe beams were coupled collinearly with a polarized beam splitter. Half-wave plates (10RP02-46, Newport) in individual light paths were used to change the polarization direction and adjust the excitation fluence on the sample. Subsequently, two beams were directed onto galvanometric mirrors (GVS002, Thorlabs) to perform a raster scan. A 100x oil immersion objective (UPLSAPO 100XO NA1.4, Olympus) was used to focus laser beams on samples. Backward scattering was reflected by a beamsplitter, spectrally blocked the pump beam using a short-pass filter (SP01-785RU-25, Semrock), and then focused into a pinhole in front of a photomultiplier tube PMT(R928, Hamamatsu). The photocurrent from the detector was then sent into a lock-in amplifier (SR844, Stanford Research), which was phase-locked to the modulation frequency of EOM (100 kHz) in order to demodulate the pump-probe signals, i.e., ΔS. The backward scattering S intensity of the probe beam which was not experienced by the pump beam was measured using another lock-in amplifier (SR830, Stanford Research) while the probe beam was mechanically chopped at 320

doi:10.6342/NTU202300045

Hz. Time-resolved signals $\Delta S/S$ were then calculated. Through raster scanning mode, pump-probe images were formed at a specific pump-probe delay.

3.3.2 System Performance

In the pump-probe system, the most important factor, temporal resolution is necessary to be clarified to ensure the viability before conducting the experiments. Optical autocorrelator is well-known for the measurement of the duration of ultrashort pulses, which determines the temporal resolution. Figure 3.5a displays a schematic of a second harmonic generation (SHG) intensity autocorrelator. The beam is first split into two pulses train and the time delay between two replicas of the pulse is controlled by a delay stage. Two parallel beams are then focused on a crystal to generate a delay-dependent SHG signal. This signal is collected with a photodetector, which measures

$$I_{SHG} = \int_{-\infty}^{+\infty} |\mathbf{E}(t)\mathbf{E}(t-\tau)|^2 dt = \int_{-\infty}^{+\infty} I(t)I(t-\tau)\, dt \tag{3.2}$$

, where I_{SHG} is the intensity autocorrelation function and $\mathbf{E}(t)$ is the complex electric fields. The temporal resolution is then determined by the intensity autocorrelation bandwidth as shown in Fig. 3.5b. For our pump-probe system, temporal resolution is calculated to be 1.25 ps with a Gaussian fitting.

doi:10.6342/NTU202300045

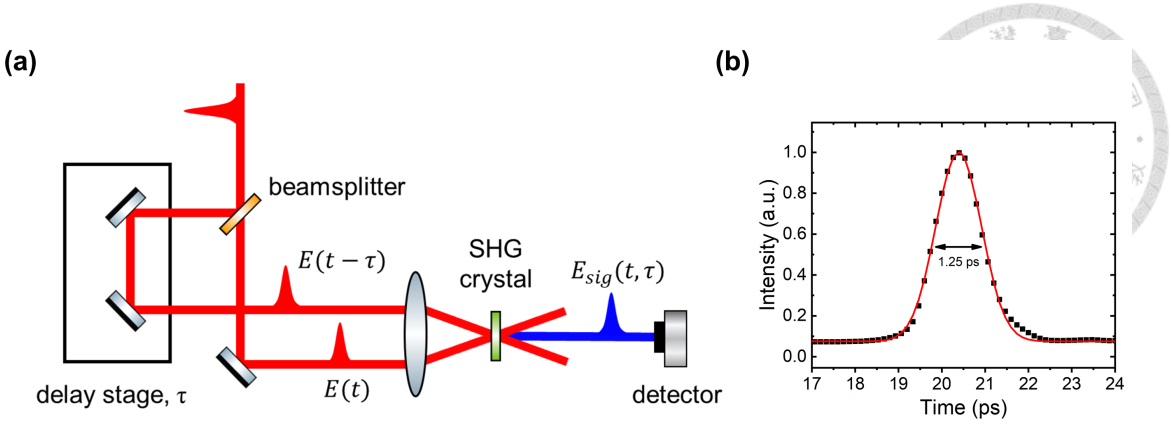

Figure 3.5: Intensity autocorrelator for pulse characterization. (a) Schematic of an intensity autocorrelator. SHG: second harmonic generation. (b) SHG intensity autocorrelation trace. The temporal resolution is calculated to be 1.25 ps (FWHM of the trace).

3.3.3 Fabrication process of SiNBs

The fabrication process of SiNBs was reported [34]. A 150-nm thick chemical resists was spin-coated on a Si layer with a thickness of 150 nm on a quartz substrate. Custom shapes were drawn on the chemical resist using electron beam lithography (ELS-7700T, ELIONIX Inc.). A 30-nm thick Cr layer was then applied as a hardmask using a heat-resistant evaporator, and the chemical resist was removed in a lift-off process. Then, reactive ion etching methods with SF_6 and C_4F_8 plasma were used to remove the Si layer without a Cr hardmask. Lastly, a Cr solution (Diammonium Cerium(IV) Nitrate) was used to etch the Cr hardmask. SiNBs with various lateral dimensions and fixed 150-nm height were then fabricated.

doi:10.6342/NTU202300045

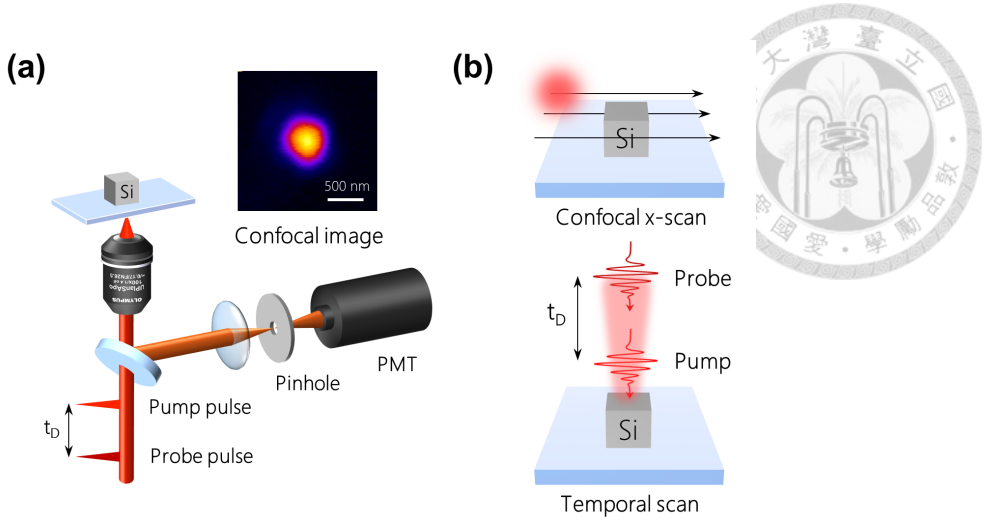

Figure 3.6: Confocal pump-probe microscope with intensity x-scan and pump-probe temporal scan capabilities. (a) Schematic of a confocal pump-probe microscope. PMT: photomultiplier tube. t_D: time delay between pump and probe pulses. The inset displays the scattering image of a single SiNB (w_x = w_y = 200 nm). Scale bars, 500 nm. (b) Schematic of confocal x-scan and pump-probe temporal scan.

3.4 Optical Properties of SiNBs Characterized by Confocal Pump-probe Spectro-microscope

Optical properties of SiNBs are investigated using a confocal pump-probe microscope, which contains the capabilities of intensity x-scan and pump-probe temporal scan (Figure 3.6a and b) [86]. According to the Mie theory, SiNBs exhibit multipole resonances, whose Mie scattering profiles are determined by physical dimensions [34, 70]. As mentioned, the Mie analytical solution is only valid in the case of nanospheres. For the case of nanoblocks, numerical methods are introduced to calculate the size-dependent Mie scattering cross-section under 785-nm laser excitation, based on the COMSOL software. The simulation results and multipole decomposition analysis are presented in Fig. 3.7a. We note that as the fabrication error results in strong deviation in the measure-

doi:10.6342/NTU202300045

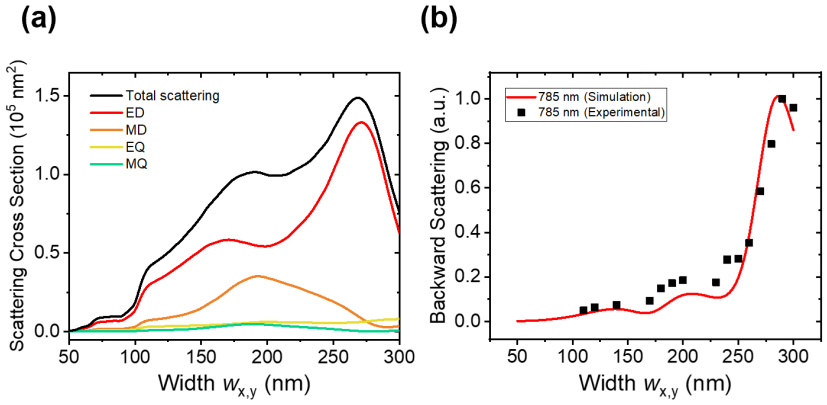

Figure 3.7: Multipole decomposition and size-dependent backward scattering of SiNBs under 785-nm excitation. (a) Simulation of total size-dependent 785-nm scattering. ED: electric dipole, MD: magnetic dipole, EQ: electric quadrupole, MQ: magnetic quadrupole. (b) Simulation and experiment results of 785-nm backward scattering with various dimensions of SiNBs.

ments, we characterize the size-dependent backward scattering with various dimensions of SiNBs (Figure 3.7b, black dot) and also simulate size-dependent tendency (Figure 3.7b, red curve). Experimental and simulation results show good agreement with each other, verifying the dimensions of SiNBs as expected. In this work, $w_x = w_y = 200$ nm and 290-nm SiNBs are chosen to conduct the transient nonlinearity demonstration since these two dimensions allow to induce the magnetic and electric dipole Mie resonances, providing relatively strong backward scattering signals under 785-nm laser illumination.

To characterize the transient nonlinearity, ultrafast carrier dynamics of SiNBs are first carried out in our pump-probe system. Figure 3.8 are the long- and short-term transient scattering $\Delta S/S$ response of a 200-nm SiNB under five pump fluences excitation. At the first few picoseconds, each trace initiates with a drastic decrease to reach its global minimum, contributed by the high carrier densities ($N \approx 10^{20} - 10^{21}$ cm^{-3}), where the estimation is calculated by Eq. 2.1. Then, $\Delta S/S$ quickly recovers via non-radiative carrier

doi:10.6342/NTU202300045

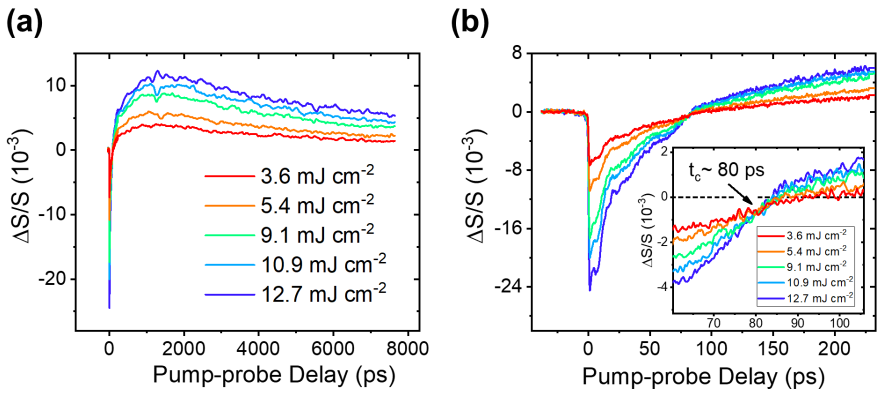

Figure 3.8: Ultrafast carrier dynamics of a 200-nm SiNB. (a) Transient scattering $\Delta S/S$ of a 200-nm SiNB at at 3.6 – 12.7 mJ cm^{-2}. (b) The corresponding data of (a) on a short time scale ($\sim$ 250 ps). The inset highlights the enlarged traces near the crossing point ($t_c \sim 80$ ps).

recombination processes dominated Auger process (Section 2.3), leading to not only carrier density reduction, but also lattice heating due to Auger heating [29, 53]. The former leads to $\Delta S/S$ relaxation towards zero and the latter results in $\Delta S/S$ growth in a positive manner. Together these two contributions give rise to a common crossing point at $t_c \sim 80$ ps for various pump fluences. $\Delta S/S$ increases gradually to reach its maximum at $t_D \sim 1$ ns, resulting from the lattice heating. Then, $\Delta S/S$ starts to relax towards zero after a few nanoseconds due to thermal diffusion to the surroundings.

It is worth recapping the background in Sec. 2.4 and 2.5 that the sign of scattering deviation is determined by not only the carrier dynamics inducing the Mie spectrum shift but also the wavelength of excitation. In the experiment, the 785-nm laser excitation is on the red side of the scattering spectrum (Figure 3.9a). Recap that carrier density provides a negative contribution to the refractive index, leading to spectrum blueshift and scattering deviating negatively. On the contrary, lattice temperature results in the spectrum redshift, and scattering deviates in the negative manner as shown in Fig. 3.9b.

doi:10.6342/NTU202300045

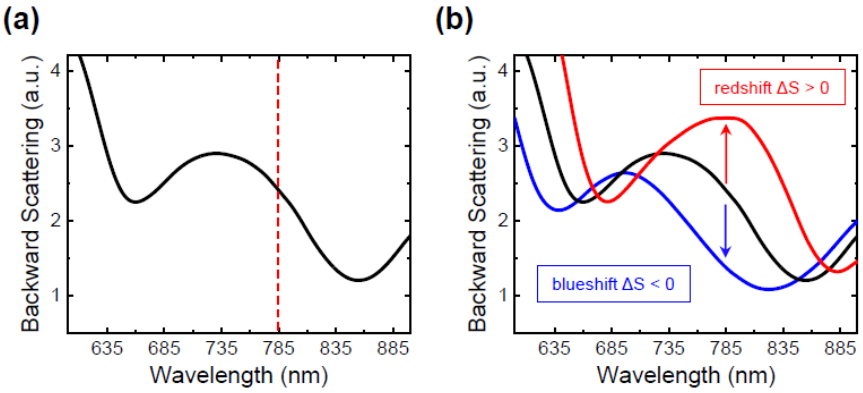

Figure 3.9: Mie scattering spectrum of a 200-nm SiNB. (a) Simulation of a 200-nm SiNB Mie scattering spectrum. The red dot line points out the 785-nm laser excitation. (b) Schematic of Mie spectrum shift due to the refractive index variation, presenting the positive or negative deviation of transient scattering.

Instead of presenting the global fitting of the pump-probe trace in the whole observed window (8 ns), we focus on the analysis in the first 250 ps since, in this time window, we don't have to consider the competition between the lattice heating and thermal diffusion and the simple Auger analytical model can be adopted to describe the carrier dynamics. Both carrier densities reduction via Auger recombination and lattice temperature rise via Auger heating share the same analytic form [29]. Based on the Eq. 2.5, the $\Delta S/S$ traces are analyzed with the following equation:

$$\frac{\Delta S(t)}{S} = A_0 \left(\frac{1}{\sqrt{1 + 2t/\tau_{\text{Auger}}}} \right) + A_1 \left(1 - \frac{1}{\sqrt{1 + 2t/\tau_{\text{Auger}}}} \right) \tag{3.3}$$

where A_0 term corresponds to Auger recombination, and the A_1 term relates to Auger heating. Figure 3.10 reveals the Auger fitting of the pump-probe trace at pump fluence 12.7 mJ cm^{-2}. The red and blue curves represent the contribution of Auger heating and Auger recombination, respectively. Their sum ((purple curve) is well-fitted with the trace, confirming the underlying Auger mechanism. The fitting results (A_0, A_1, and τ_{Auger}) are

doi:10.6342/NTU202300045

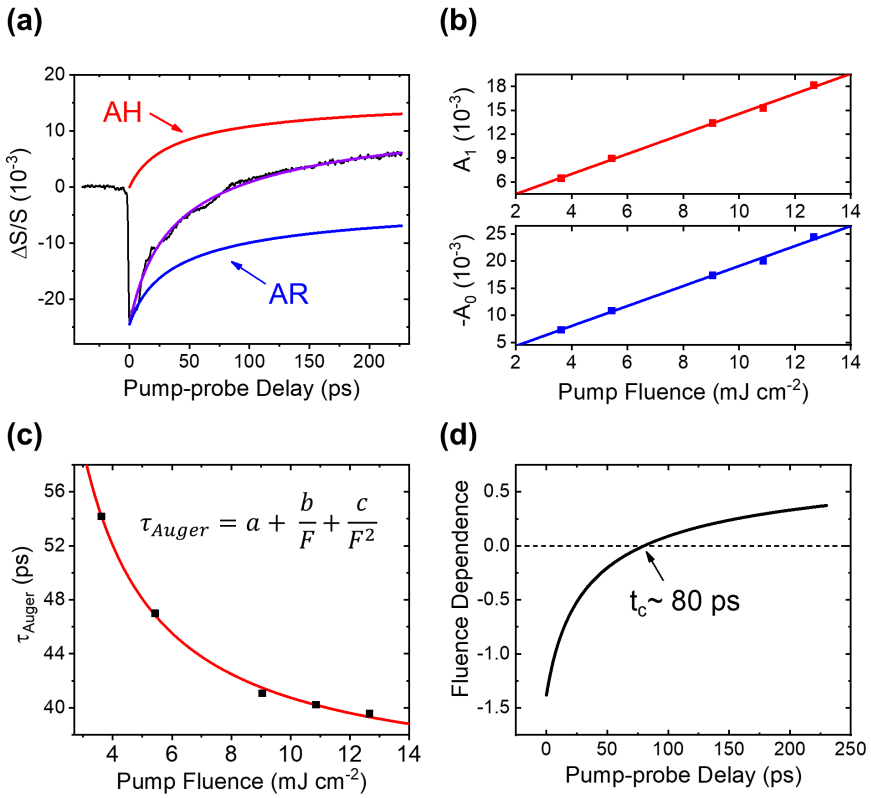

Figure 3.10: Auger fitting of the pump-probe traces of a 200-nm SiNB. (a) Auger fitting of $\Delta S/S$ at pump fluence 12.7 mJ cm^{-2}. The red and blue curves present the components of Auger heating (AH) and Auger recombination (AR) contributions. (b) Fitted amplitudes A_0 and A_1 correspond to AR and AH, respectively. (c) Fitted Auger lifetime τ_{Auger} at five different fluences. (d) Simulated transient scattering fluence dependency $\partial(\Delta S/S)/\partial F$ as a function of t_D, calculated with the fitting results in (b) and (c), manifesting the existence of a common crossing point, whose fluence dependence equals zero.

summarized in Fig. 3.10b and c. Figure 3.10b shows that Auger amplitudes are linearly proportional to the pump fluence, which is governed by photoexcited carrier density N_0 and Fig. 3.10c depicts that Auger lifetime τ_{Auger} reduces with the increment of pump fluence F. As mentioned in Sec. 2.3, in the case of high carrier density ($N_0 \sim 10^{21}$ cm^{-3}), due to the Coulomb screen effects [50], τ_{Auger} will decrease asymptotically to approach the saturation lifetime a. Equation 2.9 fits well with the results. Then, based on the amplitude, Auger lifetime tendency (solid lines in Fig. 3.10b and c) and Eq. 3.3, we can simulate the fluence dependence of transient signals, denoted as $\partial(\Delta S/S)/\partial F$. In Fig. 3.10d, the

doi:10.6342/NTU202300045

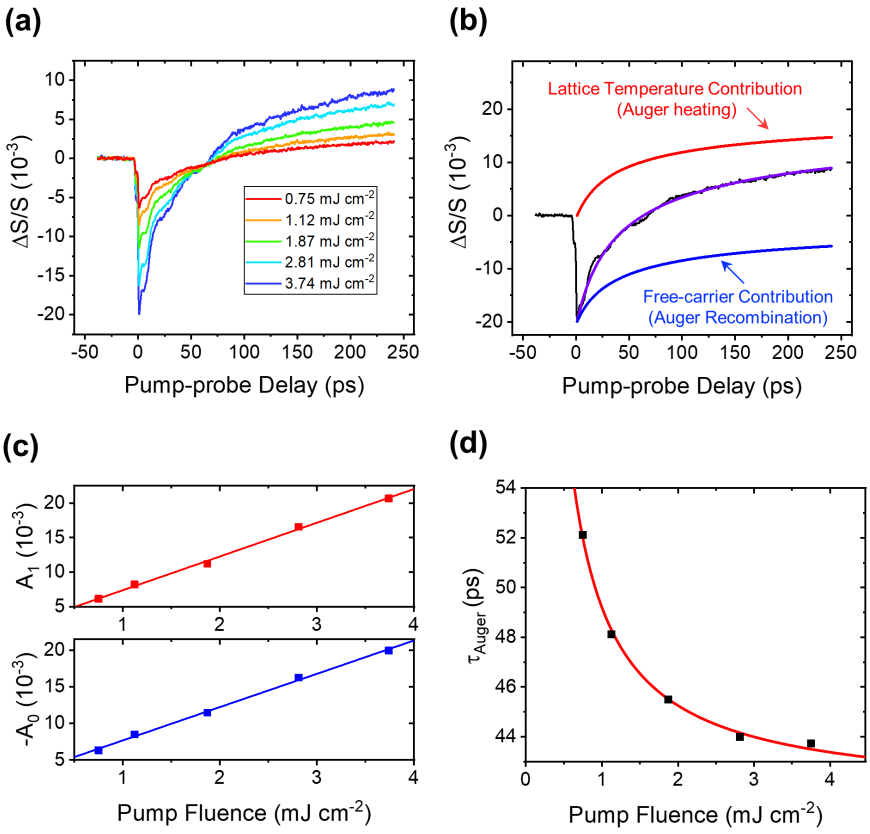

Figure 3.11: Auger fitting of the pump-probe traces of a 290-nm SiNB. (a) Transient scattering $\Delta S/S$ of a 290-nm SiNB at 0.75 – 3.74 mJ cm^{-2}.(b) Auger fitting of $\Delta S/S$ at pump fluence 3.74 mJ cm^{-2}. The red and blue curves present the components of Auger heating and Auger recombination contributions. (c) Fitted amplitudes A_0 and A_1 correspond to AR and AH, respectively. (d) Fitted Auger lifetime τ_{Auger} at various fluences.

zero-value features the common crossing point $t_c \sim 80$ ps, that is, transient scattering is fluence-independent at this special time point.

In brief, the above analyses manifest that ultrafast carrier dynamics in SiNBs is dominated by the Auger process, whose lifetime τ_{Auger} is found to be fluence-dependent. Moreover, mathematically we prove the existence of a common crossing point, featuring a full saturation nonlinearity. The same measurements and analyses are conducted for the 290-nm SiNBs, as shown in Fig. 3.11. In the following section, we characterize the evolution of Auger-induced transient nonlinearities at different time delays t_D.

doi:10.6342/NTU202300045

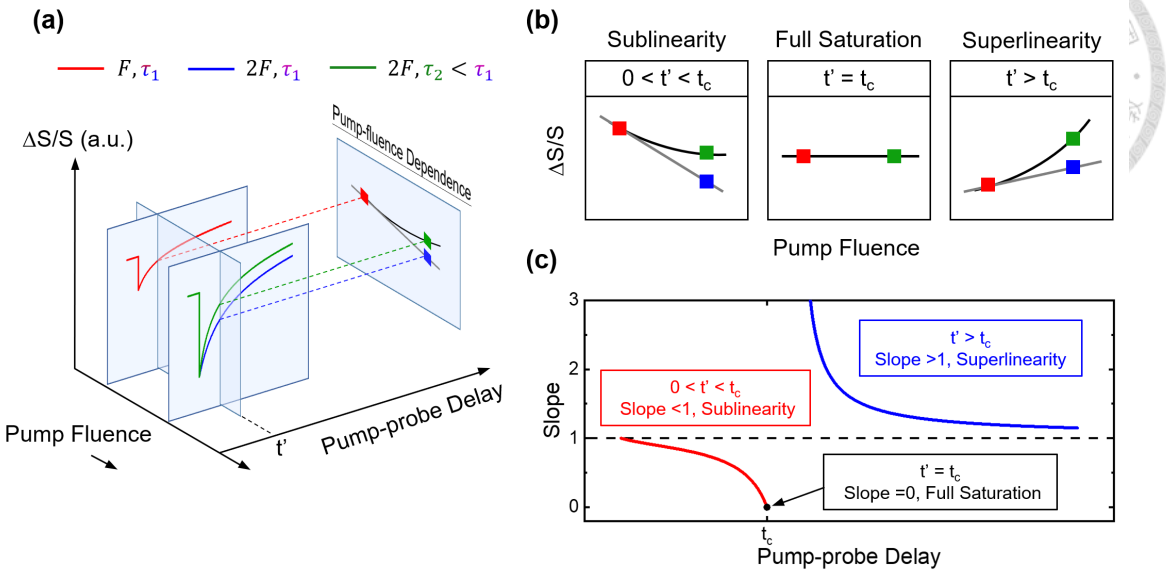

Figure 3.12: Schematic of Auger-induced transient nonlinearity. (a) Schematic of the emergence of transient nonlinearity. The red and green curves are simulated pump-probe traces with the same lifetime τ_1, but different excitation fluences (F and $2F$). The green curve considers Auger effects, resulting in the reduction of a lifetime ($\tau_2 < \tau_1$). By sampling the traces at a specific time delay t', the sectioning $\Delta S/S$ values are projected onto a plane to present the relation between $\Delta S/S$ and pump-fluence, i.e., pump-fluence dependency. (b) Three cases of Auger-induced transient nonlinear behaviors: sub-linearity, full saturation, and super-linearity associated with three temporal intervals. (c) Temporal evolution of Auger-induced transient nonlinearity, which is quantized by the slope of pump-fluence dependence on a logarithmic scale.

3.5 Auger-induced Transient Nonlinearity in SiNBs

Figure 3.12a is a schematic that depicts the appearance of Auger-induced transient nonlinearity through the varied Auger lifetime. If the Auger lifetime is a constant, the projected $\Delta S/S$ onto the "pump-fluence dependence" plane presents the linear behavior, as shown by the red and blue curves. On the contrary, in our experiment, we have to take into account the Auger effects that reduce the lifetime with increasing pump fluence as shown by the green curve. The projection manifests the nonlinear behaviors. Remark-

doi:10.6342/NTU202300045

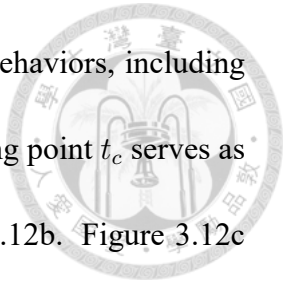

ably, the reduction of the Auger lifetime leads to various nonlinear behaviors, including sub-linearity, full saturation, and super-linearity. The common crossing point t_c serves as a demarcation time point of nonlinear behaviors as shown in Fig. 3.12b. Figure 3.12c presents the temporal evolution of Auger-induced transient nonlinearity. Nonlinear responses are quantized by the slope of pump-fluence dependence on a logarithmic scale. For $0 < t' < t_c$, the slope initiates from unity, and then decreases to zero value, i.e., from linearity to sub-linearity. At $t' = t_c$, the slope equals zero. A full saturation behavior is observed as expected. For $t' > t_c$, the slope is greater than 1 and decays asymptotically to the value of 1, that is, from super-linearity to linearity.

Based on the concept of Fig. 3.12a, we then extract the data points from Fig. 3.8a, sampling at various time delays. In Fig. 3.13a, where t_D is set to be 0 ps, namely, the global minimum in the traces, the $\Delta S/S$ is primarily determined by photoexcited carriers generation with the incident pump pulse. A linear pump-fluence dependence is expected to be observed [87]. At a long time delay ($t_D = 7815$ ps), the thermal diffusion process dominates. As shown in Fig. 3.13b, the observed linear behavior confirms the fact the thermal relaxation time of nanostructures is independent of the pump fluence [88]. To reveal the transition of nonlinear behaviors around the common crossing point ($t_c \sim 80$ ps), pump-probe traces at 75, 80, and 90 ps are specifically sampled, and their pump-fluence dependencies are depicted in Fig. 3.13c – e, respectively. It is obvious that fluence-dependence has a transition from sub-linear (slope < 1), full saturation (slope ~ 0), and then super-linear (slope > 1) behaviors. Figure 3.13f presents the temporal evolution of Auger-induced transient nonlinearity over the whole temporal window. For $t_D = 0$–80

doi:10.6342/NTU202300045

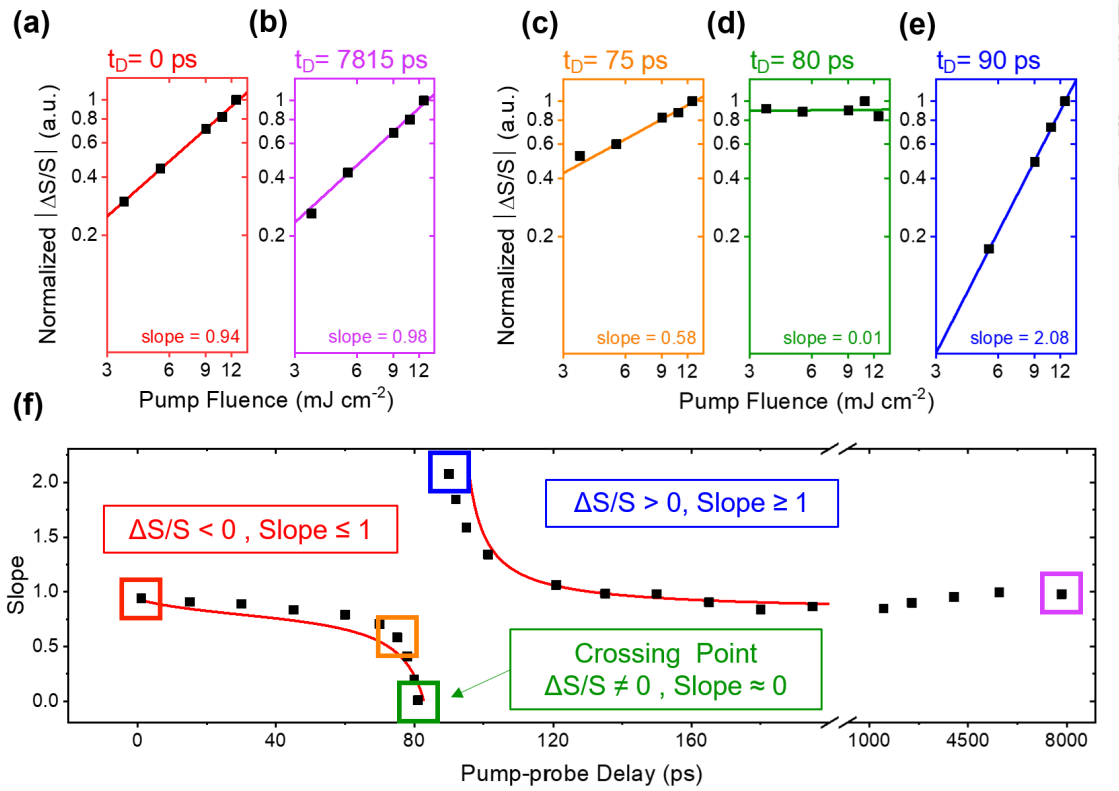

Figure 3.13: Temporal evolution of Auger-induced transient nonlinearity of a 200-nm SiNB. (a) – (e) Normalized $|\Delta S/S|$ as a function of pump fluence on a logarithmic scale for five different time delays t_D: (a) 0 ps, (b) 7815 ps, (c) 75 ps, (d) 80 ps, (e) 90 ps. The fitting slope values are listed in the lower right of each panel. (f) Temporal evolution of Auger-induced transient nonlinearity of a 200-nm SiNB. The colored rectangles are corresponding to (a) – (e). The red curve is calculated through Auger analytic solutions with Eq. 3.3.

ps, presenting the negative $\Delta S/S$, the slopes decline from 0.94 to 0.01. For t_D = 90 – 200 ps, presenting the positive $\Delta S/S$, the slope initiates from 2.08 and decays toward unity, denoting the termination of the Auger nonlinear process. For long-term behaviors (t_D = 1 – 8 ns), no nonlinear carrier dynamics are anticipated, and thus linear pump dependence is presented. The red curve is calculated through analytic solutions with Eq. 3.3, and the great agreement verifies the underlying Auger mechanism. Similar analyses in a 290-nm SiNB are also performed (Figure 3.14). A common crossing point is observed (Fig. 3.14b), but occurs at a shorter time delay ($t_c \sim 64$ ps) as compared with 200-nm one

doi:10.6342/NTU202300045

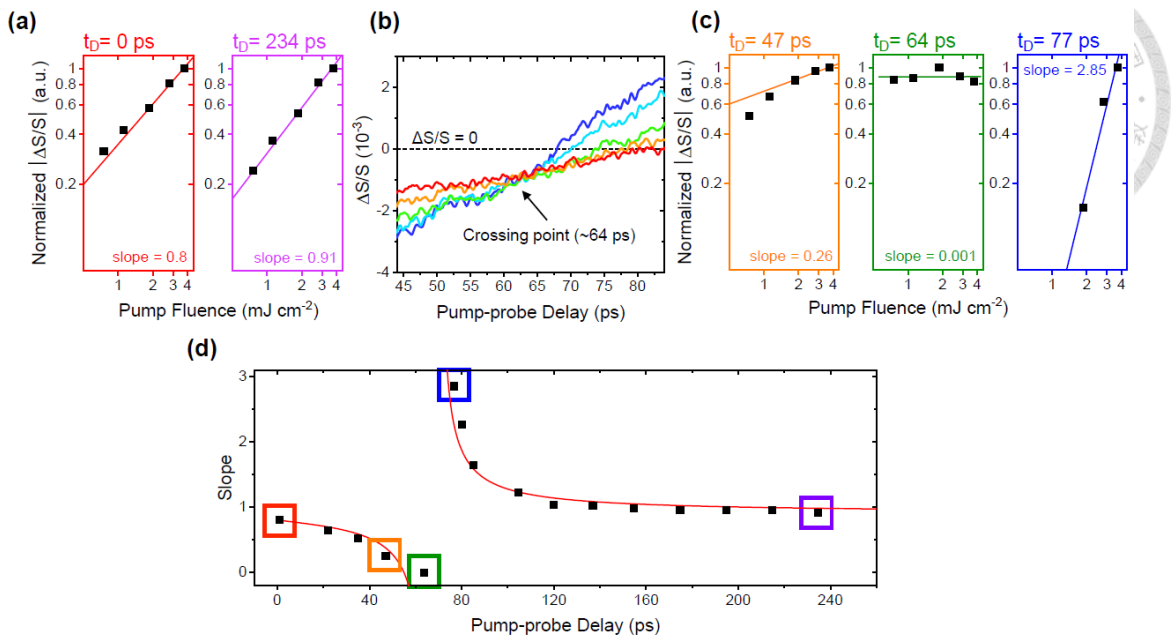

Figure 3.14: Temporal evolution of Auger-induced transient nonlinearity of a 290-nm SiNB. (a)(c) Normalized $|\Delta S/S|$ as a function of pump fluence on a logarithmic scale for five different time delays t_D: 0 ps, 234 ps, 47 ps, 64 ps, 77 ps. The fitting slope values are listed in the lower right of each panel. (b) Enlarged traces near the crossing ($t_c \sim 64$ ps) in Fig. 3.11a. (d) Temporal evolution of Auger-induced transient nonlinearity of a 290-nm SiNB. The colored rectangles are corresponding to (a) and (c). The red curve is calculated through Auger analytic solutions with Eq. 3.3.

($t_c \sim 80$ ps). Nonlinear behaviors transition from sub-linear to super-linear behaviors are presented in Fig. 3.14a and c. The temporal evolution of Auger-induced transient nonlinearity is depicted in Fig. 3.13d. A similar carrier dynamics process has been mentioned in the 200-nm SiNB case.

The simulation in Fig. 3.15 shows that the location of the common crossing point relies on two parameters: saturation lifetime a and the ratio of Auger heating and recombination amplitudes $|A_0/A_1|$. According to Eq. 2.9, the saturation lifetime a is determined by the Auger coefficient, where the related Auger lifetime has been reported to be size-dependent on particle radius ($\tau_{\text{Auger}} \sim R^2$) as the particle size is at a few nanometers scales

doi:10.6342/NTU202300045

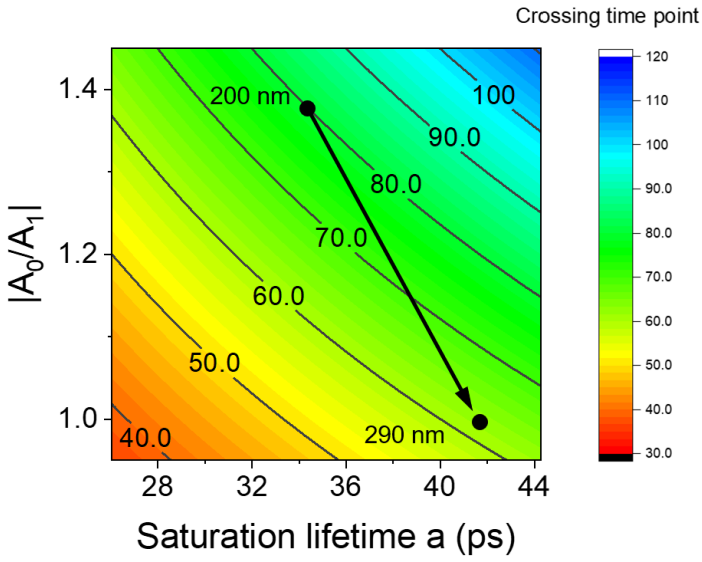

Figure 3.15: Contour mapping of the common crossing point t_c. The location of the common crossing point relies on two parameters: saturation lifetime a in Eq. 2.9 and the ratio of the Auger amplitudes $|A_0/A_1|$.

[89]. However, in our case, the nanostructures with a dimension of hundreds of nanometers, the Auger coefficient seems not to vary too much with the particle diameter. The fact is shown in the saturation lifetimes of the 200-nm and 290-nm SiNBs, which are calculated to be 35 and 42 ps, respectively. Hence, we speculate the distinct factor that changes the position of t_c is the ratio of Auger amplitudes $|A_0/A_1|$. For the amplitude of Auger recombination A_0, it is related to the photoexcited carrier generation, which can be boosted by the Mie resonance. Besides, for the amplitude of Auger heating, A_1 is related to the efficiency of carrier-phonon conversion, which is affected by resonance types. As shown in Fig. 3.7a, an electric dipole and a magnetic dipole perform the contribution of the resonance mode of a 200-nm SiNB. On the contrary, for the 290-nm SiNB, it is dominated by the electric dipole. It has been reported that for a large particle, the heating efficiency depending on electric pole resonance is far higher than a small one with magnetic dipole resonance [90]. Thus, we expect the more considerable A_1 value found in the 290-nm

doi:10.6342/NTU202300045

SiNB. After computing the ratio of Auger amplitudes $|A_0/A_1|$ in Fig. 3.10b and 3.11c, the values are found to be 1.38 and 1, respectively. This leads to a common crossing point occurring at a shorter time delay, as shown in Fig. 3.15. Our findings add a new degree of freedom of temporally manipulating the nonlinear behaviors.

3.6 Application: Transient Nonlinearity for Point-spread-function Engineering

Transient nonlinearities can facilitate numerous applications such as all-optical switching and super-resolution imaging. Here, we exemplify the point-spread-function (PSF) engineering with Auger-induce transient nonlinearity, where the types of anticipated nonlinear behaviors modify the microscopic imaging PSF. The size of PSF shrinks with super-linearity [91] while broadening via sub-linearity. From Fig. 3.13f, as nonlinear behaviors transition from sub-linearity to super-linearity, we expect PSF width to enlarge and then shrink as the time delay increases. The experimental results are presented in Fig. 3.16a – d, showing the pump-probe confocal images and the calculated FWHM values at different nonlinear situations. The tendency of size variation has a good agreement with our expectations. For the linear behaviors (Figure 3.16a and 3.16d), FWHM values are calculated around 260 nm, which supports the concept that there should not be size variation of PSF in the linear state. In contrast, in the nonlinear state, the width of PSF expands to 290 nm (Figure 3.16b) and reduces to 200 nm (Figure 3.16c). This demonstration not only provides the application example but also confirms the underlying nonlinear responses.

doi:10.6342/NTU202300045

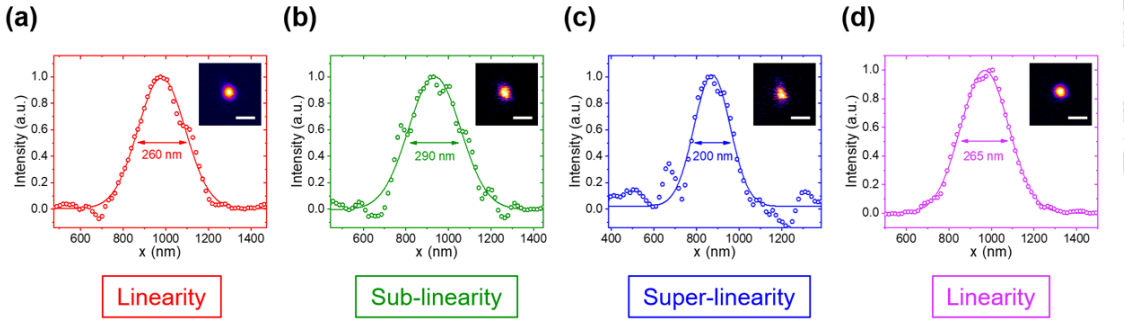

Figure 3.16: Point-spread-function engineering with transient nonlinearity. (a) – (d) cross-sectional line profiles of the pump-probe images of a 200-nm SiNB (inset) at different nonlinear states: (a)(d) linearity, (b) sub-linearity, (c) super-linearity. Scale bars, 500 nm. The corresponding FWHM is calculated through Gaussian fitting and fitting curves are shown in solid lines.

It is worth noting that both sub-linearity and super-linearity can be utilized to reduce the PSF, which has been reported in metal or semiconductor nanoparticles [70, 92].

3.7 Discussion

In brief, we first introduced the general concept of transient nonlinearity generation with fluence-dependent carrier lifetime, based on nonlinear carrier recombination processes, as depicted in Fig. 3.2 and mentioned in Sec. 3.2. As a proof-of-concept experiment, a practical example is the fluence-dependent Auger mechanism of semiconductor nanostructures under high fluence, i.e., high carrier density conditions. Leveraging the combination of intensity x-scan and temporal pump-probe scan, we feature unconventional temporal dynamics of transient nonlinearity in Si nanostructures. Through analyzing the pump-probe traces at various time delays, sub-linear, full saturation, and super-linear behaviors are indeed observed. An unexpected "crossing point" across several re-

doi:10.6342/NTU202300045

laxation curves with different pump intensities is unraveled. The key underlying principle is the fluence-dependent carrier lifetime based on the nonlinear Auger process. Moreover, the presented transient nonlinearities are applied to PSF engineering, demonstrating the potential of sub-diffraction microscopy.

In the temporal window of interest ($0 - 200$ ps), we assume that the dominant recombination process is the Auger mechanism under the high carrier density condition ($N > 10^{19}$ cm^{-3}. However, as the carrier densities gradually decrease, other recombination processes might have to take into account. Here, we verify that in our analyzed temporal window, carrier density still satisfies the high plasma condition and the Auger mechanism remains dominant. According to Eq. 2.1 and Eq. 2.5, the carrier density decaying over 200 ps is calculated to be

$$N(t) = \frac{N_0}{\sqrt{1 + 2CN_0^2 t}} = \frac{10^{21}}{1 + 2\frac{200}{\tau_{\text{Auger}}}} \approx 3.3 \times 10^{20} \ (\text{cm}^{-3}) \tag{3.4}$$

which is still in the high plasma regime. Therefore, within the 200 ps temporal observed window, it is reasonable to claim that Auger recombination is the dominant mechanism in our works.

For the Auger mechanism, it has been widely studied through fluence dependency [59, 93] and photoluminescence decay [89, 94]. Despite this wealth of knowledge, few experimental works have been conducted to characterize the intrinsic nonlinear properties of the Auger process. The reason is that Auger recombination belongs to nonradiative recombination, whose properties determine such as lasing efficiency [95] and the conver-

doi:10.6342/NTU202300045

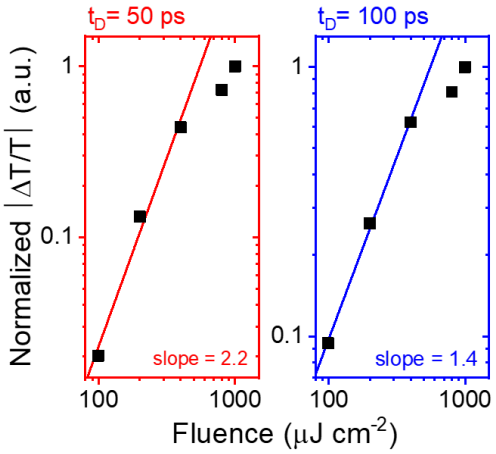

Figure 3.17: Transient nonlinearity of a Si nanowire. Normalized $|\Delta T/T|$ as a function of pump fluence on a logarithmic scale for two different pump-probe delay times t_D: 50 and 100 ps. The data is reanalyzed from Ref. [23] (Figure 4a).

sion rate of solar energy [96]. The essential factor is the Auger lifetime, obtained through analysis of the entire relaxation traces as shown in Fig. 3.10. On the contrary, after analyzing the relaxation traces, we concentrate on interrogating each time point within the traces, revealing the nonlinear pump-fluence dependency (Figure 3.13). After the literature review, we find similar behaviors in Ref. [23]. By re-analyze their pump-probe traces of Si nanowires, transient nonlinearity is also found (Figure 3.17), verifying our concept. Note that the common crossing time point is not observed in Ref. [23], as depicted in Fig. 3.17a. The reason stems from that their excitation fluence is not high enough to induce the saturation of Auger lifetime. This phenomenon is the critical factor to produce the common crossing point.

In Fig. 3.8b and 3.14b, a common crossing point exists in both cases of 200-nm and 290-nm SiNBs and our calculation (Figure 3.15) highlights that crossing points shall emerge in multiple conditions. As long as Auger recombination is the dominant recombination process, the carrier lifetime following the tendency in Eq. 2.9, crossing point is

doi:10.6342/NTU202300045

expected to be observed in various dimensions of nanostructures and different excitation wavelengths. We note that the value of transient scattering at the crossing point does not equal zero, but slightly deviates to the negative side ($\Delta S/S < 0$). Therefore, the signal-to-noise ratio at this time point is too low to be performed in the practical application. We expect more efforts in the future, based on nanostructures morphology or excitation wavelengths to optimize transient nonlinearity magnitudes.

To further generalize our concept, we would like to emphasize that the Auger process is a universal effect on semiconductors, characterized by several methods, including absorption [59], transmission [23], and photoluminescence [93] in various nanostructures such as quantum dots [93] and nanowires [23, 24, 93]. In addition, the carrier density-dependent lifetime has also been reported in amorphous silicon thin film [97]. Therefore, we believe that this demonstration provides the general scenario of transient nonlinearity generation and the presented Auger-based mechanism is generally applicable to other semiconductor nanomaterials, shedding light on temporal tuning nonlinear behaviors and semiconductor super-resolution imaging.

For the application of PSF engineering in Fig. 3.16, super-linearity is utilized to reduce the size of PSF. As shown in Fig. 3.13, the slope increases asymptotically near the crossing point, which enhances the spatial resolution greatly. In addition, sub-linearity is applicable in spatial resolution enhancement via saturation excitation (SAX) microscopy [70, 98]. Full saturation nonlinear behavior occurs at the crossing point, potentially resulting in an unrestricted enhancement based on the combination of pump-probe techniques

doi:10.6342/NTU202300045

and SAX microscopy [99]. Certainly, the signal-to-noise ratio is always a limitation in the measurement. For practical applications, our concept has the potential for defect mapping. Defects in semiconductors are known to present trap-assisted Auger recombination [100] and they may perform different transient nonlinear behaviors as compared with the normal one. In addition, defect-assisted transient nonlinearity can potentially enhance the optical inspection resolution.

In summary, we unravel the novel time-dependent nonlinearity in the fields of Si nanophotonics via the combination of intensity x-scan and temporal pump-probe spectroscopy to provide the spatiotemporal nonlinear information. The general concept is based on the fluence-dependent carrier lifetime and the nonlinear Auger mechanism is taken as a practical example. Nonlinear behaviors transition from sub-linearity to super-linearity over time are observed, manifesting that transient nonlinearity can be temporarily manipulated. The presented transient nonlinearity represent a new type of nonlinear Si nanophotonics, which is valuable in all-optical switching and nanoscale imaging.

doi:10.6342/NTU202300045

Chapter 4

Theory of Coherent Raman Scattering

This chapter provides an overview of the basic concepts of Raman effects, which is described with a classical harmonic oscillator model. Specifically, the theoretical background of coherent anti-Stokes Raman scattering and stimulated Raman scattering is introduced. Moreover, the electronic pre-resonance effect for Raman signals enhancement is described.

4.1 Spontaneous Raman Scattering

The spontaneous Raman scattering was first experimentally observed by C.V. Raman in 1928 [101]. As the light is scattered by the matter, most photons encounter an elastic process (Rayleigh scattering). However, only a small proportion of photons undergo an inelastic process, exchanging the energies with the matter known as spontaneous Raman scattering, as illustrated in Fig. 4.1a. In general, the Raman scattered light contains new frequencies different from the incident light source. Those new components can be clas-

doi:10.6342/NTU202300045

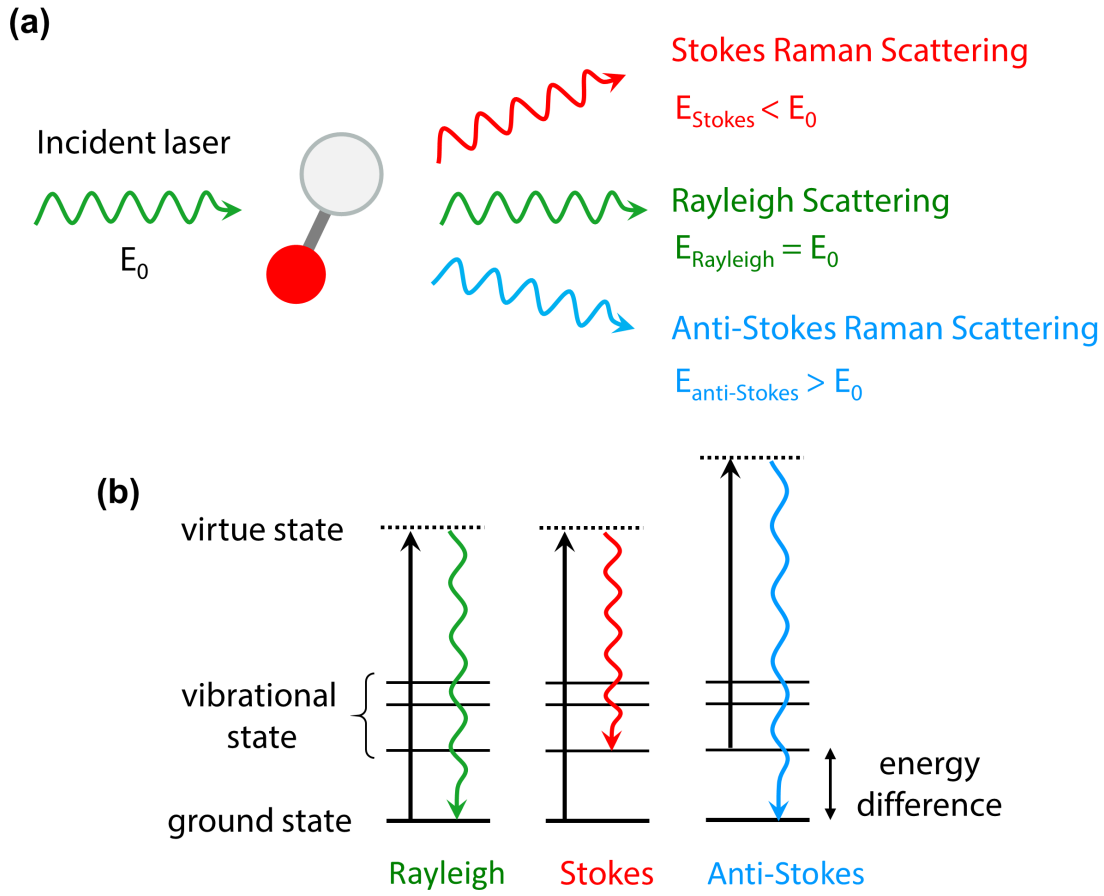

Figure 4.1: Spontaneous Raman scattering. (a) Light scattering by molecules. Three types of scattering: Rayleigh, anti-stokes, and Stokes Raman scattering can be observed in the scattered light spectroscopically. (b) Energy level diagrams describing Rayleigh and Raman scattering. Rayleigh scattering: electrons transition from the ground state and fall back to the ground state. Stokes Raman scattering: electrons transition from the ground state to a vibrational state. Anti-Stokes Raman scattering: electrons transition from a vibrational state to the ground state.

sified into two types: Stokes and anti-Stokes Raman scattering. Stokes components have a redshift, possessing less energy than incident photons. By contrast, anti-Stokes Raman components shift to higher frequencies with more energy than the incident light.

These frequency-shift properties can be understood through the energy level diagram in Fig. 4.1b. The incident light interacts with the molecules to distort the electron clouds and form a virtual state. Stokes scattering is a process that consists of the electrons transi-

doi:10.6342/NTU202300045

Optical Process	Cross-section of	σ (cm^2)
absorption	UV	10^{-18}
absorption	IR	10^{-21}
emission	Fluorescence	10^{-19}
scattering	Rayleigh	10^{-26}
scattering	Raman	10^{-29}

Table 4.1: Comparison between different optical cross-sections for various optical processes. Adapted from Ref. [102].

tion from the ground state to a vibrational state. On the other hand, anti-Stokes scattering starts from a vibrational state and ends up at a ground state. However, spontaneous Raman scattering is an extremely weak process since the Raman cross-section is relatively small, where a typical value is listed in Table 4.1 [102]. Small cross-section issue for the spontaneous Raman process restricts itself to limited sensitivity and high-speed imaging modality in biological applications. This problem is alleviated by the coherent Raman scattering (CRS) process, which is a resonant and coherent nonlinear process that offers an enhanced factor of $10^6 - 10^8$ as compared to the spontaneous Raman process [103], thus opening a new avenue for high-speed label-free spectro-microscopy [37–39].

4.2 Coherent Raman Scattering

Coherent Raman scattering (CRS) is a third-order nonlinear optical effect, which is classified into a four-wave mixing process. That is, the interaction between three input fields in a $\chi^{(3)}$ material leads to the generation of a new fourth field, where the input and output frequencies can be either identical or differentiated [15]. Four fields exchange energies in the $\chi^{(3)}$ materials, reflecting several important chemical information such as

doi:10.6342/NTU202300045

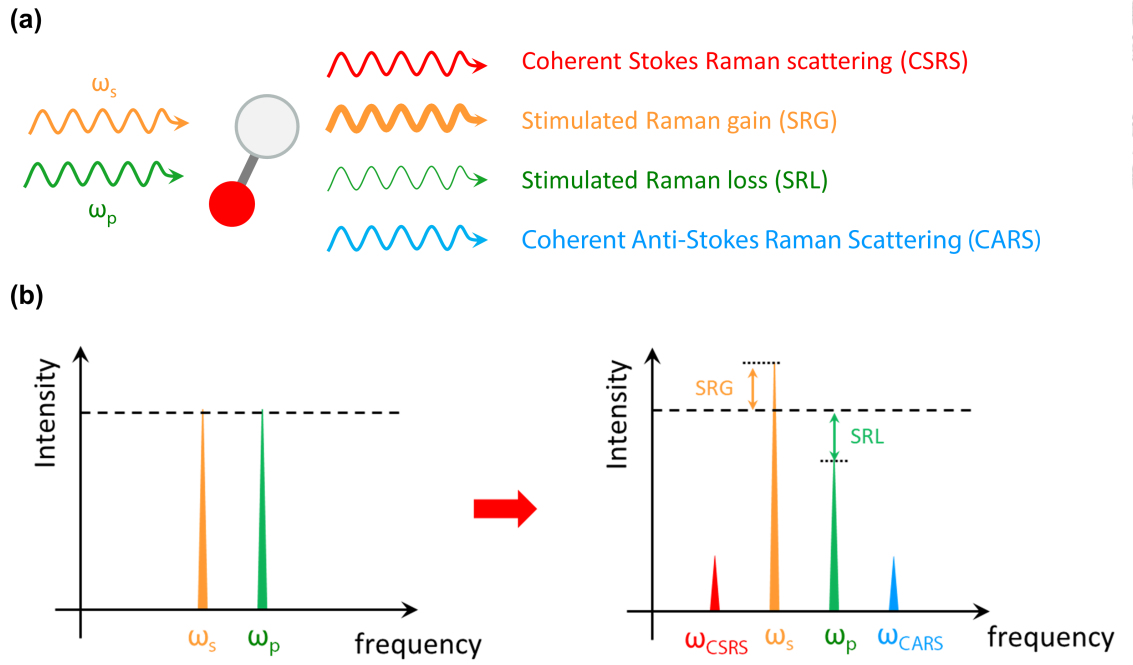

Figure 4.2: Conceptual scheme for the four possible CRS signals generation.

electronic, magnetic, and vibrational features. In the CRS process, two optical fields are applied to materials, where one centering at a frequency ω_p is called pump field and the other with a frequency ω_s is called Stokes fields. Notice that one of the incident fields (pump or Stokes) will also serve as the third field in the four-wave mixing interaction (Fig. 4.2a). Typically, the frequency of the pump is higher than the Stokes ($\omega_p > \omega_s$). When their beating frequency matches the vibration frequency of a Raman mode ($\omega_p - \omega_s = \omega_v$), the presenting electric fields can efficiently drive the Raman vibrational modes coherently, leading to four possible CRS interactions [36]: coherent anti-Stokes Raman scattering (CARS) at frequency $\omega_{CARS} = \omega_p + (\omega_p - \omega_s)$, coherent Stokes Raman scattering (CSRS) at frequency $\omega_{CSRS} = \omega_s - (\omega_p - \omega_s)$, stimulated Raman gain (SRG) at frequency $\omega_s = \omega_p - (\omega_p - \omega_s)$, and stimulated Raman loss (SRL) at frequency $\omega_p = \omega_s + (\omega_p - \omega_s)$ (Fig. 4.2b). The SRG and SRL processes are collectively named as stimulated Raman scattering (SRS).

doi:10.6342/NTU202300045

In the following section, the CRS mechanism with a classical harmonic oscillator model is presented to provide the basic physical interpretation. We will mainly focus on the CARS and SRS processes and will not discuss the CSRS process more since its frequency lies in the infrared region hindered by no ideal photodetector for the measurement, resulting in noisy signals and low signal-to-noise ratio (SNR).

4.3 Classical Theory for Raman Effect

4.3.1 Forced Damped Oscillator Modeling Molecular Vibration

The classical description of Raman effects provides an intuitive picture of the molecular motion driven by external optical fields [8, 15, 36]. In this model, a classical forced damped harmonic oscillator with resonance frequency ω_v and damping coefficient γ is used to describe the molecular vibrational modes when the molecules interact with incoming light fields. For the sake of simplicity, we consider an isolated diatomic molecule, which is suitable for describing the electronic and nuclear motions. As illustrated in Fig. 4.3, $\tilde{q}(t)$ is the induced deviation of the internuclear distance from its equilibrium q_0. The equation of motion for a damped oscillator is then written as

$$\frac{\mathrm{d}^2\tilde{q}(t)}{\mathrm{d}t^2} + 2\gamma\frac{\mathrm{d}\tilde{q}(t)}{\mathrm{d}t} + \omega_v^2\,\tilde{q}(t) = \frac{\tilde{F}(t)}{m_r} \tag{4.1}$$

where $\tilde{F}(t)$ is the time-varying force acting on the molecule originating from the incoming electric fields and m_r represents the reduced nuclear mass. To understand the Raman ef-

doi:10.6342/NTU202300045

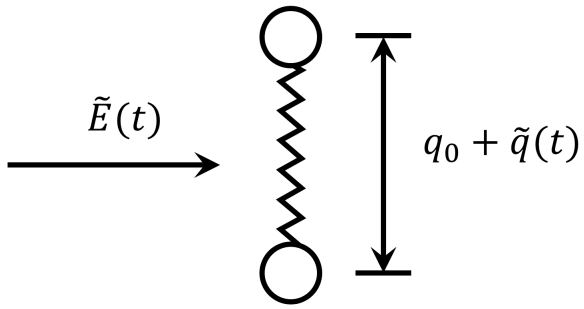

Figure 4.3: Classical view of a diatomic molecule driven by an incoming electric field.

fects in this classical theory, the key concept is that the polarizability α is not a constant, but varies with the internuclear distance $\tilde{q}(t)$. Time-varying polarizability $\alpha(t)$ would induce the variation of dipole moment μ, which acts as a source for generating electromagnetic waves with new frequency components.

4.3.2 Spontaneous Raman Scattering

In the spontaneous Raman scattering process, an optical field $E(z,t)$ is presented on the sample and the linear induced dipole moment $\tilde{\mu}$ located at coordinate z is given by

$$\mu(z,t) = \epsilon_0 \alpha E(z,t) \tag{4.2}$$

For small displacement, polarizability α is expanded in a Taylor series with a first-order approximation:

$$\alpha(t) = \alpha_0 + \left(\frac{\partial \alpha}{\partial q}\right)_0 \tilde{q}(t) \tag{4.3}$$

where α_0 is the polarizability of a molecule at its equilibrium q_0. $\tilde{q}(t)$ is associated with molecular vibrational modes ω_v, which is written as $\tilde{q}(t) = q(\omega_v)\cos(\omega_v t)$, where $q(\omega_v)$ is the amplitude.

doi:10.6342/NTU202300045

In the presence of the optical field $E(z,t) = E_0 \cos(\omega_L t)$, the induced dipole moment is expressed as

$$\begin{aligned}
\mu &= \epsilon_0 \left[\alpha_0 + \left(\frac{\partial \alpha}{\partial q}\right)_0 q(\omega_v)\cos(\omega_v t)\right] E_0 \cos(\omega_L t) \\
&= \epsilon_0 \alpha_0 E_0 \cos(\omega_L t) \\
&+ \frac{\epsilon_0}{2}\left(\frac{\partial \alpha}{\partial q}\right)_0 q(\omega_v) E_0 \left\{\cos\left[(\omega_L - \omega_v)t\right] + \cos\left[(\omega_L + \omega_v)t\right]\right\} \\
&= \mu(\omega_L) + \mu(\omega_L - \omega_v) + \mu(\omega_L + \omega_v)
\end{aligned} \tag{4.4}$$

The first term is related to elastic Rayleigh scattering, where the dipole moment oscillates at the incident frequency ω_L. The second and third terms with frequencies offset by the vibrational frequency ω_v represents the inelastic Raman scattering. New frequency components $\omega_L - \omega_v$ and $\omega_L + \omega_v$ are known as Stokes and anti-Stokes Raman scattering, respectively. Note that the spontaneous Raman signals are proportional to the term $(\partial\alpha/\partial q)_0$, which describes how the applied optical fields drive the vibration mode, leading to the change of polarizability. The polarizability change depends on the symmetry of the nuclear mode, constructing the basis of the selection rule in Raman effects [8, 104].

4.3.3 Coherent Raman Scattering

As mentioned in Sec. 4.3.1, the applied fields will provide the driving force $\tilde{F}$ and induce the dipole moment μ. The energy to construct the dipole moment is given by [15]

$$W = \frac{1}{2}\langle \vec{\mu}(z,t) \cdot \vec{E}(z,t)\rangle = \frac{1}{2}\langle \epsilon_0 \alpha \vec{E}(z,t) \cdot \vec{E}(z,t)\rangle = \frac{1}{2}\epsilon_0 \alpha \langle E^2(z,t)\rangle \tag{4.5}$$

doi:10.6342/NTU202300045

and the associated driving force is a derivative of the energy with respect to spatial coordinates.

$$\tilde{F}(t) = \frac{\partial W}{\partial q} = \frac{\epsilon_0}{2}\left(\frac{\partial \alpha}{\partial q}\right)_0 \langle E^2 \rangle \tag{4.6}$$

In the case of the CRS process, two optical fields (pump/Stokes fields) with amplitude A_p/A_s and frequency ω_p/ω_s are presented in the system. The total illumination field is the sum of the pump and Stokes fields,

$$\tilde{E}(z,t) = A_p e^{i(k_p z - \omega_p t)} + A_s e^{i(k_s z - \omega_s t)} + c.c. \tag{4.7}$$

According to Eq. 4.6, the driving force is thus given as

$$\tilde{F}(t) = \frac{\epsilon_0}{2}\left(\frac{\partial \alpha}{\partial q}\right)_0 \left\{ \begin{array}{l} A_p A_p^* + A_s A_s^* \\ +A_p A_p e^{2i(k_p z - \omega_p t)} + A_s A_s e^{2i(k_s z - \omega_s t)} \\ +2A_p A_s e^{i[(k_p + k_s)z - (\omega_p + \omega_s)t)]} \\ +2A_p A_s^* e^{i[(k_p - k_s)z - (\omega_p - \omega_s)t)]} + c.c. \end{array} \right\} \tag{4.8}$$

Since the frequencies of the applied fields are far from the vibration frequency ω_v (ω_p or $\omega_s \gg \omega_v$), the nuclear modes are not driven efficiently by the incident frequencies. Moreover, when the applied fields contain two frequency components, the vibrational coordinate will experience a time-varying force at their beating frequency $\omega_p - \omega_s$ [8, 15].

doi:10.6342/NTU202300045

Under these conditions, we only need to consider the fourth term in Eq. 4.8, given by

$$\begin{aligned}\tilde{F}(t) &= \epsilon_0 \left(\frac{\partial \alpha}{\partial q}\right)_0 \left[A_p A_s^* e^{i[(k_p-k_s)z-(\omega_p-\omega_s)t)]} + c.c.\right] \\ &= \epsilon_0 \left(\frac{\partial \alpha}{\partial q}\right)_0 \left[A_p A_s^* e^{i(Kz-\Omega t)} + c.c.\right]\end{aligned} \tag{4.9}$$

where we introduce the new notation: $K = k_p - k_s$ and $\Omega = \omega_p - \omega_s$. Time-varying force $\tilde{F}(t)$ and its associated time-dependent displacement $\tilde{q}(t)$ allows energy transfer between the oscillating electronic cloud and nuclear modes, which can be modeled as the solution of an equation for the motion of a forced damped oscillator. Therefore, from Eq. 4.9, we adopt the trial solution as

$$\tilde{q}(t) = q(\Omega)e^{i(Kz-\Omega t)} + c.c. \tag{4.10}$$

Substituting Eq. 4.9 and Eq. 4.10 into Eq. 4.1 yields

$$-\Omega^2 q(\Omega) - 2i\Omega\gamma q(\Omega) + \omega_v^2 q(\Omega) = \frac{\epsilon_0}{m_r}\left(\frac{\partial \alpha}{\partial q}\right)_0 A_p A_s^* \tag{4.11}$$

The corresponding amplitude of the molecular motion is found to be

$$q(\Omega) = \frac{\epsilon_0}{m_r}\left(\frac{\partial \alpha}{\partial q}\right)_0 \frac{A_p A_s^*}{\omega_v^2 - \Omega^2 - 2i\Omega\gamma} \tag{4.12}$$

Equation 4.12 highlights the term $(\partial\alpha/\partial q)_0$ plays an important role in determining the efficiency of the CRS process since it reflects the response of Raman-active material to the incoming fields. In addition, the amplitude is linearly proportional to the incident fields and increases as the beating frequency Ω approaches to the vibration frequency ω_v.

doi:10.6342/NTU202300045

The driving molecular motion in the applied force alters the optical properties of the material, affecting the incoming fields E_p or E_s when propagating through the medium. These phenomena are described via polarization P, which is the sum of the dipole moments

$$\begin{aligned}\tilde{P}(z,t) &= N\mu = N\epsilon_0\alpha\tilde{E}(z,t) \\ &= N\epsilon_0\left[\alpha_0 + \left(\frac{\partial\alpha}{\partial q}\right)_0 \tilde{q}(t)\right]\tilde{E}(z,t) \\ &= N\epsilon_0\alpha_0\tilde{E}(z,t) + N\epsilon_0\left(\frac{\partial\alpha}{\partial q}\right)_0 \tilde{q}(t)\tilde{E}(z,t) \\ &= \tilde{P}_L(z,t) + \tilde{P}_{NL}(z,t)\end{aligned} \tag{4.13}$$

The term proportional to α_0 is related to the linear polarization of the medium. However, The term proportional to $(\partial\alpha/\partial q)_0$ represents the nonlinear polarization associated with the three field interactions: two fields are utilized to drive the molecular motion $\tilde{q}(t)$ and the third field E_p or E_s induce the Raman-dependent nonlinear polarization, including four different frequency components.

$$\begin{aligned}\tilde{P}_{NL}(t) = P(\omega_{CARS})e^{-i(\omega_p+\Omega)t} + P(\omega_{SRG})e^{-i(\omega_p-\Omega)t} \\ + P(\omega_{CSRS})e^{-i(\omega_s-\Omega)t} + P(\omega_{SRL})e^{-i(\omega_s+\Omega)t} + c.c.\end{aligned} \tag{4.14}$$

where $\omega_{CARS} = \omega_p+\Omega = 2\omega_p-\omega_s$ is referred to as coherent anti-Stokes Raman scattering frequency, $\omega_{SRG} = \omega_p - \Omega = \omega_s$ is referred to as Stokes frequency, $\omega_{CSRS} = \omega_p - \Omega = 2\omega_s - \omega_p$ is referred to as coherent Stokes Raman scattering frequency, and $\omega_{SRL} = \omega_p - \Omega = \omega_s$ is referred to as pump frequency. By computing the part of this expression

doi:10.6342/NTU202300045

explicitly, we can derive the complex amplitude of Stokes polarization, given by

$$P(\omega_s) = N\epsilon_0 \left(\frac{\partial \alpha}{\partial q}\right)_0 \left[A_s q^*(\Omega) e^{ik_s z}\right] = \frac{N\epsilon_0^2}{m_r} \left(\frac{\partial \alpha}{\partial q}\right)_0^2 \frac{|A_p|^2 A_s}{\omega_v^2 - \Omega^2 + 2i\Omega\gamma} e^{ik_s z} \tag{4.15}$$

In Eq. 4.15, we introduce the expression of amplitude $q(\Omega)$ from Eq. 4.12. We now define the third-order nonlinear susceptibility for coherent Raman interaction through the expression [15]

$$P(\omega_s) = 6\epsilon_0 \chi_R(\omega_s) |A_p|^2 A_s e^{ik_s z} \tag{4.16}$$

Note that the factor of six comes from the permutation of the interaction field frequency that contributes to the same nonlinear polarization [8]. We thus write down the form of Raman susceptibility

$$\chi_R(\omega_s) = \frac{N\epsilon_0}{6m_r} \left(\frac{\partial \alpha}{\partial q}\right)_0^2 \frac{1}{\omega_v^2 - \Omega^2 + 2i\Omega\gamma} \tag{4.17}$$

At the Raman resonance condition, the Raman susceptibility $\chi_R(\omega_s)$ is approximated as

$$\chi_R(\omega_s) = \frac{N\epsilon_0}{12m_r\omega_v} \left(\frac{\partial \alpha}{\partial q}\right)_0^2 \frac{1}{(\omega_v - \Omega) + i\gamma} \tag{4.18}$$

The real and imaginary parts of the complex Raman susceptibility are calculated to be

$$\begin{aligned} \chi_R'(\omega_s) &= \mathrm{Re}\{\chi_R(\omega_s)\} \propto \frac{\omega_v - \Omega}{(\omega_v - \Omega)^2 + \gamma^2} \\ \chi_R''(\omega_s) &= \mathrm{Im}\{\chi_R(\omega_s)\} \propto \frac{-\gamma}{(\omega_v - \Omega)^2 + \gamma^2} \end{aligned} \tag{4.19}$$

which are illustrated in Fig. 4.4. For the real part, the spectral dependence presents as the

doi:10.6342/NTU202300045

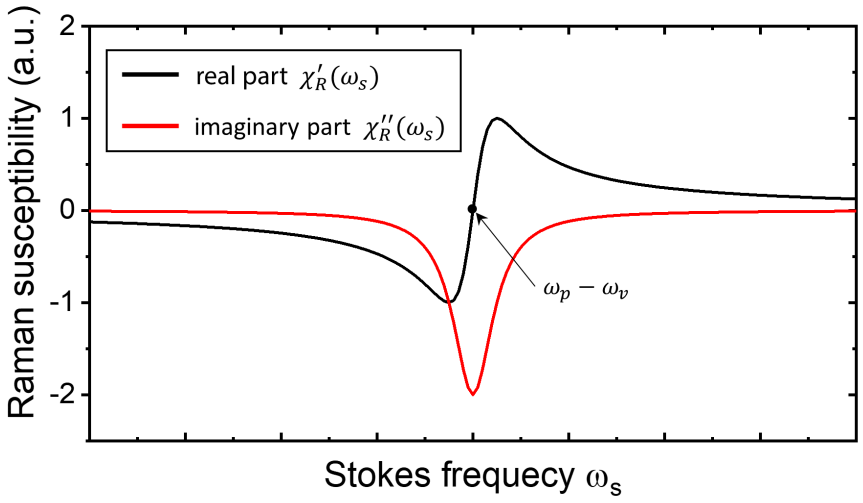

Figure 4.4: Raman susceptibility as a function of the Stokes frequency. $\chi'_R(\omega_s)$ and $\chi''_R(\omega_s)$ are denoted as the real and imaginary part of Raman susceptibility, respectively.

typical resonance shape. On the other hand, the imaginary part shows a dispersive-like shape. Eq. 4.19 shows that at the exact Raman resonance condition $(\omega_v = \omega_p - \omega_s)$, the Raman susceptibility is a purely imaginary number. This links to the gain/loss of SRS signals and the non-resonant background issue, which will be discussed in Sec. 4.3.4.

Different spectral contributions still describe with the same Raman susceptibility equation (Eq. 4.17), taking $\chi_R(\omega_{CARS})$ as an example

$$\begin{aligned}\chi_R(\omega_{CARS}) &= \frac{N\epsilon_0}{6m_r}\left(\frac{\partial\alpha}{\partial q}\right)_0^2 \frac{1}{\omega_v^2 - (\omega_p - 2\omega_p + \omega_s)^2 + 2i(\omega_p - 2\omega_p + \omega_s)\gamma} \\ &= \frac{N\epsilon_0}{6m_r}\left(\frac{\partial\alpha}{\partial q}\right)_0^2 \frac{1}{\omega_v^2 - (\omega_p - \omega_s)^2 - 2i(\omega_p - \omega_s)\gamma} = \chi_R^*(\omega_s)\end{aligned} \tag{4.20}$$

Similarly, We can further derive the nonlinear polarization at other frequencies and summarize them below.

doi:10.6342/NTU202300045

$$
\begin{aligned}
P(\omega_s) &= 6\epsilon_0\chi_R(\omega_s)\left|A_p\right|^2 A_s e^{ik_s z} \\
P(\omega_p) &= 6\epsilon_0\chi_R^*(\omega_s)A_p\left|A_s\right|^2 e^{ik_p z} \\
P(\omega_{CARS}) &= 6\epsilon_0\chi_R^*(\omega_s)A_p^2 A_s^* e^{i(2k_p-k_s)z} \\
P(\omega_{CSRS}) &= 6\epsilon_0\chi_R(\omega_s)A_p^* A_s^2 e^{i(2k_s-k_p)z}
\end{aligned}
\tag{4.21}
$$

Eq. 4.21 presents that the amplitudes of all CRS nonlinear polarization depend on the same magnitude of $\chi_R(\omega_s)$, implying that four CRS signals share comparable signal strength. However, the actual signal intensities are not similar. We will discuss the energy flow in the next section.

4.3.4 Energy Flow in Coherent Raman Scattering

4.3.4.1 Coherent Anti-Stokes Raman scattering (CARS)

To understand the energy flow in the CRS processes, we have to deal with Maxwell's wave equation, which links the induced nonlinear polarization to the generated CRS fields. Then, integrating the field equation with respect to the length of the Raman-active medium, we are able to find out the energy flow among fields (parametric process) as well as the energy exchange between fields and medium (dissipative process).

Starting from Maxwell's wave equation,

$$
\nabla^2\tilde{E}_4 - \frac{n^2}{c^2}\frac{\partial^2}{\partial t^2}\tilde{E}_4 = \frac{1}{\epsilon_0 c^2}\frac{\partial^2}{\partial t^2}\tilde{P}_{NL}^{(3)} \tag{4.22}
$$

doi:10.6342/NTU202300045

where the subscript "4" and superscript "3" denotes the generated fourth fields in a four-wave mixing process originating from a source of third-order nonlinear polarization. We first consider the case of the CARS process, where two pump fields and one Stokes field have interaction to generate the CARS field in the medium. By utilizing Maxwell's wave equation (Eq. 4.22), we can derive the CARS field after propagating the length L in the Raman-active medium, written as [8]

$$\tilde{E}_{CARS}(L) \propto i\{\chi^{(3)}\}^* E_p^2 E_s^* L \text{sinc}\left(\frac{\Delta kL}{2}\right) e^{i\frac{\Delta kL}{2}} \tag{4.23}$$

$\chi^{(3)}$ represents the general third-order nonlinear susceptibility and $\Delta k = k_{CARS} - (2k_p - k_s)$ is the wave vector matching term, relating to the momentum conservation as well as determining the emission direction of the CARS field. Under the assumption of a tight focusing condition, which is the practical situation in microscopy measurement with high numerical-aperture objectives, the phase matching condition relaxes $(\Delta k \neq 0)$ since the propagation length L is extremely small. Therefore, the term ΔkL is set to be zero and the CARS intensity becomes

$$I_{CARS}(L) \propto |\tilde{E}_{CARS}(L)|^2 \propto |\chi^{(3)}|^2 I_p^2 I_s L^2 \tag{4.24}$$

From Eq. 4.24, it is worth noting that first, the CARS intensity has a quadratic dependence on the $\chi^{(3)}$, which is linearly proportional to the number of oscillators ($|\chi^{(3)}|^2 \propto N^2$) as shown in Eq. 4.17. Moreover, $|\chi^{(3)}|^2$ determines the intensity profile in the spectral domain. Second, it has a quadratic dependence on the pump intensity and linear dependence

doi:10.6342/NTU202300045

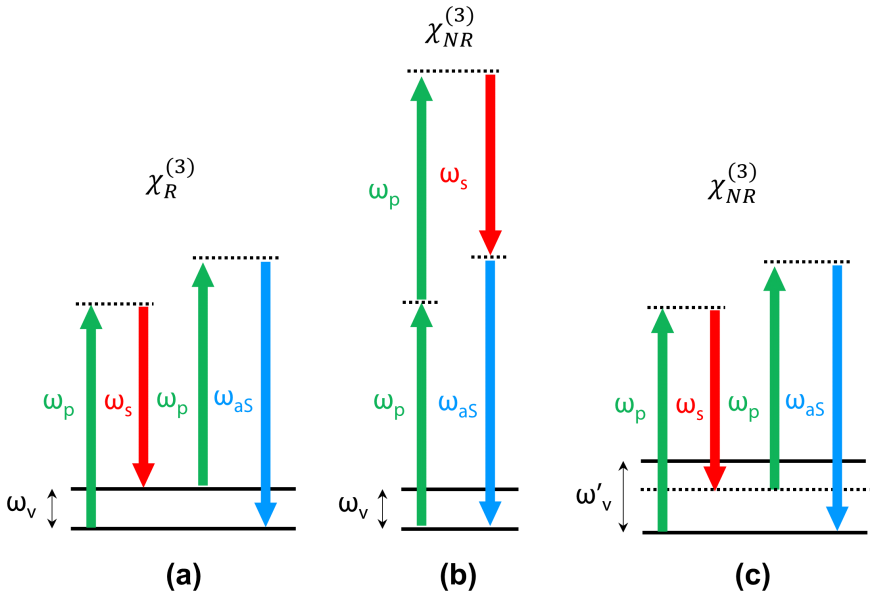

Figure 4.5: Jablonski diagrams of the resonant and non-resonant CARS process. (a) Resonant scheme for the target molecules with vibrational frequency ω_v, leading to $\chi_R^{(3)}$ contribution. (b) Non-resonant scheme for the target molecules due to pure electronic response, resulting in $\chi_{NR}^{(3)}$ contribution. (c) Non-resonant scheme for the non-target molecules with vibrational frequency ω_v' due to pure electronic response, resulting in $\chi_{NR}^{(3)}$ contribution.

on the Stokes intensity. Third, it is quadratically proportional to the length of the Raman interaction region L. In general, $\chi^{(3)}$ is contributed from two terms. One is resonant contribution related to CRS processes $\chi_R^{(3)}$ (Eq. 4.17), reporting the chemical information, and the other is non-resonant contribution $\chi_{NR}^{(3)}$, which is not active with vibrational transitions but dependent on the pure electronic response of the material. Away from electronic resonances, neither real electronic nor vibrational transitions are involved. Thus, $\chi_{NR}^{(3)}$ is a real number and frequency-independent, defined by a real constant.

Figure 4.5 presents the vibrationally resonant and non-resonant transition in the CARS process, leading to the $\chi_R^{(3)}$ and $\chi_{NR}^{(3)}$ contribution, respectively. In general, the overall

doi:10.6342/NTU202300045

third-order nonlinear susceptibility $\chi^{(3)}$ is the summation of $\chi_R^{(3)}$ and $\chi_{NR}^{(3)}$, given by

$$\chi^{(3)} = \chi_R^{(3)} + \chi_{NR}^{(3)} \tag{4.25}$$

The non-resonant contribution $\chi_{NR}^{(3)}$ is typically referred to as the non-resonant background (NRB) in CARS signals. From Eq. 4.24, it states that CARS intensity is quadratically proportional to $|\chi^{(3)}|^2$, recast as

$$I_{CARS} \propto |\chi^{(3)}|^2 = |\chi_R^{(3)} + \chi_{NR}^{(3)}|^2 = |\chi_R^{(3)}|^2 + |\chi_{NR}^{(3)}|^2 + 2\,\mathrm{Re}\left\{\chi_R^{(3)}\right\} \cdot |\chi_{NR}^{(3)}| \tag{4.26}$$

which highlights that the NRB is not simply a constant background. Instead, there is an interference term, coupling resonant with the non-resonant contribution

To find out more about how NRB affects the CARS signals, the spectral profile of individual $|\chi^{(3)}|^2$ components are depicted in Fig. 4.6. Due to the interference term and the pure non-resonant contribution, the theoretical CARS profile displays an asymmetric spectral shape and the presence of the baseline. Compared with the typical Lorentzian shape of Raman resonance (gray line in Fig. 4.6b), the peak of the CARS spectrum has a redshift. The presence of NRB in CARS microscopy results in several limitations [8]:

- image artifacts
- spectral distortion
- no linear correlation between CARS intensity and concentration
- limited sensitivity (weak Raman-resonant signals are buried in the NRB)

doi:10.6342/NTU202300045

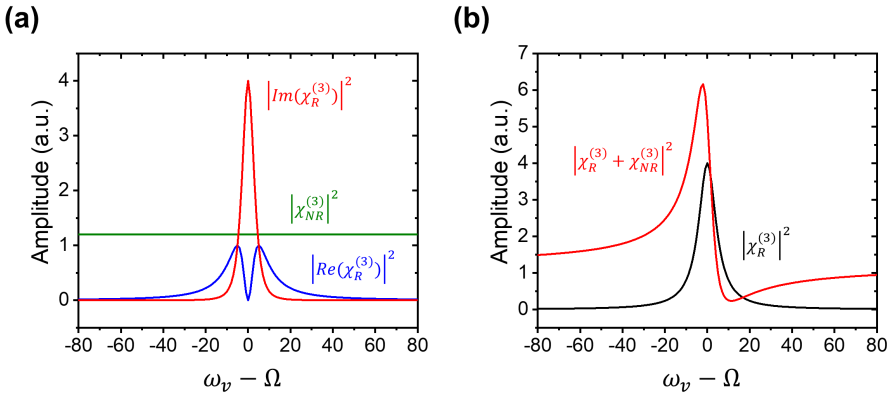

Figure 4.6: Spectral profile of third-order susceptibility. (a) Spectral amplitude of the square of the Raman resonant and non-resonant susceptibility. (b) Theoretical CARS spectrum with consideration of the non-resonant contribution.

thus hampering its development in biomedical research. Fortunately, several methods are developed to suppress the NRB, including epi-detection [105], polarization CARS [106] and time-resolved CARS [107]. Stimulated Raman scattering is known as an inherently background-free method of vibrational contrast, immunity from the NRB. The energy flow of stimulated Raman scattering is introduced in the following.

4.3.4.2 Stimulated Raman scattering (SRS)

Stimulated Raman scattering (SRS) is another class of interactions in the CRS process. With the same concept in Maxwell's wave equation (Eq. 4.22 and 4.23), we can derive the SRS fields after propagating the length L in the Raman-active medium, written as

$$\begin{aligned}\tilde{E}_{SRG}(L) &\propto i\{\chi^{(3)}\}|E_p|^2 E_s L\text{sinc}\left(\frac{\Delta kL}{2}\right)e^{i\frac{\Delta kL}{2}} = i\{\chi^{(3)}\}|E_p|^2 E_s L \\ \tilde{E}_{SRL}(L) &\propto i\{\chi^{(3)}\}^* E_p|E_s|^2 L\text{sinc}\left(\frac{\Delta kL}{2}\right)e^{i\frac{\Delta kL}{2}} = i\{\chi^{(3)}\}^* E_p|E_s|^2 L\end{aligned} \tag{4.27}$$

doi:10.6342/NTU202300045

where the phase-matching condition is automatically satisfied:

$$\Delta k = k_s + k_p - k_p - k_s = 0 \tag{4.28}$$

Given that the generated SRG/SRL field possesses the identical frequency as the incident Stokes/pump field, two fields would interfere in the far field. Therefore, the total intensity at the detector is derived as

$$\begin{aligned} I_{SRG} &\propto |\tilde{E}_s(L) + \tilde{E}_{SRG}(L)|^2 \\ &= I_s - 2A\,\mathrm{Im}\{\chi^{(3)}\} I_p I_s L + B|\chi^{(3)}|^2 I_p^2 I_s L \end{aligned} \tag{4.29}$$

where A and B are introduced to fulfill the equation. The first term is the intensity of the incident Stokes beam, which is assumed not to be attenuated during the nonlinear process. The second term is the interference between the generated SRG field and the incident Stokes field. The last term represents the intrinsic SRG signals, whose power dependency obeys the four-wave mixing mechanism. In practice, the amplitude of the incident Stokes laser field overwhelms the intrinsic SRG amplitude, and thus the third term is typically negligible. To probe the nonlinear process $\chi^{(3)}$, the SRG experiment is then turned into the measurement of the change in intensity of the Stokes beam [8]. This term is typically measured via modulation-transfer geometry, where one of the beams (pump or Stokes) is intensity modulated at high frequency (hundreds of kilohertz to tens of megahertz), and the other beam carries this modulation profile via a nonlinear process. The generated signals are then demodulated with a lock-in amplifier.

doi:10.6342/NTU202300045

Recast the interference term in Eq, 4.29,

$$\begin{aligned}\Delta I_{SRG}(\omega_s) &\propto -2\,\mathrm{Im}\{\chi^{(3)}\} I_p I_s L \\ &\propto -2\,\mathrm{Im}\left\{\chi_R^{(3)} + \chi_{NR}^{(3)}\right\} I_p I_s L \\ &\propto -2\,\mathrm{Im}\left\{\chi_R^{(3)}\right\} I_p I_s L > 0\end{aligned} \tag{4.30}$$

The signals are proportional to the imaginary part of the nonlinear susceptibility and thus the pure real number $\chi_{NR}^{(3)} \in \mathbb{R}$ does not make any contribution. With the same concept of derivation, the SRL signal is written as

$$\Delta I_{SRL}(\omega_p) \propto +2\,\mathrm{Im}\left\{\chi_R^{(3)}\right\} I_p I_s L < 0 \tag{4.31}$$

Note that $\mathrm{Im}\left\{\chi_R^{(3)}\right\}$ is a negative value as shown in Fig. 4.4 and Eq. 4.19. Hence, Eq. 4.30 and 4.31 manifest the gain and loss in the SRS process. Moreover, it is worthwhile to highlight the properties of SRS signals:

- no phase-matching condition constraints ($\Delta k = 0$)
- no presence of NRB ($\chi_{NR}^{(3)} \in \mathbb{R}$)
- linear proportion to the number of oscillators/concentration ($\chi_R^{(3)} \propto N$)
- linear dependence on both pump and Stokes intensities ($\Delta I_{SRS} \propto I_p$ and I_s)
- the SRS spectrum is directly linked to the spontaneous Raman spectra ($\Delta I_{SRS} \propto \mathrm{Im}\left\{\chi_R^{(3)}\right\} \propto \sigma_{Raman}$) [8]

doi:10.6342/NTU202300045

4.3.5 Comparison between CARS and SRS

CARS and SRS techniques rely on the same Raman susceptibility to generate detectable signals and probe the chemical information. The main difference between CARS and SRS is how they exchange energy between the input fields and material, including the dissipative and parametric ways. In fact, there is no difference in probing the chemical information with either method. However, in reality, the choice of detection schemes is determined by several practical factors and how convenient to extract and interpret the collected signals.

The detection scheme of the CARS process is relatively straightforward since CARS signals are spectrally separated from the input pump and Stokes fields and commercial shortpass or bandpass filters help to block the pump and Stokes beam but extract CARS signals. Another advantage is that the one-photon fluorescence background would not contaminate into CARS channel. CARS frequency is blue-shifted from the input fields, while the fluorescence is in the red-shifted region [105]. Still, just like conventional nonlinear microscopy, CARS microscopy provides 3D sectioning capability and allows high-speed imaging [108]. However, as mentioned in Sec. 4.3.4.1, CARS suffers from NRB problems, making signals hard to be interpreted and analyzed. On the contrary, SRS overcomes the major difficulties in CARS microscopy.

First, the SRS signal is free from NRB and the spectra are linearly proportional to the Raman cross-section. Thus, a direct link between SRS and spontaneous Raman spectra

doi:10.6342/NTU202300045

helps molecule recognition and spectra analysis [37]. Second, the SRS signal is linearly dependent on the concentration, which helps in the performance of quantitative chemical analysis with linear algorithm [39, 40]. Third, there is no phase-matching constraint in SRS since the phase-matching term is automatically satisfied (Eq. 4.28). Therefore, no spatial coherence artifacts exist. The resulting images allow conducting image deconvolution with a well-defined point spread function [9]. Forth, for some biological samples, broadband auto-fluorescence would result in a strong background in the CARS channel, while SRS is free from it since SRS is detected as the intensity change of the incident pump or Stokes beams [41]. Although SRS offers several advantages in Raman measurement, there are still some drawbacks. Compared with the CARS setup, SRS measurement is more complicated, which requires a modulation-transfer scheme to extract the interference term [37]. This restricts multiplex or multichannel detection since the implementation of a multichannel demodulation scheme is still demanding [109]. In addition, SRS suffers from various non-Raman backgrounds due to nonlinear transient absorption or nonlinear transient scattering based on the mechanisms such as two-photon absorption (TPA), cross-phase modulation (XPM), and thermal lensing effects (TL) [110, 111]. Fortunately, some methods are developed to suppress the nonlinear background, including stimulated Raman gain and loss detection [110, 112], frequency modulation [113], dual-vibrational excitation [114], and deep learning [115]. Table 4.2 summarizes the comparison between CARS and SRS techniques. From the comparison, it is obvious that SRS provides several outstanding advantages over CARS. Therefore, in this dissertation, we mainly focus on the development of SRS microscopy.

doi:10.6342/NTU202300045

Coherent anti-Stokes Raman scattering	Stimulated Raman scattering
Parametric process	Dissipation process
Presence of NRB	Absence of NRB
Distorted Raman spectrum	Identical spectrum to spontaneous Raman
Quadratic concentration dependence	Linear concentration dependence
Spatial coherence artifact	Absence of spatial coherence
Absence of pump-probe background	Presence of pump-probe background

Table 4.2: Comparison between CARS and SRS processes. Adapted from Ref. [9].

4.4 Electronic Pre-resonance Effect (EPR)

A small cross-section problem is always a big issue for Raman effects. Although CRS offers an enhanced factor of $10^6 - 10^8$, the sensitivity is still relatively low as compared to the fluorescence. This problem stems from a consequence of the "far-off" resonance of the excitation in the Raman process that electronic transitions are not coupled to enhance the cross-section. To overcome this issue, the resonant Raman effects are well-known to boost the Raman transitions by approaching the excitation frequency close enough to the absorption peak of molecules [116–118]. With the similar concept, resonant Raman effects have been also demonstrated in both CARS [119] and SRS [120] spectroscopy. However, in previous reports, when combining electronic resonance with SRS techniques, large nonlinear backgrounds would overwhelm SRS signals, resulting in no vibrational features in the SRS spectrum [44, 120]. This leads to the interest in the pre-resonance region, which seeks the balance between nonlinear background influence and sufficient SRS signal enhancement factor. Lu et al. have reported that the effective electronic pre-resonance (EPR) region lies in the pump frequency detuning from the absorption peak of molecules by $2-6$ times the absorption bandwidth Γ to preserve adequate signal-to-background ratio

doi:10.6342/NTU202300045

($S/B > 5$). The underlying concept is that SRS signals are known to decay much slower than the absorption profile. Therefore, with the strategical detuning range, it is able to enhance the SRS signals while attenuating nonlinear pump-probe background [45].

Theoretically, the behavior of EPR enhancement could be approximated by the Albrecht A-term expression in spontaneous Raman measurement [46, 47, 117], which describes the dependence between the excitation frequency and the Raman cross-sections:

$$\sigma_R(\omega_L) = K\omega_L(\omega_L - \omega_v)^3 \left[\frac{\omega_e^2 + \omega_L^2}{(\omega_e^2 - \omega_L^2)^2}\right]^2 \tag{4.32}$$

where K is the frequency-independent factor, ω_L represents the excitation frequency, ω_v is the vibrational frequency, and ω_e refers to the frequency of the transition to the excited state. We can rewrite the Eq. 4.32 into the SRS version by replacing the excitation frequency ω_L with the pump frequency ω_p [45]:

$$\sigma_R(\omega_p) = K\omega_p(\omega_p - \omega_v)^3 \left[\frac{\omega_e^2 + \omega_p^2}{(\omega_e^2 - \omega_p^2)^2}\right]^2 \tag{4.33}$$

From Eq. 4.33, we note that the growth of Raman cross-sections follows the dependence on the fourth power of the frequency detuning $(\omega_e - \omega_p)$.

Occasionally, the expression in Eq. 4.32 results in the overestimation of the pre-resonance enhancement. This occurs because the A-term approximation is under the assumption that a single electronic transition determines the Raman intensities. In fact, various transitions must provide the contribution that affects the Raman cross-sections. Therefore, the Albrecht A-term expression is phenomenologically modified by adding

doi:10.6342/NTU202300045

a constant K_2 that refers to the contribution of an extremely high energy state with a frequency-independent property [47, 117]. Recast Eq. 4.33 as

$$\sigma_R(\omega_p) = K\omega_p(\omega_p - \omega_v)^3 \left[\frac{\omega_e^2 + \omega_p^2}{(\omega_e^2 - \omega_p^2)^2} + K_2\right]^2 \tag{4.34}$$

This highlights that not all vibrational modes in the molecules possess the EPR enhancement. In a previous report, John et al. have demonstrated that compared $C \equiv N$ and $C - C$ stretching modes in acetonitrile, there is no EPR enhancement in $C - C$ stretching mode since no suitable electronic transition exists to dominate the Raman intensity [47].

To examine the EPR enhancement of a single vibration mode in SRS measurement, the frequencies of both pump and Stokes beams are required to detune accordingly. However, the current benchmark optical parametric oscillator laser systems in SRS spectromicroscopy [37, 44] do not provide the dual-wavelength tunability to conduct the EPR detection, where the wavelength of Stokes beam is usually fixed at 1030 or 1045 nm. Therefore, in this dissertation, we introduce the new scheme broadband supercontinuum: double-pass multiple-plate continuum (DPMPC) to offer multi-wavelength tunability [121], facilitating the EPR detection.

doi:10.6342/NTU202300045

Chapter 5

Double-pass Multiple-plate Continuum (DPMPC) for Coherent Raman Scattering Spectro-microscopy

In this chapter, the performance of the DPMPC-CRS system is examined, including spectroscopic measurement of pure chemical solution and imaging modality for biological samples. Moreover, the dual-wavelength tunability of the DPMPC light source that facilitates the entire Raman-active Region interrogation and electronic pre-resonance detection is demonstrated.

5.1 Introduction

Raman scattering excited by a single laser beam carries the chemical information of species based on the vibrational response of intrinsic chemical bonds, providing chemical contrast. With Raman spectro-microscopy, chemical labeling is not a prerequisite

doi:10.6342/NTU202300045

to provide the chemical information. This allows bio-samples to remain unperturbed for characterization, presenting their nature bio-function. However, spontaneous Raman scattering is extremely weak due to the small cross-section, which is typical on the level of $10^{-29}\,\mathrm{cm}^{-2}$ [102]. The low efficiency results in a long integration time and slow acquisition speed, seriously restricting its application for live bio-imaging.

Compared with spontaneous Raman scattering, signals from coherent Raman scattering (CRS) implemented with two laser beams are enhanced by seven orders of magnitude, thus enabling rapid chemical identification and label-free imaging in biological samples [36, 122, 123]. The two most adopted effects in CRS techniques are coherent anti-Stokes Raman scattering (CARS) and stimulated Raman scattering (SRS), which are typically implemented with two synchronized ultrashort pulses with different frequencies (ω_{pump} and ω_{Stokes}). These two beams are then tightly focused on the sample with superb temporal and spatial overlapping to induce vibrational responses. If the frequency difference matches specific vibrational modes ($\Omega = \omega_{\mathrm{pump}} - \omega_{\mathrm{Stokes}}$), molecular vibration is driven resonantly and coherently, leading to the dramatic amplification of Raman signals.

For the CARS process, the frequency of the generated CARS signals is centered at $\omega_{\mathrm{CARS}} = \omega_{\mathrm{pump}} + \Omega$, which is relatively straightforward to separate from the incident radiation with a filter for the detection. Therefore, CARS spectro-microscopy is on active duty earlier for more than two decades [124]. Nevertheless, it is well-known that CARS suffers from a non-resonant background problem due to four-wave mixing that arouses image artifacts and Raman spectra distortion [9, 105], while SRS is free from this back-

doi:10.6342/NTU202300045

ground artifact (Sec. 4.3.4). Moreover, SRS signals share the identical spectra feature with spontaneous Raman, and scale linearly with excitation intensities and molecular concentration, thus giving merits to quantitative chemical analysis. This is the underlying reason of provides the growing popularity in the development of SRS microscopy over CARS [44, 125–128].

For both CARS and SRS modalities, the main requirement in the laser system is to generate two tightly synchronized pulses with single wavelength tunability, adjusting either pump or Stokes frequencies to match the desired Raman modes. The current benchmark laser system is a combination of picosecond or femtosecond mode-locked lasers and synchronously pumped optical parametric oscillators (OPO) [44, 122]. Commercial mode-locked solid-state lasers such as Ti:Sapphire lasers offer not only a wide frequency tuning range but also a high repetition rate (tens of megahertz), allowing a shot-noise limited detection as well as high-speed imaging up to video rate [9, 114, 123]. Despite the great success, OPO systems have several technical weaknesses. Due to the phase-sensitive issue, OPO systems are difficult to access the low Raman shift region. Moreover, once the OPO frequencies are set to observe the desired Raman shift, there is no freedom to adjust the wavelengths anymore, restricting the highly sensitive electronic pre-resonance (EPR) detection by bringing the pump frequency close to the absorption peak of samples [44, 45].

In parallel, aiming to provide advantages in terms of a small footprint, low cost, and high reliability, fiber laser technology has also been utilized in the CRS laser system based

doi:10.6342/NTU202300045

on several nonlinear mechanisms such as soliton self-frequency shift (SSFS) [129, 130], four-wave mixing (FWM) [131, 132], and supercontinuum (SC) generation [133–135] to achieve frequency-tunable excitation. SSFS generates red-shifted Stokes pulses based on the power transfer from pump pulses and has been demonstrated in multiphoton microscopy [136]. Still, the fixed pump frequency does not support EPR mode as well, and a limited amount of redshift property can only characterize a finite window of Raman shifts ($870 - 1180$ cm^{-1} [129] and $2530 - 3270$ cm^{-1} [130]). FWM is capable to provide a wider Raman observed window ($700 - 3200$ cm^{-1} [131]), while both pump and Stokes frequencies are not independently tunable, but adjustable correspondingly under a photon energy conservation condition. Thus, it does not support EPR detection either. The broadband supercontinuum produced from photonic crystal fibers or highly nonlinear fibers is capable to offer one [132, 134] or two [133] frequency tunability for EPR-CRS microscopy. Nevertheless, its progress is still limited by some technical issues.

First, most fiber-based laser systems rely on ytterbium fibers and erbium-doped fibers as gain mediums, lasing at $1020 - 1060$ nm and $1520 - 1570$ nm, respectively. The generated wavelength (> 1 μm) lying in the NIR region is not compatible with EPR detection since the absorption peak of most endogenous bio-molecules is in the visible or ultraviolet region. It is not possible to bring the pump frequency into the pre-resonance region.

Second, the spectral energy density from fiber laser sources is restricted by the damage threshold of fibers, resulting in typically $1 - 100$ pJ/cm^{-1} [129–135]. Since CRS is a third-order nonlinear process, high average power ($10 - 100$ mW) is usually adapted to

doi:10.6342/NTU202300045

produce sufficient CRS signals. This raises the risk of photothermal damage to the bio-sample [137, 138]. In addition, to prevent photovoltage saturation of the photodetector under high-power illumination, a high biased voltage ($\sim$ 60 V) is necessary to be applied, which may induce the degradation of device performance and higher dark noise.

Here, we demonstrate CRS spectro-microscopy driven by a double-pass multiple-plate continuum (DPMPC) light source that provides intense octave-spanning supercontinuum via nonlinear effects such as optical Kerr effects and self-phase modulation in the multiple quartz plates [121, 139, 140]. Such a light source benefits the CRS system in manifolds: (1) The desired pump and Stokes pulses are directly extracted from DPMPC. Thus, two pulses are synchronized automatically in time. The extra time delay in the order of millimeters produced from different optical elements in pump or Stokes light paths can be easily compensated by a compact design such as a wedge pair. This is technically attractive compared with a commercial OPO system that requires an additional long delay line (tens of centimeters) for delay compensation. (2) Moderate energy spectral density ($\sim$ 1 nJ/cm^{-1}) of DPMPC improves the generation efficiency of CRS signals without inducing nonlinear damage [141]. The applied bias voltage (5V) on a photodetector is adequate to measure the pump or Stokes beam at $\sim$1 mW average power without photovoltage saturation effects. (3) The octave-spanning bandwidth allows to access the entire Raman active region ($0 - 4000$ cm^{-1}), beyond the above-mentioned OPO or fiber laser sources. (4) Dual excitation wavelength tunability of the pump and Stokes beams allows various wavelength combinations for a single Raman mode to examine the electronic pre-resonance effects (EPR).

doi:10.6342/NTU202300045

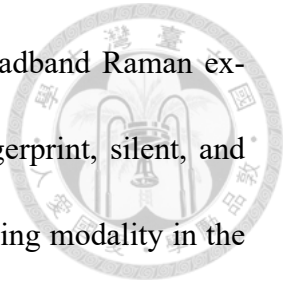

As a proof-of-concept experiment, here we exemplify ultrabroadband Raman examination in a pure chemical solution of acetonitrile across the fingerprint, silent, and C-H stretch Raman regions. Moreover, we demonstrate the bio-imaging modality in the DPMPC-SRS system via the *Drosophila* brain, where the fine structure is clearly visible. Finally, highly sensitive EPR detection is exemplified with the C=C mode of a commercial Alexa 635 fluorescent dye, whose SRS signals increase when approaching the pump frequency to the absorption peak. All of the contents in this chapter have been published in *Optics Express*, 30(21):38975-38984, (2022).

5.2 Dual-wavelength Tunability from DPMPC

The main point of utilizing the DPMPC for the CRS laser system is that such a light source not only simultaneously provides both pump and Stokes beams but also offers dual-wavelength tunability, which can independently adjust the pump and Stokes wavelengths. Based on the mechanisms of the nonlinear Kerr effect and self-phase modulation [139, 140], the incident 1030 nm pulsed laser encounters a spectral broadening process in the quartz plates, resulting in the octave-spanning supercontinuum. In Fig. 5.1, the shaded gray area refers to the Yb:KGW laser spectrum, whose center wavelength is located at 1030 nm. The blue curve is the spectrum of the DPMPC, measured with two spectrometers (HR4000, Ocean optics and BTC264P, B&W Tek), spanning from 600 to 1300 nm. With proper tunable filters [142], both pump and Stokes can be independently adjusted as shown in Fig. 5.2. For the EPR detection, the pump wavelength needs to be

doi:10.6342/NTU202300045

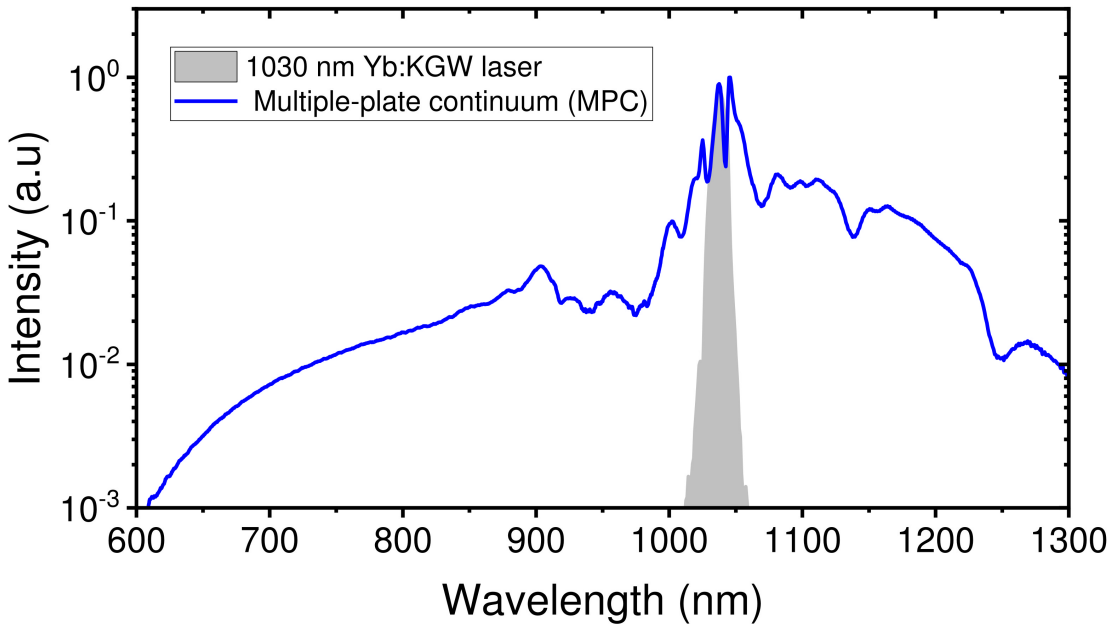

Figure 5.1: Spectrum of the DPMPC. The gray shaded area refers to the spectrum of the front-end Yb:KGW laser operating at wavelengths of 1030 nm.

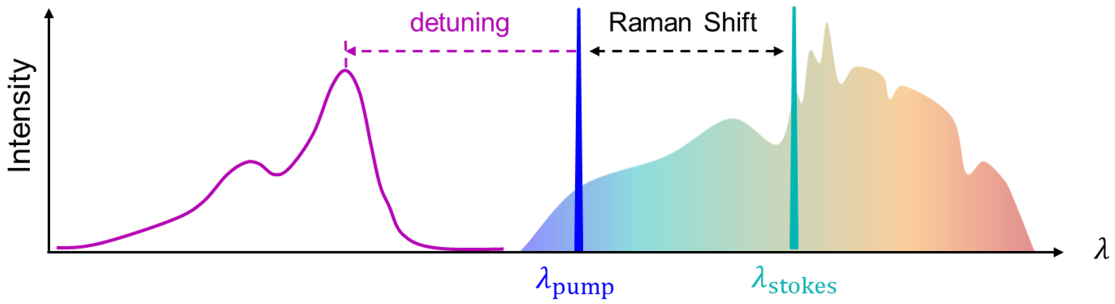

Figure 5.2: Schematic of dual-wavelength tunability of the DPMPC. The colorful area indicates the spectrum of the DPMPC. The purple curve represents the absorption spectrum of a certain sample.

close enough to the absorption peak of the sample, while preserving the desired Raman shift. This makes the DPMPC a fascinating light source in the application of EPR-CRS spectro-microscopy. In the following section, dual-wavelength tunability from DPMPC is utilized in CRS spectro-microscopy, facilitating the spectroscopic characterization in the entire Raman active region, EPR detection, and single-wavelength CRS imaging.

doi:10.6342/NTU202300045

5.3 Experimental Methods

5.3.1 Experimental Setup

Figure 5.3 shows a schematic of the home-built coherent Raman scattering spectro-microscope driven by a DPMPC light source. The front-end laser was a Yb:KGW laser (Carbide, Light Conversion), providing a pulse train at 1030 nm with a 200-kHz repetition rate. The beam was guided into the 1st MPC stage and focused with a concave mirror on the quartz plate. Six 200-μm thick quartz plates are aligned at Brewster's angle to the incident beam for reflection reduction and strategically placed for spectral broadening based on the mechanisms of the nonlinear Kerr effect and self-phase modulation [139, 140]. The pulses were compressed with bounces of chirped mirrors to compensate for the dispersion in the optics. Then, the beam was guided into the 2nd MPC stage for further spectral broadening to octave bandwidth.

To prevent damage to the optics, a 950-nm short-pass filter SPF1 (FES0950, Thor-labs) was used to filter out the most intense part around 1030 nm. The DPMPC su-percontinuum was then split into pump and Stokes paths with a 750-nm dichroic beam splitter DBS1 (#69-183, Edmund). A pair of tunable long- and short-pass filters TCF1 (3G LVLWP and LVSWP, Delta) and a tunable bandpass filter TCF2 (LVFBP, Delta) mounted on linear translation stages were laterally displaced to select the excitation spec-tra of the pump and Stokes pulses, respectively. Thereby we can interrogate the desired Raman shift and obtain SRS spectra via continuous spectral scanning. The intensity of the

doi:10.6342/NTU202300045

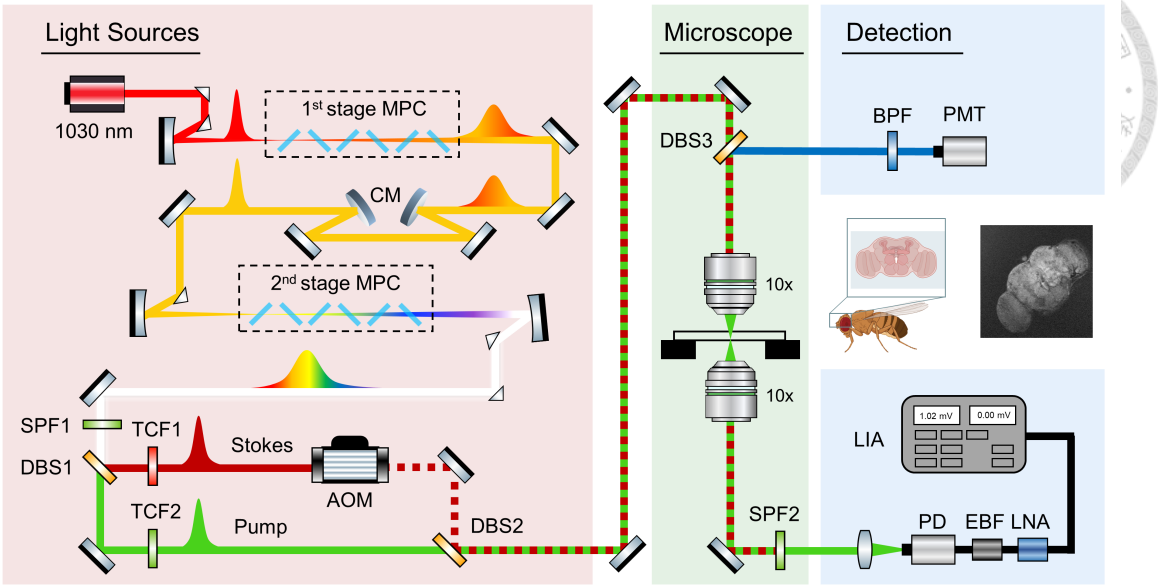

Figure 5.3: Schematic of the DPMPC-CRS setup. MPC: multiple-plate continuum; CM: chirp mirror; SPF#: short-pass filter; DBS#: dichroic beam splitter; TCF#: tunable color filter; AOM: acousto-optic modulator; BPF: bandpass filter; PMT: photomultiplier tube; PD: photodetector; EBF: electronic bandpass filter; LNA: low-noise amplifier; LIA: lock-in amplifier.

Stokes beam was modulated with an acousto-optic modulator (MT110-B50A1.5-IR-HK, AA Opto Electronic) at ∼100 kHz. The first-order diffraction light was used for excitation, whose diffraction efficiency was optimized to be 85%. Pump and Stokes beams were coupled collinearly with another identical 750-nm dichroic beam splitter DBS2.

Subsequently, two beams were directed into a commercial upright microscope (Axio Examiner.Z1, Zeiss) with a raster scan unit (LSM 7MP, Zeiss). A 10x objective (Plan-Apochromat 10x/0.45 M27, Zeiss) was used for optical excitation on samples. The forward pump and Stokes beams were collected in transmission with an identical 10x objective lens, aligned following Köhler illumination. A 750-nm short-pass filter SPF2 (FESH0750, Thorlabs) was placed to filter out the Stokes beam completely, selectively measuring the stimulated Raman loss (SRL) signals with a silicon photodetector (DET100A2,

doi:10.6342/NTU202300045

Thorlabs). The output photocurrent of the photodetector is electronically pre-filtered by a 100-kHz bandpass filter EBF (KR3317-SMA, KR Electronics) to suppress low-frequency noise and pre-amplified with a low-noise amplifier LNA (SA-230F5, NF Corporation) to improve the signal-to-noise ratio (SNR). It was then sent into a lock-in amplifier (SR844, Stanford Research) phase-locked with the Stokes modulation to demodulate the SRL signals. For the epi-CARS signals, they were first reflected with 690-nm dichroic beam splitter DBS3, spectrally filtered out the incident pump and Stokes beams with a bandpass filter BPF (BP 565-610, Zeiss), and then measured by the photomultiplier tube.

For all spectroscopic measurements, the lock-in time constant was set to 100 ms. For imaging, 512 by 512 pixels were obtained for one frame with the maximum pixel dwell time ($\sim$180 μs) of the commercial microscope and 100 μs for the lock-in time constant.

5.3.2 Sample Preparation

***Drosophila* brain preparation**: *Drosophila melanogaster* adult flies were anesthetized with ice baths for two hours before dissection. A pair of forceps (Dumont #55, Fine Science Tools) was used to remove the head cuticle and transfer the dissected fly brains to phosphate-buffered saline (PBS, Thermo Fisher Scientific). Fly brains were then sealed in two coverslips with two 80-μm ring spacers in between before conducting CRS imaging.

doi:10.6342/NTU202300045

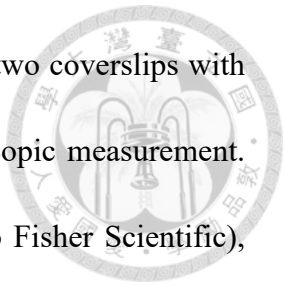

Chemical solution preparation: Pure acetonitrile is sealed in two coverslips with two 80-μm ring spacers in between before conducting the spectroscopic measurement. For Alexa 635 (Streptavidin, Alexa Fluor™ 635 conjugate, Thermo Fisher Scientific), its powder (Streptavidin, Alexa Fluor™ 635 conjugate, Thermo Fisher Scientific) is dissolved with phosphate-buffered saline (PBS, Thermo Fisher Scientific). We take 1 mg powder and dissolve it in 1 ml of PBS. The solution is then sealed in two coverslips before electronic pre-resonance measurement.

5.4 Entire Raman-active Region Interrogation

Leveraging the intense pump and Stokes pulses from octave-spanning DPMPC spectrum with independently tunable frequencies, theoretically, the DPMPC-CRS system can probe the highest wavenumber up to $\sim 9000\,\mathrm{cm}^{-1}$ with 600 nm as a pump wavelength and 1300 nm as a Stoke wavelength. In practice, our system is readily applicable for entire Raman-active region interrogation ($0 - 4000\,\mathrm{cm}^{-1}$). Here, to demonstrate the broadband Raman spectrum interrogation, we investigate the SRS spectrum of pure acetonitrile solution, which exhibits characteristic Raman peak in the fingerprint ($< 1700\,\mathrm{cm}^{-1}$), cell-silent ($1700 - 2700\,\mathrm{cm}^{-1}$), and C-H stretching Raman ($> 2700\,\mathrm{cm}^{-1}$) regions. The measured SRS spectrum is shown in the lower panel of Fig. 5.4a, targeting the intrinsic chemical bonds, including C−C ($920\,\mathrm{cm}^{-1}$), C≡N ($2250\,\mathrm{cm}^{-1}$), and C−H ($2900\,\mathrm{cm}^{-1}$) and agrees well with the spontaneous Raman spectrum (top panel, Figure 5.4a) [143]. Furthermore, to confirm the integrity of the measured SRS results, we conduct the power depen-

doi:10.6342/NTU202300045

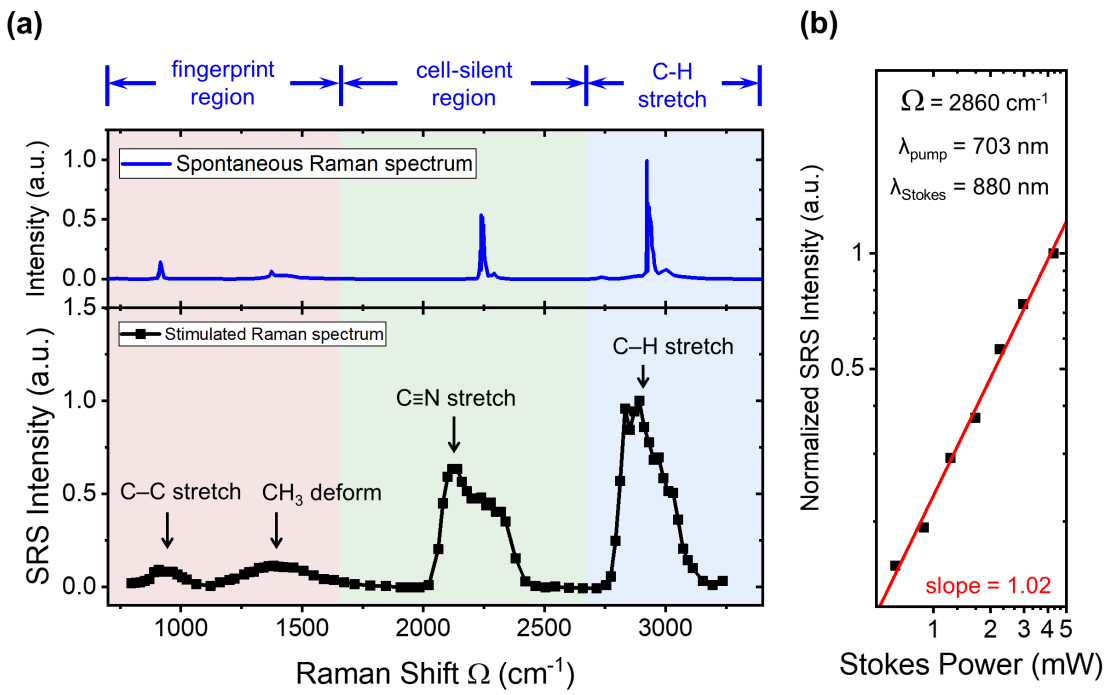

Figure 5.4: Performance of DPMPC-SRS spectroscopy. (a) (top) Spontaneous Raman spectrum and (bottom) SRS spectrum of acetonitrile. (b) SRS signals at 2860 cm^{-1} as a function of the Stokes power, where the slope ≈ 1 indicates the linear power dependence. Each data point was acquired in 20 s under the 1 mW pump power and 3.6 mW modulated Stokes power excitation.

dence experiment, where the SRS signals scale linearly on the Stokes power and linearity is quantized via the slope of power dependence on a logarithmic scale (Fig. 5.4b). Compared the spontaneous and stimulated Raman spectra, the relative coarse spectral resolution ($> 200\,\mathrm{cm}^{-1}$) results from the pass bandwidth of the tunable filter (~ 5 nm bandwidth for the pump beam and ~ 15 nm bandwidth for the Stokes). Poor spectral resolution can be improved via super-narrow bandpass filters, etalon [144], spectral focusing [138, 145], or angularly dispersive devices.

doi:10.6342/NTU202300045

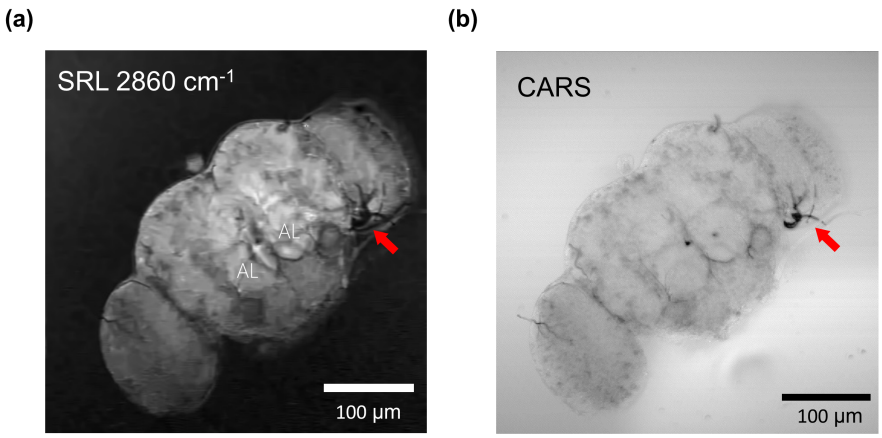

Figure 5.5: CRS images of *Drosophila* brain. AL: antennal lobe. Pixel dwell time: 177.32 μs. Laser powers after the objective are 1.2 mW and 2.6 mW for the pump and Stokes beam, respectively.

5.5 Coherent Raman Scattering Microscopy for Bio-imaging

Next, we conduct the CRS bio-imaging for *Drosophila* brain samples. The wavelengths of the pump and Stokes were set to 703 and 880 nm in order to fit the CH_2 stretching mode of lipids in brain tissue at $2860\,\mathrm{cm}^{-1}$ Raman shift, which allows observing the *Drosophila* brain structure without chemical pretreatment and labeling. Figure 5.5a and 5.5b shows the SRS and CARS image of *Drosophila* brain immersed in PBS solution after 40 times image average, respectively. Compared with SRS and CARS images, CARS images suffer from a large non-resonant background in PBS solution. In an anterior view, two antennal lobes (AL) and trachea structure (dark region indicated by a red arrow) are observed. Neither thermal nor nonlinear tissue damage occurs in the long-term measurement. The total average power on the brain tissue was lower than the reported thermal damage threshold [146] by two orders of magnitude.

doi:10.6342/NTU202300045

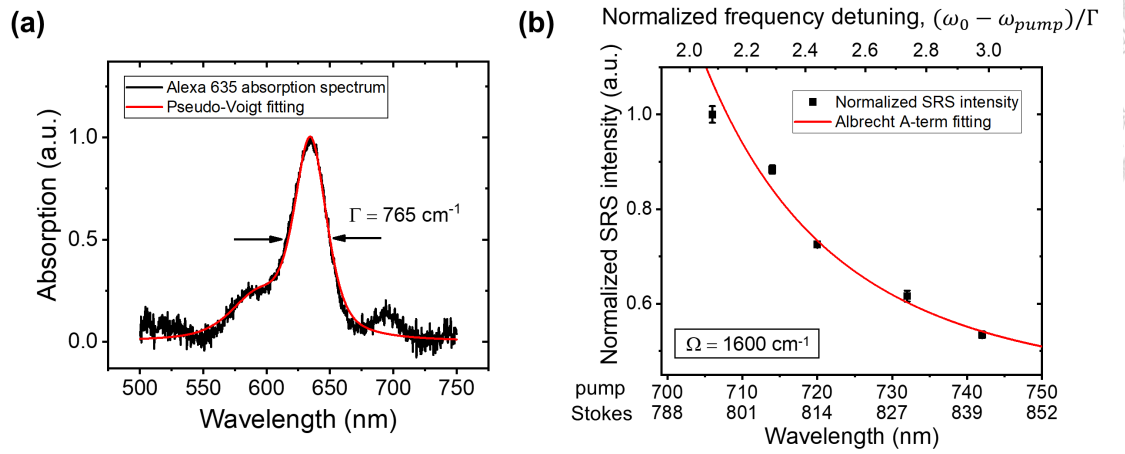

Figure 5.6: EPR detection of Alexa 635. (a) Absorption spectrum of Alexa 635. The red curve refers to pseudo-Voigt fitting, determining the absorption bandwidth as $\Gamma = 765\,\mathrm{cm}^{-1}$. (b) Normalized SRS intensity of C = C vibration mode at $1600\,\mathrm{cm}^{-1}$ Raman shift under different pump-to-absorption detuning conditions within the EPR regime. The red curve represents the Albert A-term fitting.

5.6 Spectroscopic Measurement in the EPR Mode

At last, we demonstrate the EPR detection of commercial dye: Alexa 635. EPR effect has been reported to boost the Raman cross-section by utilizing the electronic coupling to enhance the electron transition, thus leading to highly sensitive Raman detection (Sec. 4.4). In practice, under the criteria of S/B > 5, the pre-resonance excitation region for the pump frequency is established to be detuned from the absorption maximum of the sample by $2-6$ times the absorption bandwidth Γ [45].

In our demonstration, we interrogated the C=C vibration mode of the commercial fluorescent dye: Alexa 635. To determine the absorption peak and spectral bandwidth, the absorption spectrum of Alexa 635 was measured with a halogen lamp (Figure 5.6a), which was then analyzed with pseudo-Voigt function to characterize the absorption peak as

doi:10.6342/NTU202300045

$\lambda_{\text{peak}} = 635\,\text{nm}$ and the spectral bandwidth as $\Gamma = 765\,\text{cm}^{-1}$. The pump wavelength was tuned from 706 nm and 742 nm, and the Stokes wavelength was adjusted accordingly to match the C=C vibration mode at $1600\,\text{cm}^{-1}$ Raman shift. In these conditions, the pump-to-absorption detuning range is calculated to be $2 - 3\Gamma$ within the EPR regime. Figure 5.6b displays the normalized SRS intensities under five different pump/Stokes frequency combinations. The SRS signals increase as decreasing the wavelength detuning. The red curve refers to Albrecht A-term fitting (Eq. 4.33), which is well-fitted with data points, manifesting the EPR effect.

5.7 Discussion

In brief, we demonstrated the CRS spectro-microscopy and highly sensitive EPR detection using a DPMPC supercontinuum light source. Multiple quartz plates are used to conduct a spectral broadening process based on the nonlinear optical Kerr effect and self-phase modulation. The resulting supercontinuum spectrum spans from 600 nm to 1300 nm with high spectral energy density ($\sim 1\,\text{nJ}/\text{cm}^{-1}$). Leveraging the tunable color filters implemented in both pump and Stokes beam paths, two excitation frequencies can be adjusted independently to achieve SRS spectrum scanning across the entire Raman-active region ($0 - 4000\,\text{cm}^{-1}$). In our proof-of-concept experiments, four characteristic peaks of pure acetonitrile solution located in fingerprint, cell-silent, and C-H stretching Raman regions are successfully observed. Moreover, we presented CRS bio-imaging of a *Drosophila* brain immersed in PBS. The fine structure of brain tissue is clearly observed.

doi:10.6342/NTU202300045

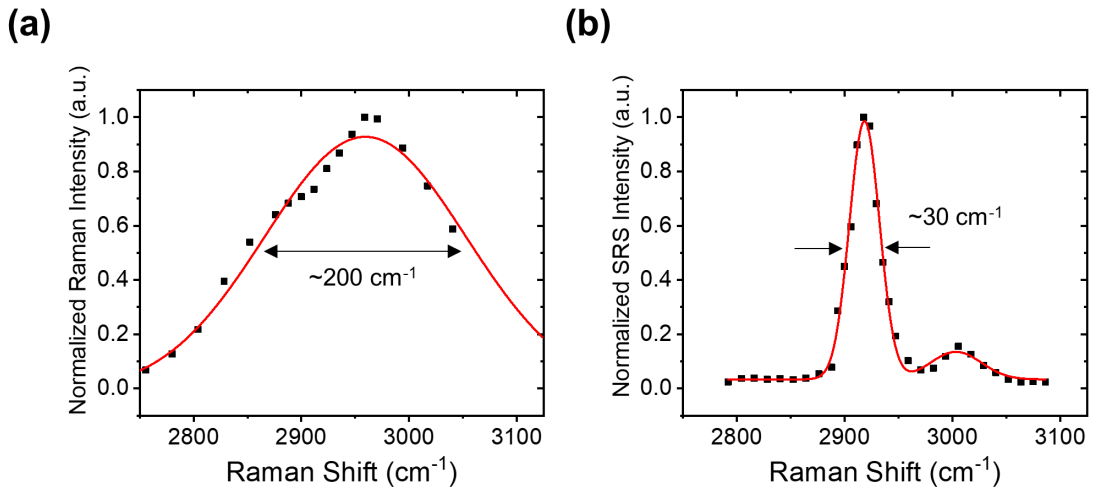

Figure 5.7: SRS spectrum of dimethyl sulfoxide. (a) The results were measured with tunable filters. (b) The results were measured when employing two etalons. (Data from Po-Yi Lee and Cheng-Wei Li)

Finally, benefiting from the dual-wavelength tunability of DPMPC, we confirmed the EPR effect with commercial fluorescent dye: Alexa 635, where the SRS signals increase as the pump-to-absorption detuning decreases.

Several technical improvements are within reach. In the DPMPC-SRS spectroscopic measurement, the spectral resolution in our current setup is estimated to be greater than $200\,\mathrm{cm}^{-1}$, which is determined by the pass bandwidth of the tunable filters. To approach the typical Raman linewidths ($\sim 10\,\mathrm{cm}^{-1}$) [44, 123] in the femtosecond laser system, one can narrow down the excitation bandwidth via an ultra-steep optical filter [114] and an etalon [144]. As a preliminary test, we adopted a customized etalon (OP-13393, Light-machinery) in both pump and Stokes beam paths. By tilting the etalon orientation, the Stokes frequency can be continuously adjusted. High spectral resolution SRS spectrum was demonstrated with the pure dimethyl sulfoxide (DMSO) solution, investigating its characteristic peak ($2919\,\mathrm{cm}^{-1}$ and $3000\,\mathrm{cm}^{-1}$) in the C-H stretching region. In Fig. 5.7a,

doi:10.6342/NTU202300045

the SRS spectrum of DMSO was measured with tunable filters, resulting in the spectral bandwidth of $\sim 200\,\mathrm{cm}^{-1}$. Two prominent peaks can not be well-distinguished and the position of the Raman peak has a redshift. This may come from that for the broad bandwidth excitation, it is hard to define the center wavelength of the excitation, resulting in the misdetermination of the Raman shift. On the contrary, by employing two etalons to narrow the excitation bandwidth, two characteristic peaks can be clearly identified and the position of the Raman peak agrees well with the spontaneous Raman spectrum from the online database: https://spectrabase.com/spectrum/AKJBySxbbP2. Other methods such as spectral focusing [138, 147] and pulse shaping [148] could also be applied to enhance the spectral resolution at the cost of complexity.

For the imaging modality in the DPMPC-CRS system, the image quality and acquisition speed are limited by the laser repetition rate (200 kHz) and AOM modulation frequency ($\sim 100\,\mathrm{kHz}$ in the current setup). To enhance the image quality, we average 40 frames as shown in Fig. 5.5. Figure 5.8a shows the SRS images of *Drosophila* brain after averaging N frames. The corresponding signal-to-noise ratio (SNR) displays in Fig. 5.8b, defined by $(I_{signal} - I_{background})/\sigma_{background}$, where $\sigma_{background}$ is the standard deviation of the background signals. SNR increases with the square root of average frames, following the statistical model. We then envision that through upgrading the repetition rate of a front-end source, SNR and imaging speed can be further enhanced by, for example, adopting high-power thin-disk lasers with the MPC module at $\sim 10\,\mathrm{MHz}$ [149]. We believe the performance of the DPMPC-CRS system would be comparable to that of the OPO-CRS system.

doi:10.6342/NTU202300045

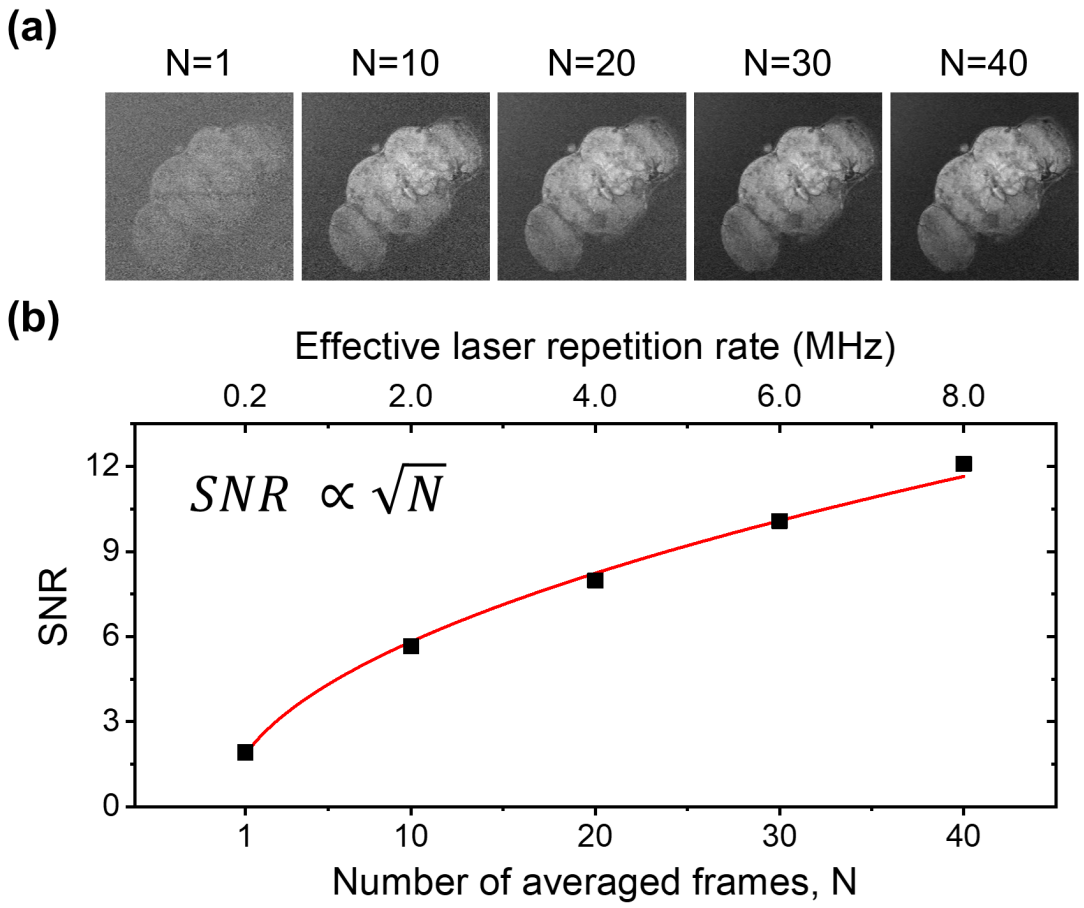

Figure 5.8: SRS images of *Drosophila* brain. (a) Images obtained after averaging 1, 10, 20, 30, and 40 frames. (b) The corresponding SNR values of (a). The red curve is square-root fitting, following the statistical model.

The strategic values of the DPMPC-CRS system are beyond the scope of the above-mentioned technical improvements. First, CRS microscopy is still not at the leading position of biological research due to its poor sensitivity compared with fluorescence microscopy. The EPR effect is the potential solution that helps to boost Raman sensitivity. However, in previous reports, scientists are restricted to choosing the specific fluorescence dyes, whose absorption peak lies in the pre-resonance excitation region, corresponding to the pump wavelength and the desired Raman shift [44, 45]. To conduct the EPR detection, both pump and Stokes frequencies have to be adjusted independently such that they can

doi:10.6342/NTU202300045

meet the requirements of EPR mode ($\Omega = \omega_{\text{pump}} - \omega_{\text{Stokes}}$ and $\omega_0 - \omega_{\text{pump}} = 2-6\Gamma$). In this sense, DPMPC with dual-wavelength tunability is a promising tool for the EPR-SRS function. Second, DPMPC is able to deliver multiple wavelengths, facilitating multiplexed imaging [110, 114] or background subtraction [114]. We envision that CRS spectromicroscopy using DPMPC light source will enhance the sensitivity and specificity via conducting EPR mode and spectral multiplex measurements.

doi:10.6342/NTU202300045

Chapter 6

Conclusion and Future Outlook

6.1 Conclusion

This doctoral thesis is a contribution to the field of pump-probe spectro-microscopy. To be specific, two major aspects of this optical technique are expanded: (1) the demonstration of transient nonlinearity based on nonlinear carrier dynamics characterized by a home-built time-resolved pump-probe spectro-microscopy. This idea adds new degrees of freedom in temporally manipulating nonlinear behaviors; (2) the integration of an advanced supercontinuum light source, a double-pass multiple-plate continuum (DPMPC) with a home-built coherent Raman scattering (CRS) spectro-microscope: design, implementation, and examination of a reliable system for vibrational biomedical imaging as well as electronic pre-resonance detection.

In the first aspect, time-resolved properties in pump-probe spectro-microscopy are utilized to characterize the ultrafast carrier dynamics in silicon nanostructures. The aim

doi:10.6342/NTU202300045

is to expand the dimension of nonlinear behaviors characterization via a combination of intensity-scan methods (x-scan method) in the spatial domain and pump-probe techniques in the temporal domain achieved by our home-built confocal pump-probe spectro-microscope. The concept of transient nonlinearity generation is proposed for the first time, whose underlying mechanism is fluence-dependent recombination lifetime and nonlinear Auger recombination has been adopted as a practical example. Moreover, temporally tunable transient nonlinearity is applied to point-spread-function engineering. The overview of the first part of this dissertation brings a new member, transient nonlinearity into the group of nonlinear photonics as well as ultrafast nonlinear behaviors.

In the second aspect, which focuses on contrast based on the CRS effects in the pump-probe framework is devoted to the development of electronic pre-resonance CRS spectro-microcopy, aiming to provide chemical specificity and high sensitivity. The solutions largely rely on advanced laser systems. The octave-spanning supercontinuum, DPMPC is implemented in CRS spectro-microcopy, enabling spectroscopic interrogation across the entire Raman active region and biomedical imaging. The most important milestone is that benefiting from the dual-wavelength tunability from DPMPC, the EPR effect in CRS spectroscopy with continuous wavelength scanning is demonstrated for the first time, which extends the range of examined molecular species. DPMPC-CRS system opens up a new avenue in the field of coherent Raman spectro-microscopy by adding a new degree of freedom for tuning multiple wavelengths, which is valuable in multiplex imaging and highly sensitive EPR detection.

doi:10.6342/NTU202300045

6.2 Future Outlook

Apart from the current achievements, for the first part, the performance of confocal pump-probe spectro-microscope and the study of transient nonlinearity can be further improved from several perspectives. Temporal resolution is always an important parameter in the time-resolved technique, which could be enhanced via optical pulse compression techniques to compensate for the dispersion, including prism pairs [150], diffraction gratings [151], or commercial-available chirp mirrors. Another important point is the excitation wavelengths, which affect the efficiency of photoexcited carrier generation and lattice heating [29, 152]. Moreover, for the Auger-induced transient nonlinearity, various parameters could take into consideration to manipulate the Auger mechanism, such as excitation rate [153] and sample dimension [89].

For the second part, the performance of the DPMPC-CRS system could be improved in several aspects. First, the enhancement of the spectral resolution: as demonstrated in Sec. 5.7, the adopted etalon has been utilized to narrow down the pass bandwidth. Still, other approaches, such as spectral focusing [138, 147] and pulse shaping [148] could also be applied to enhance the spectral resolution. Moreover, high spectral resolution facilitates the distinction of various biomolecules such as DNA, lipids, and protein in the C-H stretching region based on the multicolor SRS measurement with a linear decomposition algorithm [39, 40]. Second, the further development of the DPMPC light source: kHz repetition rate in the current system limits the imaging speed and sensitivity, where CRS

doi:10.6342/NTU202300045

signals immerse in the laser noise in the low-frequency range. Upgraded refresh rate and detection limit may be solved by adopting the high-power thin-disk lasers at $\sim 10\,\mathrm{MHz}$ repetition rate [149]. High repetition rate ($> 1\,\mathrm{MHz}$) can not only facilitate high-speed imaging but also reduce the $1/f$ laser noise to the shot noise level [9]. Nevertheless, nonlinear background removal methods including stimulated Raman gain and loss detection [110, 112], frequency modulation [113], dual-vibrational excitation [114], and deep learning [115], and noise cancellation methods such as balance detection [133, 154] and boxcar detection [155, 156] can be adopted to further enhance the system sensitivity.

doi:10.6342/NTU202300045

References

[1] Ahmed H Zewail. Laser femtochemistry. *Science*, 242(4886):1645–1653, 1988.

[2] Dongping Zhong, Samir Kumar Pal, Chaozhi Wan, and Ahmed H Zewail. Femtosecond dynamics of a drug-protein complex: Daunomycin with Apo riboflavin-binding protein. *Proceedings of the National Academy of Sciences*, 98(21):11873–11878, 2001.

[3] Samir Kumar Pal, Jorge Peon, Biman Bagchi, and Ahmed H Zewail. Biological water: femtosecond dynamics of macromolecular hydration. *The Journal of Physical Chemistry B*, 106(48):12376–12395, 2002.

[4] Martin C Fischer, Jesse W Wilson, Francisco E Robles, and Warren S Warren. Invited review article: pump-probe microscopy. *Review of Scientific Instruments*, 87(3):031101, 2016.

[5] Pu-Ting Dong and Ji-Xin Cheng. Pump–probe microscopy: theory, instrumentation, and applications. *Spectroscopy*, 32(4):2–11, 2017.

[6] Dar'ya Davydova, Alejandro de la Cadena, Denis Akimov, and Benjamin Dietzek.

doi:10.6342/NTU202300045

Transient absorption microscopy: Advances in chemical imaging of photoinduced dynamics. *Laser & Photonics Reviews*, 10(1):62–81, 2016.

[7] Erik M Grumstrup, Michelle M Gabriel, Emma EM Cating, Erika M Van Goethem, and John M Papanikolas. Pump–probe microscopy: Visualization and spectroscopy of ultrafast dynamics at the nanoscale. *Chemical Physics*, 458:30–40, 2015.

[8] Ji-Xin Cheng and Xiaoliang Sunney Xie. *Coherent Raman scattering microscopy*. CRC press, 2016.

[9] Wei Min, Christian W Freudiger, Sijia Lu, and X Sunney Xie. Coherent nonlinear optical imaging: beyond fluorescence microscopy. *Annual Review of Physical Chemistry*, 62(1):507, 2011.

[10] Chi Zhang and Ji-Xin Cheng. Perspective: Coherent Raman scattering microscopy, the future is bright. *APL Photonics*, 3(9):090901, 2018.

[11] Andreas Othonos. Probing ultrafast carrier and phonon dynamics in semiconductors. *Journal of Applied Physics*, 83(4):1789–1830, 1998.

[12] Tersilla Virgili, Giulia Grancini, Egle Molotokaite, Inma Suarez-Lopez, Sai Kiran Rajendran, Andrea Liscio, Vincenzo Palermo, Guglielmo Lanzani, Dario Polli, and Giulio Cerullo. Confocal ultrafast pump-probe spectroscopy: A new technique to explore nanoscale composites. *Nanoscale*, 4(7):2219–2226, 2012.

[13] Chi Zhang, Delong Zhang, and Ji-Xin Cheng. Coherent Raman scattering mi-

doi:10.6342/NTU202300045

croscopy in biology and medicine. *Annual Review of Biomedical Engineering*, 17:415, 2015.

[14] Warren R Zipfel, Rebecca M Williams, and Watt W Webb. Nonlinear magic: multiphoton microscopy in the biosciences. *Nature Biotechnology*, 21(11):1369–1377, 2003.

[15] Robert W. Boyd. *Nonlinear Optics, Third Edition*. Academic Press, Inc., 2008.

[16] Winifried Denk, James H Strickler, and Watt W Webb. Two-photon laser scanning fluorescence microscopy. *Science*, 248(4951):73–76, 1990.

[17] Barry R Masters. *Confocal microscopy and multiphoton excitation microscopy: the genesis of live cell imaging*, volume 72. SPIE Press, 2006.

[18] Joseph R Lakowicz. *Principles of fluorescence spectroscopy*. Springer, 2006.

[19] Laura Martinez Maestro, Emma Martín Rodríguez, Francisco Sanz Rodríguez, MC Iglesias-de la Cruz, Angeles Juarranz, Rafik Naccache, Fiorenzo Vetrone, Daniel Jaque, John A Capobianco, and José García Solé. CdSe quantum dots for two-photon fluorescence thermal imaging. *Nano letters*, 10(12):5109–5115, 2010.

[20] Till T Meiling, Piotr J Cywiński, and Hans-Gerd Löhmannsröben. Two-photon excitation fluorescence spectroscopy of quantum dots: Photophysical properties and application in bioassays. *The Journal of Physical Chemistry C*, 122(17):9641–9647, 2018.

doi:10.6342/NTU202300045

[21] Jagdeep Shah. *Ultrafast spectroscopy of semiconductors and semiconductor nanostructures*, volume 115. Springer Science & Business Media, 2013.

[22] Rohit P Prasankumar, Prashanth C Upadhya, and Antoinette J Taylor. Ultrafast carrier dynamics in semiconductor nanowires. *Physica Status Solidi (b)*, 246(9):1973–1995, 2009.

[23] Ayan Kar, Prashanth C Upadhya, Shadi A Dayeh, S Tom Picraux, Antoinette J Taylor, and Rohit P Prasankumar. Probing ultrafast carrier dynamics in silicon nanowires. *IEEE Journal of Selected Topics in Quantum Electronics*, 17(4):889–895, 2010.

[24] Sunil Kumar, M Khorasaninejad, MM Adachi, KS Karim, SS Saini, and AK Sood. Probing ultrafast carrier dynamics, nonlinear absorption and refraction in core-shell silicon nanowires. *Pramana*, 79(3):471–481, 2012.

[25] Maxim R Shcherbakov, Polina P Vabishchevich, Alexander S Shorokhov, Katie E Chong, Duk-Yong Choi, Isabelle Staude, Andrey E Miroshnichenko, Dragomir N Neshev, Andrey A Fedyanin, and Yuri S Kivshar. Ultrafast all-optical switching with magnetic resonances in nonlinear dielectric nanostructures. *Nano Letters*, 15(10):6985–6990, 2015.

[26] Maxim R Shcherbakov, Sheng Liu, Varvara V Zubyuk, Aleksandr Vaskin, Polina P Vabishchevich, Gordon Keeler, Thomas Pertsch, Tatyana V Dolgova, Isabelle Staude, Igal Brener, et al. Ultrafast all-optical tuning of direct-gap semiconductor metasurfaces. *Nature Communications*, 8(1):1–6, 2017.

doi:10.6342/NTU202300045

[27] Dario Polli, Daniele Brida, Shaul Mukamel, Guglielmo Lanzani, and Giulio Cerullo. Effective temporal resolution in pump-probe spectroscopy with strongly chirped pulses. *Physical Review A*, 82(5):053809, 2010.

[28] CV Shank, R_ Yen, and Ch Hirlimann. Time-resolved reflectivity measurements of femtosecond-optical-pulse-induced phase transitions in silicon. *Physical Review Letters*, 50(6):454, 1983.

[29] MC Downer and CV Shank. Ultrafast heating of silicon on sapphire by femtosecond optical pulses. *Physical Review Letters*, 56(7):761, 1986.

[30] Takayuki Tanaka, Akira Harata, and Tsuguo Sawada. Subpicosecond surface-restricted carrier and thermal dynamics by transient reflectivity measurements. *Journal of Applied Physics*, 82(8):4033–4038, 1997.

[31] A. J. Sabbah and D. M. Riffe. Femtosecond pump-probe reflectivity study of silicon carrier dynamics. *Physical Review B*, 66(16):165217, 2002.

[32] Juan Cabanillas-Gonzalez, Giulia Grancini, and Guglielmo Lanzani. Pump-probe spectroscopy in organic semiconductors: monitoring fundamental processes of relevance in optoelectronics. *Advanced Materials*, 23(46):5468–5485, 2011.

[33] Yuri Kivshar. All-dielectric meta-optics and non-linear nanophotonics. *National Science Review*, 5(2):144–158, 2018.

[34] Yusuke Nagasaki, Masafumi Suzuki, and Junichi Takahara. All-dielectric dual-color pixel with subwavelength resolution. *Nano Letters*, 17(12):7500–7506, 2017.

doi:10.6342/NTU202300045

[35] Guan-Jie Huang, Hao-Yu Cheng, Yu-Lung Tang, Ikuto Hotta, Junichi Takahara, Kung-Hsuan Lin, and Shi-Wei Chu. Transient super-/sub-linear nonlinearities in silicon nanostructures. *Advanced Optical Materials*, 10(5):2101711, 2022.

[36] Hervé Rigneault and Pascal Berto. Tutorial: coherent Raman light matter interaction processes. *APL Photonics*, 3(9):091101, 2018.

[37] Christian W. Freudiger, Wei Min, Brian G. Saar, Sijia Lu, Gary R. Holtom, Chengwei He, Jason C. Tsai, Jing X. Kang, and X. Sunney Xie. Label-free biomedical imaging with high sensitivity by stimulated Raman scattering microscopy. *Science*, 322(5909):1857, 2008.

[38] Lu Wei, Fanghao Hu, Yihui Shen, Zhixing Chen, Yong Yu, Chih-Chun Lin, Meng C. Wang, and Wei Min. Live-cell imaging of alkyne-tagged small biomolecules by stimulated Raman scattering. *Nature Methods*, 11(4):410–412, 2014.

[39] Fa-Ke Lu, Srinjan Basu, Vivien Igras, Mai P. Hoang, Minbiao Ji, Dan Fu, Gary R. Holtom, Victor A. Neel, Christian W. Freudiger, David E. Fisher, and X. Sunney Xie. Label-free DNA imaging in vivo with stimulated Raman scattering microscopy. *Proceedings of the National Academy of Sciences*, 112(37):11624, 2015.

[40] Luyuan Zhang, Lingyan Shi, Yihui Shen, Yupeng Miao, Mian Wei, Naixin Qian, Yinong Liu, and Wei Min. Spectral tracing of deuterium for imaging glucose metabolism. *Nature Biomedical Engineering*, 3(5):402–413, 2019.

doi:10.6342/NTU202300045

[41] Jessica C Mansfield, George R Littlejohn, Mark P Seymour, Rob J Lind, Sarah Perfect, and Julian Moger. Label-free chemically specific imaging in planta with stimulated Raman scattering microscopy. *Analytical Chemistry*, 85(10):5055–5063, 2013.

[42] Yali Bi, Chi Yang, Yage Chen, Shuai Yan, Guang Yang, Yaozu Wu, Guoping Zhang, and Ping Wang. Near-resonance enhanced label-free stimulated Raman scattering microscopy with spatial resolution near 130 nm. *Light: Science & Applications*, 7(1):1–10, 2018.

[43] Minghua Zhuge, Kai-Chih Huang, Hyeon Jeong Lee, Ying Jiang, Yuying Tan, Haonan Lin, Pu-Ting Dong, Guangyuan Zhao, Daniela Matei, Qing Yang, et al. Ultrasensitive vibrational imaging of retinoids by visible preresonance stimulated Raman scattering microscopy. *Advanced Science*, 8(9):2003136, 2021.

[44] Lu Wei, Zhixing Chen, Lixue Shi, Rong Long, Andrew V Anzalone, Luyuan Zhang, Fanghao Hu, Rafael Yuste, Virginia W Cornish, and Wei Min. Super-multiplex vibrational imaging. *Nature*, 544(7651):465–470, 2017.

[45] Lu Wei and Wei Min. Electronic preresonance stimulated Raman scattering microscopy. *The Journal of Physical Chemistry Letters*, 9(15):4294–4301, 2018.

[46] AC Albrecht and MC Hutley. On the dependence of vibrational Raman intensity on the wavelength of incident light. *The Journal of Chemical Physics*, 55(9):4438–4443, 1971.

doi:10.6342/NTU202300045

[47] John M Dudik, Craig R Johnson, and Sanford A Asher. Wavelength dependence of the preresonance Raman cross sections of CH_3CN, SO_4^{2-}, ClO_4^-, and NO_3^-. *The Journal of Chemical Physics*, 82(4):1732–1740, 1985.

[48] Guan-Jie Huang, Pei-Chen Lai, Ming-Wei Shen, Jia-Xuan Su, Jhan-Yu Guo, Kuo-Chuan Chao, Peng Lin, Ji-Xin Cheng, Li-An Chu, Ann-Shyn Chiang, et al. Towards stimulated Raman scattering spectro-microscopy across the entire Raman active region using a multiple-plate continuum. *Optics Express*, 30(21):38975–38984, 2022.

[49] Jagdeep Shah. *Ultrafast spectroscopy of semiconductors and semiconductor nanostructures*, volume 115. Springer Science & Business Media, 1999.

[50] Ellen J Yoffa. Dynamics of dense laser-induced plasmas. *Physical Review B*, 21(6):2415, 1980.

[51] Henry M van Driel. Kinetics of high-density plasmas generated in Si by 1.06-and 0.53-μm picosecond laser pulses. *Physical Review B*, 35(15):8166, 1987.

[52] D. E. Aspnes and A. A. Studna. Dielectric functions and optical parameters of Si, Ge, GaP, GaAs, GaSb, InP, InAs, and InSb from 1.5 to 6.0 eV. *Physical Review B*, 27(2):985, 1983.

[53] Henry M van Driel. Influence of hot phonons on energy relaxation of high-density carriers in germanium. *Physical Review B*, 19(11):5928, 1979.

[54] D Chekulaev, V Garber, and A Kaplan. Free carrier plasma optical response and

doi:10.6342/NTU202300045

dynamics in strongly pumped silicon nanopillars. *Journal of Applied Physics*, 113(14):143101, 2013.

[55] M Ghanassi, MC Schanne-Klein, F Hache, AI Ekimov, D Ricard, and Chr Flytzanis. Time-resolved measurements of carrier recombination in experimental semiconductor-doped glasses: Confirmation of the role of Auger recombination. *Applied Physics Letters*, 62(1):78–80, 1993.

[56] U Strauss, WW Rühle, and K Köhler. Auger recombination in intrinsic GaAs. *Applied Physics Letters*, 62(1):55–57, 1993.

[57] Ammar Zakar, Rihan Wu, Dimitri Chekulaev, Vera Zerova, Wei He, Leigh Canham, and Andrey Kaplan. Carrier dynamics and surface vibration-assisted Auger recombination in porous silicon. *Physical Review B*, 97(15):155203, 2018.

[58] Sheng S Li. *Semiconductor physical electronics*. Springer Science & Business Media, 2012.

[59] H Htoon, JA Hollingsworth, R Dickerson, and VI Klimov. Effect of zero-to one-dimensional transformation on multiparticle Auger recombination in semiconductor quantum rods. *Physical Review Letters*, 91(22):227401, 2003.

[60] Albert Haug. Carrier density dependence of Auger recombination. *Solid-State Electronics*, 21(11-12):1281–1284, 1978.

[61] Marc Achermann, Andrew P Bartko, Jennifer A Hollingsworth, and Victor I

doi:10.6342/NTU202300045

Klimov. The effect of Auger heating on intraband carrier relaxation in semiconductor quantum rods. *Nature Physics*, 2(8):557–561, 2006.

[62] James R Chelikowsky and Marvin L Cohen. Nonlocal pseudopotential calculations for the electronic structure of eleven diamond and zinc-blende semiconductors. *Physical Review B*, 14(2):556, 1976.

[63] Gustav Mie. Beiträge zur optik trüber medien, speziell kolloidaler metallösungen. *Annalen Der Physik*, 330(3):377–445, 1908.

[64] Sebastian Volz. *Thermal nanosystems and nanomaterials*, volume 118. Springer Science & Business Media, 2009.

[65] Craig F Bohren and Donald R Huffman. *Absorption and scattering of light by small particles*. John Wiley & Sons, 1983.

[66] Shawn Sederberg, Curtis J Firby, Shawn R Greig, and Abdulhakem Y Elezzabi. Integrated nanoplasmonic waveguides for magnetic, nonlinear, and strong-field devices. *Nanophotonics*, 6(1):235–257, 2017.

[67] Arseniy I Kuznetsov, Andrey E Miroshnichenko, Mark L Brongersma, Yuri S Kivshar, and Boris Luk' yanchuk. Optically resonant dielectric nanostructures. *Science*, 354(6314):aag2472, 2016.

[68] Giuseppe Della Valle, Ben Hopkins, Lucia Ganzer, Tatjana Stoll, Mohsen Rahmani, Stefano Longhi, Yuri S Kivshar, Costantino De Angelis, Dragomir N Neshev, and

doi:10.6342/NTU202300045

Giulio Cerullo. Nonlinear anisotropic dielectric metasurfaces for ultrafast nanophotonics. *ACS Photonics*, 4(9):2129–2136, 2017.

[69] Maxim R. Shcherbakov, Dragomir N. Neshev, Ben Hopkins, Alexander S. Shorokhov, Isabelle Staude, Elizaveta V. Melik-Gaykazyan, Manuel Decker, Alexander A. Ezhov, Andrey E. Miroshnichenko, Igal Brener, Andrey A. Fedyanin, and Yuri S. Kivshar. Enhanced third-harmonic generation in silicon nanoparticles driven by magnetic response. *Nano Letters*, 14(11):6488–6492, 2014.

[70] Yi-Shiou Duh, Yusuke Nagasaki, Yu-Lung Tang, Pang-Han Wu, Hao-Yu Cheng, Te-Hsin Yen, Hou-Xian Ding, Kentaro Nishida, Ikuto Hotta, Jhen-Hong Yang, et al. Giant photothermal nonlinearity in a single silicon nanostructure. *Nature Communications*, 11(1):1–9, 2020.

[71] Tianyue Zhang, Ying Che, Kai Chen, Jian Xu, Yi Xu, Te Wen, Guowei Lu, Xiaowei Liu, Bin Wang, Xiaoxuan Xu, et al. Anapole mediated giant photothermal nonlinearity in nanostructured silicon. *Nature Communications*, 11(1):1–9, 2020.

[72] Francesco Priolo, Tom Gregorkiewicz, Matteo Galli, and Thomas F Krauss. Silicon nanostructures for photonics and photovoltaics. *Nature Nanotechnology*, 9(1):19–32, 2014.

[73] Mansoor Sheik-Bahae, Ali A Said, T-H Wei, David J Hagan, and Eric W Van Stryland. Sensitive measurement of optical nonlinearities using a single beam. *IEEE Journal of Quantum Electronics*, 26(4):760–769, 1990.

doi:10.6342/NTU202300045

[74] Jiangwei Wang, Mansour Sheik-Bahae, AA Said, David J Hagan, and Eric W Van Stryland. Time-resolved Z-scan measurements of optical nonlinearities. *Journal of the Optical Society of America B*, 11(6):1009–1017, 1994.

[75] Tushar C Jagadale, Dhanya S Murali, and Shi-Wei Chu. Nonlinear absorption and scattering of a single plasmonic nanostructure characterized by x-scan technique. *Beilstein Journal of Nanotechnology*, 10(1):2182–2191, 2019.

[76] Hsueh-Yu Wu, Yen-Ta Huang, Po-Ting Shen, Hsuan Lee, Ryosuke Oketani, Yasuo Yonemaru, Masahito Yamanaka, Satoru Shoji, Kung-Hsuan Lin, Chih-Wei Chang, et al. Ultrasmall all-optical plasmonic switch and its application to superresolution imaging. *Scientific Reports*, 6(1):1–9, 2016.

[77] Shi-Wei Chu, Hsueh-Yu Wu, Yen-Ta Huang, Tung-Yu Su, Hsuan Lee, Yasuo Yonemaru, Masahito Yamanaka, Ryosuke Oketani, Satoshi Kawata, Satoru Shoji, et al. Saturation and reverse saturation of scattering in a single plasmonic nanoparticle. *ACS Photonics*, 1(1):32–37, 2014.

[78] Sergey Makarov, Sergey Kudryashov, Ivan Mukhin, Alexey Mozharov, Valentin Milichko, Alexander Krasnok, and Pavel Belov. Tuning of magnetic optical response in a dielectric nanoparticle by ultrafast photoexcitation of dense electron-hole plasma. *Nano Letters*, 15(9):6187–6192, 2015.

[79] Wei Min, Sijia Lu, Shasha Chong, Rahul Roy, Gary R Holtom, and X Sunney Xie. Imaging chromophores with undetectable fluorescence by stimulated emission microscopy. *Nature*, 461(7267):1105–1109, 2009.

doi:10.6342/NTU202300045

[80] Dan Fu, Tong Ye, Thomas E Matthews, Gunay Yurtsever, and Warren S Warren Sr. Two-color, two-photon, and excited-state absorption microscopy. *Journal of Biomedical Optics*, 12(5):054004, 2007.

[81] Shasha Chong, Wei Min, and X Sunney Xie. Ground-state depletion microscopy: detection sensitivity of single-molecule optical absorption at room temperature. *The Journal of Physical Chemistry Letters*, 1(23):3316–3322, 2010.

[82] Junjie Li, Weixia Zhang, Ting-Fung Chung, Mikhail N Slipchenko, Yong P Chen, Ji-Xin Cheng, and Chen Yang. Highly sensitive transient absorption imaging of graphene and graphene oxide in living cells and circulating blood. *Scientific Reports*, 5(1):1–9, 2015.

[83] Yong Wang, Chia-Yu Lin, Alexei Nikolaenko, Varun Raghunathan, and Eric O Potma. Four-wave mixing microscopy of nanostructures. *Advances in Optics and Photonics*, 3(1):1–52, 2011.

[84] Qiannan Cui, Yuanyuan Li, Jianhua Chang, Hui Zhao, and Chunxiang Xu. Temporally resolving synchronous degenerate and nondegenerate two-photon absorption in 2D semiconducting monolayers. *Laser & Photonics Reviews*, 13(2):1800225, 2019.

[85] Denis G Baranov, Sergey V Makarov, Valentin A Milichko, Sergey I Kudryashov, Alexander E Krasnok, and Pavel A Belov. Nonlinear transient dynamics of photoexcited resonant silicon nanostructures. *ACS Photonics*, 3(9):1546–1551, 2016.

doi:10.6342/NTU202300045

[86] Kung-Hsuan Lin, Hao-Yu Cheng, Chi-Yuan Yang, Hung-Wei Li, Chih-Wei Chang, and Shi-Wei Chu. Phonon dynamics of single nanoparticles studied using confocal pump-probe backscattering. *Applied Physics Letters*, 113(17):171906, 2018.

[87] Frank Ceballos, Qiannan Cui, Matthew Z Bellus, and Hui Zhao. Exciton formation in monolayer transition metal dichalcogenides. *Nanoscale*, 8(22):11681–11688, 2016.

[88] Min Hu and Gregory V Hartland. Heat dissipation for au particles in aqueous solution: relaxation time versus size. *The Journal of Physical Chemistry B*, 106(28):7029–7033, 2002.

[89] Alicia W Cohn, Alina M Schimpf, Carolyn E Gunthardt, and Daniel R Gamelin. Size-dependent trap-assisted Auger recombination in semiconductor nanocrystals. *Nano Letters*, 13(4):1810–1815, 2013.

[90] George P Zograf, Mihail I Petrov, Dmitry A Zuev, Pavel A Dmitriev, Valentin A Milichko, Sergey V Makarov, and Pavel A Belov. Resonant nonplasmonic nanoparticles for efficient temperature-feedback optical heating. *Nano Letters*, 17(5):2945–2952, 2017.

[91] Denitza Denkova, Martin Ploschner, Minakshi Das, Lindsay M Parker, Xianlin Zheng, Yiqing Lu, Antony Orth, Nicolle H Packer, and James A Piper. 3D sub-diffraction imaging in a conventional confocal configuration by exploiting super-linear emitters. *Nature Communications*, 10(1):1–12, 2019.

doi:10.6342/NTU202300045

[92] Gitanjal Deka, Kentaro Nishida, Kentaro Mochizuki, Hou-Xian Ding, Katsumasa Fujita, and Shi-Wei Chu. Resolution enhancement in deep-tissue nanoparticle imaging based on plasmonic saturated excitation microscopy. *APL Photonics*, 3(3):031301, 2018.

[93] Alex R Guichard, Rohan D Kekatpure, Mark L Brongersma, and Theodore I Kamins. Temperature-dependent Auger recombination dynamics in luminescent silicon nanowires. *Physical Review B*, 78(23):235422, 2008.

[94] Xiaoqi Hou, Jun Kang, Haiyan Qin, Xuewen Chen, Junliang Ma, Jianhai Zhou, Liping Chen, Linjun Wang, Lin-Wang Wang, and Xiaogang Peng. Engineering Auger recombination in colloidal quantum dots via dielectric screening. *Nature Communications*, 10(1):1–11, 2019.

[95] VI Klimov, AA Mikhailovsky, Su Xu, A Malko, JA Hollingsworth, a CA Leatherdale, H-J Eisler, and MG Bawendi. Optical gain and stimulated emission in nanocrystal quantum dots. *Science*, 290(5490):314–317, 2000.

[96] Mark J Kerr, Andres Cuevas, and Patrick Campbell. Limiting efficiency of crystalline silicon solar cells due to coulomb-enhanced Auger recombination. *Progress in Photovoltaics: Research and Applications*, 11(2):97–104, 2003.

[97] Waldemar Kuett, Anton Esser, Klaus Seibert, Uli Lemmer, and Heinrich Kurz. Femtosecond studies of plasma formation in crystalline and amorphous silicon. In *Applications of Ultrashort Laser Pulses in Science and Technology*, volume 1268, pages 154–165. International Society for Optics and Photonics, 1990.

doi:10.6342/NTU202300045

[98] Yu-Lung Tang, Te-Hsin Yen, Kentaro Nishida, Junichi Takahara, Tianyue Zhang, Xiangping Li, Katsumasa Fujita, and Shi-Wei Chu. Mie-enhanced photothermal/thermo-optical nonlinearity and applications on all-optical switch and super-resolution imaging. *Optical Materials Express*, 11(11):3608–3626, 2021.

[99] Omer Tzang, Alexander Pevzner, Robert E Marvel, Richard F Haglund, and Ori Cheshnovsky. Super-resolution in label-free photomodulated reflectivity. *Nano Letters*, 15(2):1362–1367, 2015.

[100] PT Landsberg. Trap-Auger recombination in silicon of low carrier densities. *Applied Physics Letters*, 50(12):745–747, 1987.

[101] C. V. Raman and K. S. Krishnan. A new type of secondary radiation. *Nature*, 121(3048):501–502, 1928.

[102] Ricardo Aroca. *Surface-enhanced vibrational spectroscopy*. John Wiley & Sons, 2006.

[103] David W. McCamant, Philipp Kukura, and Richard A. Mathies. Femtosecond broadband stimulated Raman: a new approach for high-performance vibrational spectroscopy. *Applied Spectroscopy*, 57(11):1317–1323, 2003.

[104] Derek A. Long. *The Raman effect: a unified treatment of the theory of Raman scattering by molecules*, volume 8. Wiley Chichester, 2002.

[105] Ji-Xin Cheng and X Sunney Xie. Coherent anti-Stokes Raman scattering mi-

doi:10.6342/NTU202300045

croscopy: instrumentation, theory, and applications. *The Journal of Physical Chemistry B*, 108(3):827–840, 2004.

[106] Ji-Xin Cheng, Lewis D Book, and X Sunney Xie. Polarization coherent anti-Stokes Raman scattering microscopy. *Optics Letters*, 26(17):1341–1343, 2001.

[107] Andreas Volkmer, Lewis D Book, and X Sunney Xie. Time-resolved coherent anti-Stokes Raman scattering microscopy: imaging based on Raman free induction decay. *Applied Physics Letters*, 80(9):1505–1507, 2002.

[108] Conor L Evans, Eric O Potma, Mehron Puoris' haag, Daniel Côté, Charles P Lin, and X Sunney Xie. Chemical imaging of tissue in vivo with video-rate coherent anti-Stokes Raman scattering microscopy. *Proceedings of the National Academy of Sciences of the United States of America*, 102(46):16807–16812, 2005.

[109] Alejandro De la Cadena, Federico Vernuccio, Andrea Ragni, Giuseppe Sciortino, Renzo Vanna, Carino Ferrante, Natalia Pediconi, Carlo Valensise, Luca Genchi, Sergey P Laptenok, et al. Broadband stimulated Raman imaging based on multi-channel lock-in detection for spectral histopathology. *APL Photonics*, 7(7):076104, 2022.

[110] Pascal Berto, Esben Ravn Andresen, and Hervé Rigneault. Background-free stimulated Raman spectroscopy and microscopy. *Physical Review Letters*, 112(5):053905, 2014.

[111] Delong Zhang, Mikhail N Slipchenko, Daniel E Leaird, Andrew M Weiner, and

doi:10.6342/NTU202300045

Ji-Xin Cheng. Spectrally modulated stimulated Raman scattering imaging with an angle-to-wavelength pulse shaper. *Optics Express*, 21(11):13864–13874, 2013.

[112] Sandro Heuke, Alberto Lombardini, Edlef Büttner, and Hervé Rigneault. Simultaneous stimulated Raman gain and loss detection (SRGAL). *Optics Express*, 28(20):29619–29630, 2020.

[113] Hanqing Xiong, Naixin Qian, Zhilun Zhao, Lingyan Shi, Yupeng Miao, and Wei Min. Background-free imaging of chemical bonds by a simple and robust frequency-modulated stimulated Raman scattering microscopy. *Optics Express*, 28(10):15663–15677, 2020.

[114] Sandro Heuke, Ingo Rimke, Barbara Sarri, Paulina Gasecka, Romain Appay, Loic Legoff, Peter Volz, Edlef Büttner, and Hervé Rigneault. Shot-noise limited tunable dual-vibrational frequency stimulated Raman scattering microscopy. *Biomedical Optics Express*, 12(12):7780–7789, 2021.

[115] Bryce Manifold, Elena Thomas, Andrew T Francis, Andrew H Hill, and Dan Fu. Denoising of stimulated Raman scattering microscopy images via deep learning. *Biomedical Optics Express*, 10(8):3860–3874, 2019.

[116] Andreas C Albrecht. On the theory of Raman intensities. *The Journal of Chemical Physics*, 34(5):1476–1484, 1961.

[117] Sanford A Asher. UV resonance Raman studies of molecular structure and dynam-

doi:10.6342/NTU202300045

ics: applications in physical and biophysical chemistry. *Annual Review of Physical Chemistry*, 39:537–588, 1988.

[118] Shibin Deng, Weigao Xu, Jinying Wang, Xi Ling, Juanxia Wu, Liming Xie, Jing Kong, Mildred S Dresselhaus, and Jin Zhang. Direct measurement of the Raman enhancement factor of Rhodamine 6G on graphene under resonant excitation. *Nano Research*, 7(9):1271–1279, 2014.

[119] Bruce Hudson, W_ Hetherington III, Stephen Cramer, Ilan Chabay, and Gary K Klauminzer. Resonance enhanced coherent anti-Stokes Raman scattering. *Proceedings of the National Academy of Sciences*, 73(11):3798–3802, 1976.

[120] Lixue Shi, Hanqing Xiong, Yihui Shen, Rong Long, Lu Wei, and Wei Min. Electronic resonant stimulated Raman scattering micro-spectroscopy. *The Journal of Physical Chemistry B*, 122(39):9218–9224, 2018.

[121] Bo-Han Chen, Jia-Xuan Su, Jhan-Yu Guo, Kai Chen, Shi-Wei Chu, Hsuan-Hao Lu, Chih-Hsuan Lu, and Shang-Da Yang. Double-pass multiple-plate continuum for high temporal contrast nonlinear pulse compression. *Frontiers in Photonics*, 3:937622, 2022.

[122] Christian W Freudiger, Wei Min, Brian G Saar, Sijia Lu, Gary R Holtom, Chengwei He, Jason C Tsai, Jing X Kang, and X Sunney Xie. Label-free biomedical imaging with high sensitivity by stimulated Raman scattering microscopy. *Science*, 322(5909):1857–1861, 2008.

doi:10.6342/NTU202300045

[123] Brian G Saar, Christian W Freudiger, Jay Reichman, C Michael Stanley, Gary R Holtom, and X Sunney Xie. Video-rate molecular imaging in vivo with stimulated Raman scattering. *Science*, 330(6009):1368–1370, 2010.

[124] Andreas Zumbusch, Gary R Holtom, and X Sunney Xie. Three-dimensional vibrational imaging by coherent anti-Stokes Raman scattering. *Physical Review Letters*, 82(20):4142, 1999.

[125] Fa-Ke Lu, Srinjan Basu, Vivien Igras, Mai P Hoang, Minbiao Ji, Dan Fu, Gary R Holtom, Victor A Neel, Christian W Freudiger, David E Fisher, et al. Label-free DNA imaging in vivo with stimulated Raman scattering microscopy. *Proceedings of the National Academy of Sciences*, 112(37):11624–11629, 2015.

[126] Fanghao Hu, Zhixing Chen, Luyuan Zhang, Yihui Shen, Lu Wei, and Wei Min. Vibrational imaging of glucose uptake activity in live cells and tissues by stimulated Raman scattering. *Angewandte Chemie International Edition*, 54(34):9821–9825, 2015.

[127] Christian W Freudiger, Wei Min, Gary R Holtom, Bingwei Xu, Marcos Dantus, and X Sunney Xie. Highly specific label-free molecular imaging with spectrally tailored excitation-stimulated Raman scattering (STE-SRS) microscopy. *Nature Photonics*, 5(2):103–109, 2011.

[128] Lu Wei, Fanghao Hu, Yihui Shen, Zhixing Chen, Yong Yu, Chih-Chun Lin, Meng C Wang, and Wei Min. Live-cell imaging of alkyne-tagged small biomolecules by stimulated Raman scattering. *Nature Methods*, 11(4):410–412, 2014.

doi:10.6342/NTU202300045

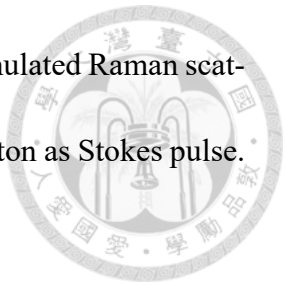

[129] Esben Ravn Andresen, Pascal Berto, and Hervé Rigneault. Stimulated Raman scattering microscopy by spectral focusing and fiber-generated soliton as Stokes pulse. *Optics Letters*, 36(13):2387–2389, 2011.

[130] Nicola Coluccelli, Vikas Kumar, Marco Cassinerio, Gianluca Galzerano, Marco Marangoni, and Giulio Cerullo. Er/Tm: fiber laser system for coherent Raman microscopy. *Optics Letters*, 39(11):3090–3093, 2014.

[131] Thomas Würthwein, Kristin Wallmeier, Maximilian Brinkmann, Tim Hellwig, Niklas M Lüpken, Nick S Lemberger, and Carsten Fallnich. Multi-color stimulated Raman scattering with a frame-to-frame wavelength-tunable fiber-based light source. *Biomedical Optics Express*, 12(10):6228–6236, 2021.

[132] Maximilian Brinkmann, Sven Dobner, and Carsten Fallnich. Light source for narrow and broadband coherent Raman scattering microspectroscopy. *Optics Letters*, 40(23):5447–5450, 2015.

[133] Christian W Freudiger, Wenlong Yang, Gary R Holtom, Nasser Peyghambarian, X Sunney Xie, and Khanh Q Kieu. Stimulated Raman scattering microscopy with a robust fibre laser source. *Nature Photonics*, 8(2):153–159, 2014.

[134] Hope T Beier, Gary D Noojin, and Benjamin A Rockwell. Stimulated Raman scattering using a single femtosecond oscillator with flexibility for imaging and spectral applications. *Optics Express*, 19(20):18885–18892, 2011.

[135] Hsiang-Yu Chung, Wei Liu, Qian Cao, Franz X Kärtner, and Guoqing Chang. Er-

doi:10.6342/NTU202300045

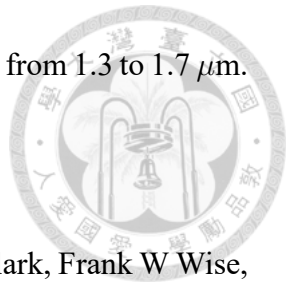

fiber laser enabled, energy scalable femtosecond source tunable from 1.3 to 1.7 μm. *Optics Express*, 25(14):15760–15771, 2017.

[136] Nicholas G Horton, Ke Wang, Demirhan Kobat, Catharine G Clark, Frank W Wise, Chris B Schaffer, and Chris Xu. In vivo three-photon microscopy of subcortical structures within an intact mouse brain. *Nature Photonics*, 7(3):205–209, 2013.

[137] Delong Zhang, Mikhail N Slipchenko, and Ji-Xin Cheng. Highly sensitive vibrational imaging by femtosecond pulse stimulated Raman loss. *The Journal of Physical Chemistry Letters*, 2(11):1248–1253, 2011.

[138] Kota Koike, Nicholas I Smith, and Katsumasa Fujita. Spectral focusing in picosecond pulsed stimulated Raman scattering microscopy. *Biomedical Optics Express*, 13(2):995–1004, 2022.

[139] Chih-Hsuan Lu, Yu-Jung Tsou, Hong-Yu Chen, Bo-Han Chen, Yu-Chen Cheng, Shang-Da Yang, Ming-Chang Chen, Chia-Chen Hsu, and Andrew H Kung. Generation of intense supercontinuum in condensed media. *Optica*, 1(6):400–406, 2014.

[140] Chih-Hsuan Lu, Wei-Hsin Wu, Shiang-He Kuo, Jhan-Yu Guo, Ming-Chang Chen, Shang-Da Yang, and AH Kung. Greater than 50 times compression of 1030 nm Yb: KGW laser pulses to single-cycle duration. *Optics Express*, 27(11):15638–15648, 2019.

[141] Murat Yildirim, Hiroki Sugihara, Peter TC So, and Mriganka Sur. Functional imag-

doi:10.6342/NTU202300045

ing of visual cortical layers and subplate in awake mice with optimized three-photon microscopy. *Nature Communications*, 10(1):1–12, 2019.

[142] Henrik Fabricius and Oliver Pust. Linear variable filters for biomedical and hyperspectral imaging applications. *Biomedical Optics*, page BS3A.42, 2014.

[143] P Neelakantan. Raman spectrum of acetonitrile. *Proceedings of the Indian Academy of Sciences-Section A*, 60(6):422–424, 1964.

[144] Tobias Steinle, Vikas Kumar, Moritz Floess, Andy Steinmann, Marco Marangoni, Claudia Koch, Christina Wege, Giulio Cerullo, and Harald Giessen. Synchronization-free all-solid-state laser system for stimulated Raman scattering microscopy. *Light: Science & Applications*, 5(10):e16149–e16149, 2016.

[145] Mojtaba Mohseni, Christoph Polzer, and Thomas Hellerer. Resolution of spectral focusing in coherent Raman imaging. *Optics Express*, 26(8):10230–10241, 2018.

[146] Tianyu Wang, Chunyan Wu, Dimitre G Ouzounov, Wenchao Gu, Fei Xia, Minsu Kim, Xusan Yang, Melissa R Warden, and Chris Xu. Quantitative analysis of 1300-nm three-photon calcium imaging in the mouse brain. *Elife*, 9:e53205, 2020.

[147] KE Thorn, NR Monahan, SKK Prasad, K Chen, and JM Hodgkiss. Efficient and tunable spectral compression using frequency-domain nonlinear optics. *Optics Express*, 26(21):28140–28149, 2018.

[148] Andrew M Weiner. Ultrafast optical pulse shaping: A tutorial review. *Optics Communications*, 284(15):3669–3692, 2011.

doi:10.6342/NTU202300045

[149] Chia-Lun Tsai, Frank Meyer, Alan Omar, Yicheng Wang, An-Yuan Liang, Chih-Hsuan Lu, Martin Hoffmann, Shang-Da Yang, and Clara J Saraceno. Efficient nonlinear compression of a mode-locked thin-disk oscillator to 27 fs at 98 W average power. *Optics Letters*, 44(17):4115–4118, 2019.

[150] JD Kafka and T Baer. Prism-pair dispersive delay lines in optical pulse compression. *Optics Letters*, 12(6):401–403, 1987.

[151] Edmond Treacy. Optical pulse compression with diffraction gratings. *IEEE Journal of Quantum Electronics*, 5(9):454–458, 1969.

[152] GE Jellison Jr and FA Modine. Optical functions of silicon at elevated temperatures. *Journal of Applied Physics*, 76(6):3758–3761, 1994.

[153] Patrick E Hopkins, Edward V Barnat, Jose L Cruz-Campa, Robert K Grubbs, Murat Okandan, and Gregory N Nielson. Excitation rate dependence of Auger recombination in silicon. *Journal of Applied Physics*, 107(5):053713, 2010.

[154] Francesco Crisafi, Vikas Kumar, Tullio Scopigno, Marco Marangoni, Giulio Cerullo, and Dario Polli. In-line balanced detection stimulated Raman scattering microscopy. *Scientific Reports*, 7(1):1–8, 2017.

[155] Durga Prasad Khatua, Sabina Gurung, Asha Singh, Salahuddin Khan, Tarun Kumar Sharma, and J Jayabalan. Filtering noise in time and frequency domain for ultrafast pump–probe performed using low repetition rate lasers. *Review of Scientific Instruments*, 91(10):103901, 2020.

doi:10.6342/NTU202300045

[156] Peter Fimpel, Claudius Riek, Lukas Ebner, Alfred Leitenstorfer, Daniele Brida, and Andreas Zumbusch. Boxcar detection for high-frequency modulation in stimulated Raman scattering microscopy. *Applied Physics Letters*, 112(16):161101, 2018.

doi:10.6342/NTU202300045

Appendix A — *PyMieScatt* Code

In this appendix, we write down the *PyMieScatt* python code for Mie theory calculation. We thank Mr. Pang-Han Wu for his helpful assistance with this code.

- Mie spectrum

```
pip install PyMieScatt

import numpy as np
import matplotlib.pyplot as plt
import PyMieScatt as ms
"""
Mie Scattering
Reference
https://pymiescatt.readthedocs.io/en/latest/forward.html
"""
# parameters
l = 785.0   # wavelength (nm)
d = 150.0   # diameter of the particle (nm)
n = np.array([3.9,4,4.1])    # n1 n2 n3
# derived parameters
x = np.pi * d / l
# spectral range
spec   = np.linspace( 400.0, 800.0, 1001)
```


doi:10.6342/NTU202300045

```
spec_x = np.pi * d / spec
# red shift
# scattering
sn1  = np.empty(len(spec))
sn2  = np.empty(len(spec))
sn3  = np.empty(len(spec))
# absorption
an1  = np.empty(len(spec))
an2  = np.empty(len(spec))
an3  = np.empty(len(spec))
cross_section = np.empty(( 7, len(spec) ))
for i in range(len(spec)):
    sn1[i]  = ms.MieQ( n[0], spec[i], d, asCrossSection=True )[1]
    sn2[i]  = ms.MieQ( n[1], spec[i], d, asCrossSection=True )[1]
    sn3[i]  = ms.MieQ( n[2], spec[i], d, asCrossSection=True )[1]
    an1[i]  = ms.MieQ( n[0], spec[i], d, asCrossSection=True )[2]
    an2[i]  = ms.MieQ( n[1], spec[i], d, asCrossSection=True )[2]
    an3[i]  = ms.MieQ( n[2], spec[i], d, asCrossSection=True )[2]

for i in range(len(spec)):
    cross_section[0][i] = spec[i]
    cross_section[1][i] = sn1[i]
    cross_section[2][i] = sn2[i]
    cross_section[3][i] = sn3[i]
    cross_section[4][i] = an1[i]
    cross_section[5][i] = an2[i]
    cross_section[6][i] = an3[i]
# plot
plt.figure(figsize=(12, 6))
plt.subplot( 1, 2, 1 )
plt.plot(spec,sn1, label='sca_n1')
plt.plot(spec,sn2, label='sca_n2')
```


doi:10.6342/NTU202300045

```
plt.plot(spec,sn3, label='sca_n3')
plt.legend(loc='upper right')
plt.subplot( 1, 2, 2 )
plt.plot(spec,an1, label='abs_n1')
plt.plot(spec,an2, label='abs_n2')
plt.plot(spec,an3, label='abs_n3')
plt.legend(loc='upper right')
# data
np.savetxt('output.txt', np.transpose(cross_section))
```

- Multipole decomposition

```
pip install PyMieScatt

import numpy as np
import pandas as pd
import matplotlib.pyplot as plt
import PyMieScatt as ms

# Paramenters
DP  = 150.            # diameter of the particle (nm)
N   = 4.              # reflective index, List
WL  = [400., 800.]    # range of light wavelength (nm)
RES = 1600            # resolution of the wavelength in the range

# Calculation
items = ['ED', 'MD', 'EQ', 'MQ']
decompose = {k: [] for k in items}
wavelength = np.linspace(*WL, RES)

for wl in wavelength:
    s = np.pi*DP/wl
    coefficients = ms.Mie_ab(m=N, x=s)
```


doi:10.6342/NTU202300045

```
    decompose['ED'].append(np.abs(coefficients[0][0]))
    decompose['MD'].append(np.abs(coefficients[1][0]))
    decompose['EQ'].append(np.abs(coefficients[0][1]))
    decompose['MQ'].append(np.abs(coefficients[1][1]))

# Plot
plt.figure(dpi=100)
for it in items:
    plt.plot(
        wavelength, decompose[it],
        label=it
    )

plt.xlabel('Wavelength $(nm)$')
plt.legend()
plt.show()
```

- Mie scattering in different refractive index conditions

```
pip install PyMieScatt

import numpy as np
import pandas as pd
import matplotlib.pyplot as plt
import PyMieScatt as ms

# Paramenters
DP  = 150.            # diameter of the particle (nm)
N   = [3.9, 4., 4.1]  # List of reflective indice
WL  = [400., 800.]    # range of light wavelength (nm)
RES = 1600            # resolution of the wavelength in the range

# Calculation
```


doi:10.6342/NTU202300045

```
wavelength = np.linspace(*WL, RES)
scattering_cross_section = {k: [] for k in N}

for n in N:
    for wl in wavelength:
        cs = ms.MieQ(m=n, wavelength=wl, diameter=DP,
    asCrossSection=True)[1]
        scattering_cross_section[n].append(cs)

# Plot
plt.figure(dpi=100)
for n in N:
    plt.plot(wavelength, scattering_cross_section[n], label=f'n={n
    }')

plt.xlabel('Wevelength $(nm)$')
plt.ylabel('C_scattering $(nm^{2})$')
plt.legend()
plt.show()

# Output
pd.DataFrame(scattering_cross_section, index=wavelength).to_csv('
    refractive.csv')
```


doi:10.6342/NTU202300045